



12-2022

Development of a New High-Resolution Neutron Detector and Beta-delayed Neutron Spectroscopy of 240.

Shree K. Neupane

University of Tennessee, Knoxville, sneupan4@vols.utk.edu

Follow this and additional works at: https://trace.tennessee.edu/utk_graddiss

 Part of the [Nuclear Commons](#)

Recommended Citation

Neupane, Shree K., "Development of a New High-Resolution Neutron Detector and Beta-delayed Neutron Spectroscopy of 240.. " PhD diss., University of Tennessee, 2022.
https://trace.tennessee.edu/utk_graddiss/7585

This Dissertation is brought to you for free and open access by the Graduate School at TRACE: Tennessee Research and Creative Exchange. It has been accepted for inclusion in Doctoral Dissertations by an authorized administrator of TRACE: Tennessee Research and Creative Exchange. For more information, please contact trace@utk.edu.

To the Graduate Council:

I am submitting herewith a dissertation written by Shree K. Neupane entitled "Development of a New High-Resolution Neutron Detector and Beta-delayed Neutron Spectroscopy of ^{240}Pu ." I have examined the final electronic copy of this dissertation for form and content and recommend that it be accepted in partial fulfillment of the requirements for the degree of Doctor of Philosophy, with a major in Physics.

Robert K Grzywacz, Major Professor

We have read this dissertation and recommend its acceptance:

Thomas Papenbrock, Miguel Madurga, Lawrence H Heilbronn

Accepted for the Council:

Dixie L. Thompson

Vice Provost and Dean of the Graduate School

(Original signatures are on file with official student records.)

**Development of a New
High-Resolution Neutron Detector
and Beta-delayed Neutron
Spectroscopy of ^{24}O**

A Dissertation Presented for the

Doctor of Philosophy

Degree

The University of Tennessee, Knoxville

Shree Neupane

December 2022

© by Shree Neupane, 2022
All Rights Reserved.

For my family and friends

Acknowledgments

I'm incredibly grateful to my adviser, Dr. Robert Grzywacz, for his mentorship, guidance, and support throughout the working period. He provided me with opportunities to explore exciting things and always encouraged me to participate in various research activities. I want to extend my sincere thanks to my thesis committee members, Dr. Thomas Papenbrock, Dr. Miguel Madurga, and Dr. Lawrence Heilbronn, for serving on my committee and providing valuable comments and suggestions.

Many thanks to my colleagues and research group, Joseph Heideman, Thomas King, Noritaka Kitamura, Maninder Singh, Zhengyu Xu, and Rin Yokoyama, for their support in the research projects and great discussions. I also want to thank all the participants for their help during the experiments and the co-authors for their input in making the manuscripts publishable.

Lastly, I owe the greatest thanks to my family and friends for providing unlimited support and continuous encouragement throughout my studies.

Abstract

An efficient neutron detection system with good energy resolution is needed to correctly characterize the decays of neutron-rich nuclei where beta-delayed neutron emission is a dominant decay mode. Precision neutron spectroscopy probes nuclear structure effects in neutron-rich nuclei and is essential to exploit the opportunities in new-generation radioactive beam facilities. A new high-resolution neutron detector, Neutron dEtector with Xn Tracking (NEXT), has been constructed, characterized, and tested in decay and reaction experiments. Its essential capability is the neutron interaction position localization, which enables improvement in energy resolution without compromising detection efficiency in the time-of-flight measurements. Neutron-gamma discrimination capability of NEXT allows for performing experiments even in high background conditions. First measurements were performed with beta-delayed neutron emitters using NEXT at Argonne National Laboratory (ANL), focussing on fission fragments. At National Superconducting Cyclotron Laboratory (NSCL), NEXT was used alongside the Versatile Array of Neutron Detectors at Low Energy (VANDLE) to study light drip-line nuclei at and below the island of inversion with first-ever neutron spectroscopy performed for several isotopes.

The neutron energy spectrum measurement of the beta-delayed neutron precursor ^{24}O was performed for the first time at NSCL using two different neutron detector arrays: VANDLE and NEXT, accompanied by gamma spectroscopy. The beta-gamma and beta-delayed neutron measurements following the decay of ^{24}O provided the beta decay strength distribution extending to neutron unbound states in ^{24}F , serving as an excellent case to test the nuclear model calculations near the neutron drip line. The experimental results are compared with the shell model calculations using the standard USDA and USDB interactions and IMSRG.

Table of Contents

1	Introduction	1
1.1	β decay	2
1.1.1	Allowed and Forbidden Decays	3
1.2	β -delayed neutron emission	4
1.2.1	Models of β decay and β -delayed neutron emission	8
1.2.2	Astrophysical Application: The r-process	12
1.2.3	Applied Research	13
2	Neutron Detectors	15
2.1	Neutron Detection Mechanism	15
2.2	Neutron Detectors in Decay Studies	16
2.3	Time-of-Flight Technique	17
2.4	Neutron-Gamma Discrimination	18
3	Development of New High-Resolution Neutron Detector	21
3.1	NEXT Concept	21
3.2	NEXT Modules	23
3.3	Readout scheme of NEXT	24
3.4	High-Resolution Timing Analysis	24
3.5	High-Resolution Position Analysis	25
3.6	Trigger configurations	25
3.7	Signal Readout Assembly	27
3.8	New Digitizers	27

3.9	NEXT array	28
3.9.1	Prototyping Stage (Phase-I)	28
3.9.2	Phase-II	28
4	Efficiency Measurement	45
4.1	$^{27}\text{Al}(\text{d},\text{n})$ Measurement	45
4.2	Simulations: NEXT $_{sim}$	47
4.3	^{252}Cf measurement with new trigger scheme	48
5	Position-Timing Correlation and Correction	56
5.1	TOF Corrections	56
5.2	^{17}N β -delayed neutron emission	60
5.3	$^{27}\text{Al}(\text{d},\text{n})$ Thin Target Measurement	64
5.4	^{106}Nb β -delayed neutron emission	65
6	Beta-delayed Neutron Spectroscopy of ^{24}O Using VANDLE and NEXT	76
6.1	Motivation	76
6.1.1	Nuclear Shell Model	77
6.1.2	Previous measurements and knowledge on structure of ^{24}O	77
6.2	Isotope Production and Particle Identification	79
6.3	Experimental Setup	83
6.4	Ion-Beta Correlations	85
6.5	Analysis of the ^{24}O Decay	85
6.5.1	Half-life Determination	85
6.5.2	Background Estimation for Neutron and Analysis	88
6.5.3	Gamma Ray Analysis	88
6.5.4	Analysis of Neutron Time-of-Flight Spectrum	93
6.5.5	Comparison with Shell Model Calculations	99
6.5.6	Discussion	103
7	Summary	106

List of Tables

1.1	Allowed and forbidden decays selection rules.	5
6.1	The half-lives for various isotopes obtained in this work compared with literature values.	89
6.2	Branching ratios and logft values for the neutron emitting states in ^{24}F . . .	100
6.3	The possible spin-orbit configurations for neutron and proton for Gamow-Teller transition in the decay of ^{24}O in sd-shell model space.	105

List of Figures

1.1	A chart of nuclei showing $Q_\beta - S_n$ values.	5
1.2	Schematic of a β -delayed neutron emission process.	6
1.3	A chart of nuclei with the prediction of multineutron emission towards the drip line.	7
1.4	Schematic of the cut-off model to determine the neutron emission probabilities. The sum of the strengths to the emitter states above various separation energies gives the maximum probabilities of neutron emission.	10
1.5	Schematic of the QRPA and Hauser-Feshbach approach to study β decay and delayed neutron emission. The β decay of the precursor is calculated by QRPA and the subsequent delayed neutron and gamma emission treated in Hauser-Feshbach statistical approach.	11
1.6	An example showing the effect of β -delayed neutrons in the decay path towards stability.	14
2.1	Schematic of the neutron time-of-flight technique with “straight” shape scintillators. The time-of-flight of the neutron is measured between the start detector and the neutron detector (stop) over a specific flight path length L.	19
2.2	Scintillation response of the organic scintillator for different exciting particles. The figure is adapted from J.F. Knoll.	20
3.1	Energy resolution as a function of neutron energy for different segment thicknesses.	30

3.2	Schematic drawing of NEXT in the TOF setup. A single detector unit with the photosensors coupled on either side (top). The detector is facing the neutron’s flight path direction. Side view of the detector showing the possible segmentation, higher segmentation along the neutron flight path direction (bottom).	31
3.3	Multianode PMT (MAPMT) model H12700B.	32
3.4	(a) A typical NEXT Module. The segmented plastic scintillator is coupled to the Hamamatsu H12700 position-sensitive PMTs on either side for the light readout. (b) Cross-section view of the detector. Higher segmentation is along the direction of the neutron flight path (along the x-axis). The segments along the x-axis are referred to as the detector layers/columns, and segments along the y-axis are referred to as rows. There are eight detector layers/columns and four rows in a fully assembled detector module.	33
3.5	Pixie-16 16 channel digitizer from XIA LLC.	34
3.6	A schematic representation of the NEXT readout in TOF setup with start detector. The five signals from each side of the NEXT (dynode: red, anodes: blue) and a signal from the TOF start detectors are digitized using Pixie-16 digitizers. The TOF start detector provides a reference signal for the time-of-flight measurement. These signals communicate using backplane trigger lines to generate the coincident trigger configurations.	35
3.7	Anger logic resistive circuit.	36
3.8	A typical digitized trace with the polyCFD algorithm for the CFD threshold of 45%. The third-order polynomial fit to find the peak maximum is shown in green, while the linear interpolation between the points around the CFD threshold is shown in magenta. The crossing point between the magenta and green line (CFD threshold), represented by the dashed red line, determines the high-resolution timing.	37
3.9	The neutron interaction position in the detector extracted using Equations 3.3a and 3.3b.	38

3.10	The schematic representation of the coincidence trigger schemes. (a) Generating the global validation trigger using start detectors (beta singles) and NEXT dynodes. (b) A triple coincidence trigger scheme, where anodes are always required to be in coincidence with dynodes from the same detector. (c) A new trigger configuration based on unconditional readout of the anode signals. This trigger scheme allows the forced recording of a signal if a global trigger is generated.	39
3.11	Schematic view of new signal readout assembly developed by Vertilon Corporation top). Actual boards coupled to a 10 inches long module (bottom).	40
3.12	New Pixie digitizer (Pixie-16x2).	41
3.13	An array of 10 NEXT modules assembled for the experiment at Argonne National Laboratory.	42
3.14	The scintillation position inside the different NEXT modules reconstructed using the Anger logic algorithm. (a) EJ276, single layer ESR, polished sides, and adhesive material between the segments. (b) EJ200, single layer ESR, polished sides, and adhesive material between the segments. (c) EJ276, double layer ESR, polished sides, and adhesive material between the segments. (d) EJ276, double layer ESR, unpolished sides, and adhesive material between the segments. (e) EJ276, 5X10 segmentation, double layer ESR, polished sides, and air gap between the segments. (f) EJ276, double layer ESR, polished sides, and air gap between the segments.	43
3.15	NEXT modules stored in a chamber filled with Nitrogen gas to avoid the scintillator degradation.	44
4.1	A reference neutron spectrum with known neutron flux for $^{27}\text{Al}(d,n)$ at 120° measured at the Edwards Accelerator Laboratory (EAL) at Ohio University.	46
4.2	The experimental setup at EAL. The NEXT modules were placed at a distance of 5 m from the target assembly inside the 30 m long neutron time-of-flight tunnel. The neutron beam was collimated using concentric polyethylene collimators.	50

4.3	The time-of-flight spectra measured by EJ276-10 module with $^{27}\text{Al}(\text{d},\text{n})$ at 120° with a module in beam (black), the module moved out of the beam (red).	51
4.4	The efficiency for EJ276-10 (black), EJ276-05 (blue) and EJ200-10 (red) modules obtained from $^{27}\text{Al}(\text{d},\text{n})$ reactions at 120° with a 20 keVee threshold.	52
4.5	The measured intrinsic efficiency using $^{27}\text{Al}(\text{d},\text{n})$ reactions at 120° at EAL with 20 keVee threshold (black) compared to the NEXTSim calculation (red) for EJ200-10 (a) EJ276-05 (b) and EJ276-10 (c) modules.	53
4.6	Two-dimensional histograms showing the sum of the left anode QDCs (integral of the pulse within a given time interval) plotted against the corresponding detector layer for events taken with the triple coincidence trigger (a) and the new external trigger configuration (b). The zeroth layer indicates the layer closest to the source. The higher QDC threshold in the front (towards the source) and back (away from the source) layers seen in the top plot does not exist in data taken with the new trigger mode. The detection threshold is consistent between the layers, as shown in the bottom plot.	54
4.7	(a) Ratio of number of neutrons measured per energy bin in new and old trigger schemes with the EJ276-10 module using ^{252}Cf source. (b) The efficiency of the EJ276-10 module measured at EAL was corrected using the ratio of neutrons detected in the new and old trigger schemes shown in Figure 4.7a.	55
5.1	The schematic demonstration of TOF correction procedure using the neutron interaction position inside the detector. Based on interaction position, the original flight path length (L) can be resolved into x, y, and z components with respect to a fixed flight path length (L_0). The TOF is corrected for the flight path by scaling the actual TOF measurement by the ratio of L_0 and L .	58

5.2	The reconstructed neutron interaction position in a NEXT module. The X and Y positions are the same as shown in Figure 5.1. The pixels represent the module segmentation. The original TOF is obtained exclusively for each pixel and scaled to the middle of the first layer using Equation 5.1 as indicated by the red lines. See the text for the detail.	59
5.3	The decay scheme of ^{17}N . The β decay of ^{17}N populates the states above neutron separation energy in ^{17}O , which de-excite to the ground state of ^{16}O via neutron emission. All the energies are in keV.	61
5.4	The experimental setup at NSCL. Ten NEXT modules were arranged around the ion implant position at a distance of ~ 50 cm.	62
5.5	The neutron TOF measured at the individual layers before the TOF correction (a) and after the TOF correction (b). The spectra are zoomed around two high-intensity peaks for clarity.	63
5.6	The summed neutron TOF spectrum for ^{17}N β -delayed neutron emission before the TOF correction (black) and after TOF correction (red).	67
5.7	The neutron TOF plotted against the interaction position along the flight path direction (X-position) for one of the NEXT modules before the TOF correction (a) and after the TOF correction (b).	68
5.8	The simulation of the ^{17}N neutron emission without widths (green) and with widths (blue) added to the neutron emitting states in ^{17}O , compared with the measured spectrum (red).	69
5.9	The experimental setup at EAL. A 5" and 10" NEXT prototype stacked together to increase neutron detection efficiency for neutrons above 5 MeV.	70
5.10	The neutron TOF spectra for stacked detectors measured at EAL using $^{27}\text{Al}(\text{d},\text{n})$ reactions at 120° before the TOF correction (black) and after the TOF correction (red). The labels on the neutron peaks on the red histogram represent the corresponding excitation energies in keV in the residual nucleus ^{28}Si taken from previous $^{27}\text{Al}(\text{d},\text{n})$ and $^{27}\text{Al}(\text{d},\text{n}\gamma)$ measurements.	71

5.11	The decay scheme of ^{106}Nb . The β decay of ^{106}Nb populates the neutron unbound states in ^{106}Mo , which finally decay to the ground state of ^{105}Mo via neutron emission.	72
5.12	Silicon Photomultiplier-based miniature plastic scintillator detector (inset in the lower left) situated behind the front of the tape system where ions are implanted.	73
5.13	Arrangement of the 5 NEXT modules around the beam implant point at the focal plane of Modular Total Absorption Spectrometer (MTAS).	74
5.14	The ^{106}Nb neutron TOF spectrum before the TOF correction (black) and after the TOF correction (red). After the correction, a defined peak at ~ 760 keV (25 ns) is observed. As the transit time for 760 keV neutron to traverse the detector thickness (~ 5 cm) is about 4 ns a clear shift of 4 ns in TOF is seen after the correction in the 25 - 29 ns time range.	75
6.1	Schematic diagram showing the single-particle states with Wood-Saxon potential and the splitting with the inclusion of spin-orbit interaction.	78
6.2	Schematic diagram showing the occupation of the single-particle states in ^{24}O	80
6.3	A schematic diagram of NSCL's Coupled Cyclotron Facility and A1900 fragment separator.	82
6.4	Identification of the nuclei produced in the Experiment. The nuclei were identified using the time of flight between silicon detectors and the energy loss in the dE detector. ^{24}O is highlighted in red.	82
6.5	The experimental setup at NSCL. The setup comprised of implant detector, neutron detector arrays (VANDLE and NEXT) and γ ray detectors (Clovers).	84
6.6	(a) A schematic showing the ion implantation and subsequent beta particle emission. (b) An illustration of the ion-beta correlation. The ion and β events within a given correlation radius were considered valid events in the analysis.	86
6.7	Ion(a) and Beta(b) position profiles.	87
6.8	Possible ^{24}O decay chain leading to the stable nuclei indicated by black boxes.	89
6.9	The decay curve for ^{24}O fitted with Bateman equations.	90

6.10	The decay curve obtained for ^{24}O with the ion-beta correlation window of -500 to 500 ms. The decay curve sits on the huge background, which arises due to the random correlation with other implanted ions. The random background has a slope going upward towards $T_\beta - T_{ion} = 0$. The slope is due to the beam fluctuation during the experiment.	91
6.11	γ ray spectrum following the decay of ^{24}O occurring within 500 ms of implantation.	92
6.12	Schematic diagram of ^{24}O decay and consequent β -delayed neutron emission.	94
6.13	A screenshot of the GEANT4 graphical user interface showing experimental setup with all detector systems and supporting materials.	94
6.14	The simulated TOF spectrum for NEXT array for 1 MeV neutrons fitted with an asymmetric Lorentzian-shaped function plus three exponential decay tails. The inset shows the TOF spectrum zoomed around the TOF centroid.	96
6.15	^{17}N β -delayed neutron time-of-flight spectrum (black) fitted with detector response function. The total fitting function is represented in red, and the contribution from individual neutron peaks are shown in blue. a) for VANDLE and b) for NEXT.	97
6.16	Neutron singles TOF spectrum for a) VANDLE and b) NEXT within 500 ms of ion-beta correlation time window with the total fitting function plotted in red. Also, a contribution from the individual peak is shown in blue for VANDLE and black for NEXT. The dotted black line represents the background. The energy obtained from VANDLE spectrum deconvolution was used as a fixed parameter for NEXT spectrum deconvolution.	98
6.17	The experimental Gamow-Teller transition reduced matrix elements (B(GT)) for observed 1^+ states in ^{24}F	100
6.18	Comparison of the experimental ^{24}F energy levels with shell model calculations using standard USDA and USDB interactions and IMSRG. The states which are accessible to the Gamow-Teller transitions (1^+ states) are shown in red.	101
6.19	a) Comparison of the experimental B(GT) with shell model calculations using standard USDA and USDB interactions and IMSRG. b) Cumulative B(GT).	102

Chapter 1

Introduction

With the advancement of modern radioactive ion beam facilities, the number of rare isotopes synthesized in laboratories has constantly been increasing. As a result, the nuclear landscape expanded rapidly in the N-Z plane with the increasing accessibility of such rare isotopes, often referred to as exotic nuclei. They have different combinations of neutron and proton numbers than the stable nuclei. More than 3000 radioisotopes have already been identified, pushing the experimentally accessible territory toward the limit of nuclear stability. One of the main topics in nuclear physics is the study of the nuclear properties of these isotopes, which already have revealed a variety of novel phenomena, for instance, the evolution of shell structure [1, 2], location of the drip line [3, 4], and the neutron halos [5].

The nuclear properties of rare isotopes can be extracted using various complementary experimental approaches. The study of nuclear decay has been an important aspect of nuclear physics since the first discovery of radioactivity. Radioactive decay is a process by which an unstable nucleus releases energy via the emission of various radiation types: particles and gamma rays. Alpha, beta, and gamma decay are the most common types of nuclear decay. But far from nuclear stability, nuclear decay processes become more complex, and new decay modes open up. In such cases, for instance, β decay may be followed by particle emission from the unbound excited states of the daughter nuclei. Also, when the nucleon separation energy becomes negative approaching the drip line, particle emission may occur from the ground state, for example, two-proton radioactivity [6]. This dissertation is focused on studying the complex β decay of very neutron-rich nuclei.

The next generation of radioactive ion beam facilities is needed to expand access to very neutron-rich nuclei. The Facility for Rare Isotope Beams (FRIB) at Michigan State University (USA) and Radioactive Isotope Beam Factory (RIBF) at RIKEN (Japan) are some facilities capable of delivering the most intense radio-isotope beams for the study of exotic nuclei. An important method to study neutron-rich nuclei is through nuclear decay. β decay and subsequent β -delayed neutron emission are the dominant decay mode for the neutron-rich nuclei. Studying β decay and neutron emission provides insights into the nuclear structure of neutron-rich nuclei and modeling of nuclear astrophysical processes.

This dissertation describes the development and characterization of the new high-resolution neutron detector to study the neutron-rich nuclei and β -delayed neutron emission studies of ^{24}O . A new neutron detector is developed, constructed, and characterized for the precise and efficient measurement of β -delayed neutrons. ^{24}O , as a doubly magic drip-line isotope of Oxygen, is an excellent case to study nuclear structure and neutron emission mechanism near the neutron drip line.

1.1 β decay

β decay is a dominant decay mode for most of the unstable nuclei. The proton-neutron asymmetry causes the nucleus to undergo β decay. For the neutron-rich nuclei (more neutrons compared to the proton), β^- decay takes place; whereas for the neutron-deficient nuclei, β^+ decay occurs. The $\beta^-(\beta^+)$ is a weak interaction process mediated by $W^-(W^+)$ boson where neutron (proton) converted into a proton (neutron) with the emission of an electron (positron) and electron anti-neutrino (electron neutrino). Systematically, these two processes can be expressed as:

$$\beta^- : \quad {}^A_Z X_N \rightarrow {}^A_{Z+1} Y_{N-1} + e^- + \bar{\nu}_e \quad (1.1a)$$

$$\beta^+ : \quad {}^A_Z X_N \rightarrow {}^A_{Z-1} Y_{N+1} + e^+ + \nu_e \quad (1.1b)$$

where e^- and e^+ are electron and positron, and ν_e and $\bar{\nu}_e$ are electron neutrino and electron antineutrino, respectively, generated just at the moment of the nuclear decay by the weak interaction between the nucleons (proton and neutron) at the quark level. The decay energy

($Q_{\beta\pm}$) which is the energy released as kinetic energy of final products can be calculated using the atomic masses of parent and daughter nuclei:

$$Q_{\beta^-} = [m({}_Z^A X_N) - m({}_{Z+1}^A Y_{N-1})]c^2 \quad (1.2a)$$

$$Q_{\beta^+} = [m({}_Z^A X_N) - m({}_{Z-1}^A Y_{N+1}) - 2m_e]c^2 \quad (1.2b)$$

An important quantity extracted in the β decay is a strength distribution, which is the overlap between the initial parent state and all the states in the daughter nucleus. The strength distribution is directly related to the nuclear structure of the nuclei and also determines the decay rate. The β decay rate can be calculated using the formalism of the β decay strength function, $S_\beta(E)$, as follows [7]:

$$T_{\frac{1}{2}}^{-1} = \int_0^{Q_\beta} S_\beta(E_i) \times f(Z, Q_\beta - E_i) dE_i \quad (1.3)$$

where,

$$S_\beta(E_i) = |\langle \psi_f | \hat{O} | \psi_{parent} \rangle|^2 \quad (1.4)$$

E_i and Q_β are the excitation energy in the daughter nucleus and the β decay energy window, respectively. The Fermi integral, $f(Z, Q_\beta - E_i)$, takes into account the influence of the nuclear Coulomb field and the 3-body decay phase space.

1.1.1 Allowed and Forbidden Decays

In the allowed β decay, the lepton pair do not carry away any orbital angular momentum ($\Delta l = 0$). The change in angular momentum of the nucleus (ΔI) comes from the intrinsic spins of electron (positron) and anti-neutrino (neutrino); each has spin of $\frac{1}{2}$. The total spin can be 0 or 1, depending on the spin alignment of leptons. If the spins of electron (positron) and anti-neutrino (neutrino) are anti-parallel (total $S = 0$), which is known as a Fermi decay, there is no change in the total angular momentum of the nucleus ($\Delta I = 0$). If the lepton spins are parallel (total $S = 1$), which is known as Gamow-Teller decay, the total angular momentum of the nucleus changes by 0 or 1 unit ($\Delta I = 0$ or 1; except $I_i = I_f =$

0, which can only occur via Fermi-type transition). Since leptons do not carry any orbital angular momentum, there is no change in parity between initial and final nuclear states in allowed decays. A dominant transition of interest in neutron-rich nuclei is the Gamow-Teller transition.

Forbidden decays are usually less probable than allowed decays. In this decay mode, the lepton pairs carry away non-zero orbital angular momentum from the nucleus ($\Delta l > 0$) and results in a change in parity if Δl is odd. The order of forbiddenness depends on the units of angular momentum carried by the lepton pair. The spin and parity selection rules for allowed and forbidden decays are summarized in Table 1.1.

1.2 β -delayed neutron emission

Away from the line of β -stability towards the neutron-rich side, β decay energy (Q_β) increases, and the neutron separation energy (S_n) decreases with the addition of neutrons. In such cases, β decay is generally followed by neutron emission. Figure 1.1 shows a chart of nuclei with $Q_\beta - S_n$ values. The $Q_\beta - S_n$ increases with the neutron number, increasing the possibility of neutron emission.

β -delayed neutron emission was first observed by R. Roberts et al. during the fission studies of Uranium and Thorium isotopes [8]. It is a two-step process, β decay, and neutron emission, as shown schematically in Figure 1.2. Because of large $Q_\beta - S_n$ for neutron-rich nuclei, the β decay of the parent nucleus can have access to the excited states in the daughter above neutron separation energy. When states above neutron separation energy are populated in the β decay, the nucleus de-excites via neutron emission rather than gamma-ray emission, called the “ β -delayed neutron emission”. The decay fraction leading to the neutron emission is called the β -delayed neutron emission probability P_n . Since the energy window for the neutron emission ($Q_\beta - S_n$) increases with the neutron number, there is a possibility of multineutron emission towards the drip line as indicated in Figure 1.3. The parent nucleus of β decay preceding delayed neutron emission is generally referred to as the “precursor” and the daughter as the “emitter” in the following text.

Table 1.1: Allowed and forbidden decays selection rules.

Transition	Δl	ΔI	change in parity
Fermi	0	0	no
Gamow-Teller	0	0,1 (no $0 \rightarrow 0$)	no
First Forbidden	1	0,1,2	yes
Second Forbidden	2	1,2,3	no
Third Forbidden	3	2,3,4	yes
Fourth Forbidden	4	3,4,5	no

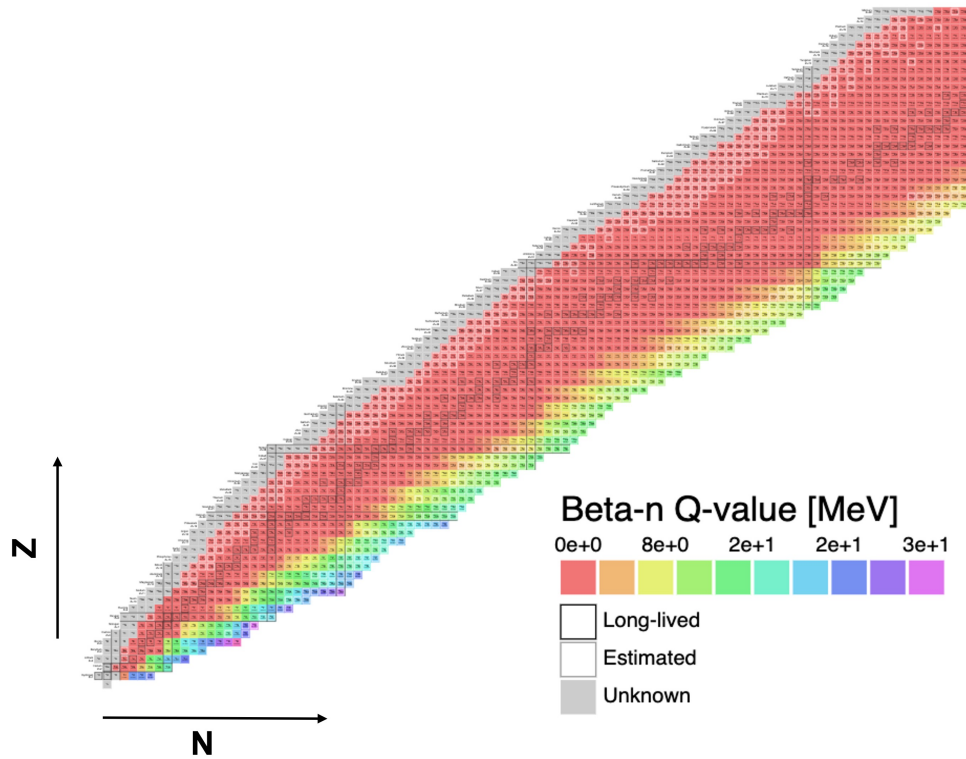


Image credit: <https://people.physics.anu.edu.au/~ecs103/chart/>

Figure 1.1: A chart of nuclei showing $Q_\beta - S_n$ values.

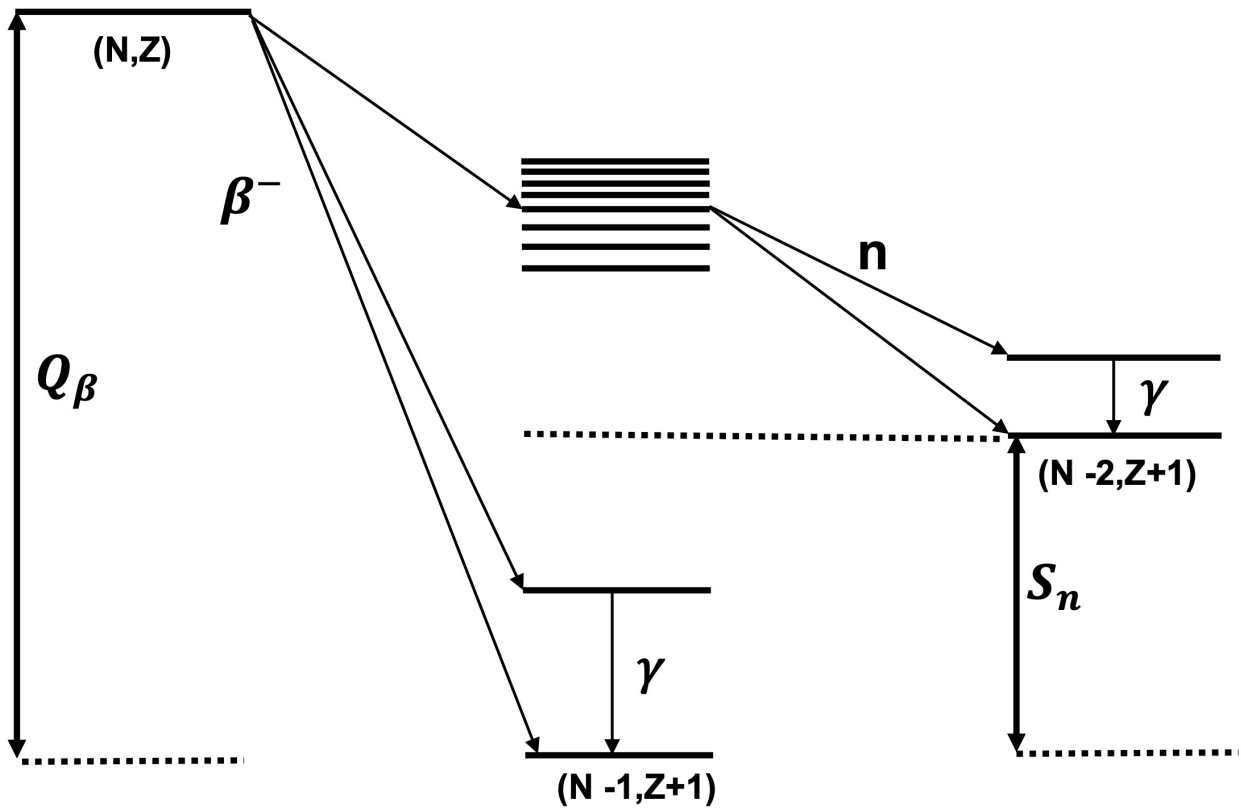


Figure 1.2: Schematic of a β -delayed neutron emission process.

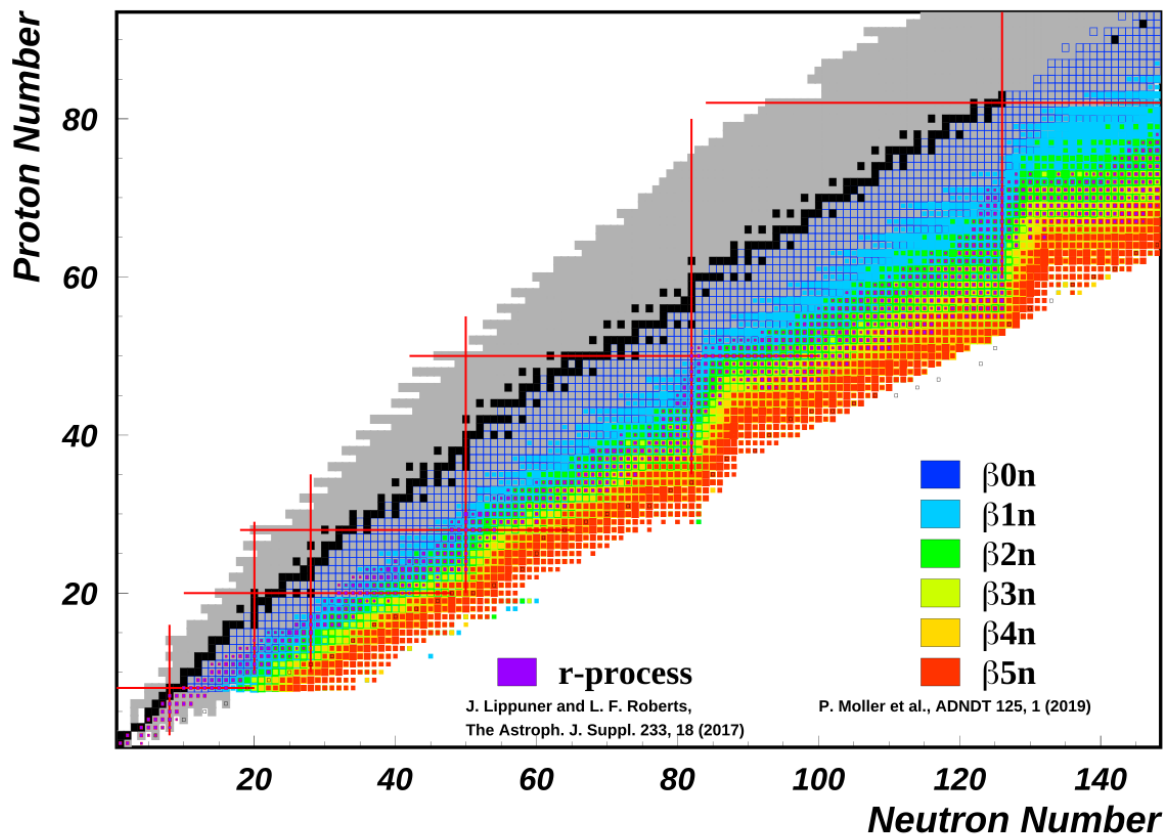


Figure 1.3: A chart of nuclei with the prediction of multineutron emission towards the drip line.

β -delayed neutron emission plays a vital role in studying the nuclear properties of neutron-rich nuclei. It is an essential tool for obtaining the nuclear structure information for neutron-rich nuclei far from the valley of β -stability [9, 10, 11]. The emitted neutrons carry information about the excited states above neutron separation energies, and a precise energy measurement is crucial for the deconvolution of the high-density states. The β decay strength function is extracted from the neutron energy measurements and used to determine the decay rates, which are the key input parameters in the r-process calculations. The strength function also provides a more direct test of nuclear models used in nuclear structure and astrophysical calculations.

1.2.1 Models of β decay and β -delayed neutron emission

The models used in the studies of β -delayed neutron emission can be categorized into two different approaches. The first approach utilizes the models based on systematics, for example, the Kratz-Herman formula [12] or ones using the Gross Theory of β decay [13]. The gross theory provides an early model of the nuclear β decay strength distribution. It considers the sum of the strengths of transitions from the initial state to the final states and generates a continuum distribution of strengths based on the general properties of Gamow-Teller giant resonance. The properties of β decay, like decay rates and P_n values, are calculated based on the position and width of the giant Gamow-Teller resonance for all nuclei. But, they do not provide information on the underlying nuclear structure or the wave functions.

The second approach uses the microscopic models of β decay. These models use effective nuclear interactions and solve the Schrodinger equation to obtain varieties of nuclear properties, for example, level energies, ground state shapes, spin and parities, decay rates, P_n values, etc., within a single framework. The Quasi-particle Random Phase Approximation (QRPA) [14] and the nuclear shell model are some examples that are based on the microscopic description.

In the QRPA framework, the β decay of the precursor nucleus to the neutron emitter is studied by solving the Schrodinger equation for the nuclear wave function and single-particle energies using folded-Yukawa potential. These calculations include additional residual interactions, pairing, and Gamow-Teller interactions, to obtain the Gamow-Teller decay

matrix element (B(GT)) from the initial to the final state. A β decay strength function, which defines the squares of the overlap integral between nuclear wave functions, is then extracted. The most sophisticated microscopic model, the nuclear shell model, is discussed in section 6.1.1.

Neutron Emission Models

The neutron emission branching ratios (P_n values) can be estimated using the formalism of β decay strength distribution, as expressed in Equation 1.5. The basic idea is determining the percentage of β decay strength to the states above various neutron separation energies which provides the maximum probability of delayed neutron emission, as shown schematically in Figure 1.4, often referred to as a “cut-off” model.

$$P_n = \frac{\int_{S_n}^{Q_\beta} S_\beta(E_i) \times f(Z, Q_\beta - E_i) dE_i}{\int_0^{Q_\beta} S_\beta(E_i) \times f(Z, Q_\beta - E_i) dE_i} \quad (1.5)$$

In these calculations, the n - γ competition factor $\frac{\Gamma_n}{\Gamma_n + \Gamma_\gamma}$ is set to one where Γ_n and Γ_γ are the neutron and γ widths, respectively, meaning the γ ray emission from neutron unbound states is neglected. These calculations fail to consider the possibility of one neutron emission from the states above two neutron separation energy. The strong one neutron emission from two neutron unbound states is recently observed for Ga isotopes [15]. This leads to a requirement for more sophisticated models.

The new approach to studying β -delayed neutron emission integrates QRPA and statistical methods into a single framework (QRPA + HF) [16]. In this approach, the β decay of the precursor is treated in QRPA, and the subsequent neutron emission is then studied in the Hauser-Feshbach model as shown schematically in Figure 1.5. The underlying assumption is that the neutron emitter is in an equilibrated state (compound nucleus), and the particle emission is sensitive only to the spin and parity of the emitting state, not the details of its formation. These calculations include the statistical decay of the emitter nucleus and the subsequent decays until the available excitation energy is exhausted.

The neutron transmission coefficients are generally determined by solving the Schrodinger equation for a given optical potential, such as Koning-Delaroche global optical potential [17].

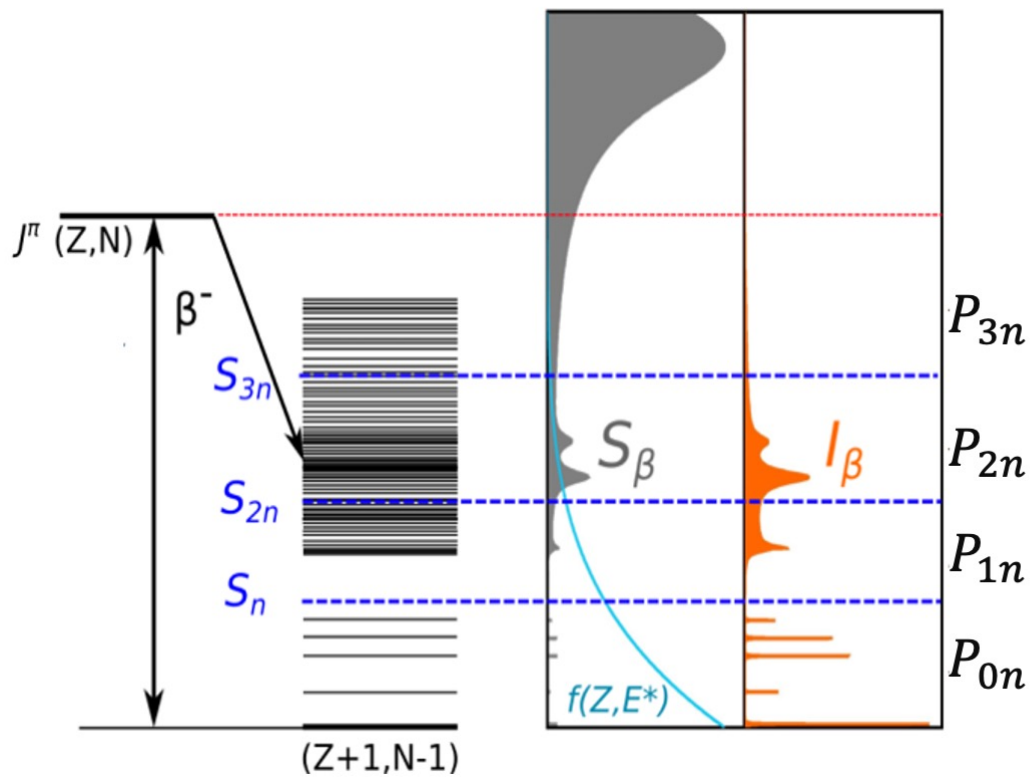


Figure 1.4: Schematic of the cut-off model to determine the neutron emission probabilities. The sum of the strengths to the emitter states above various separation energies gives the maximum probabilities of neutron emission.

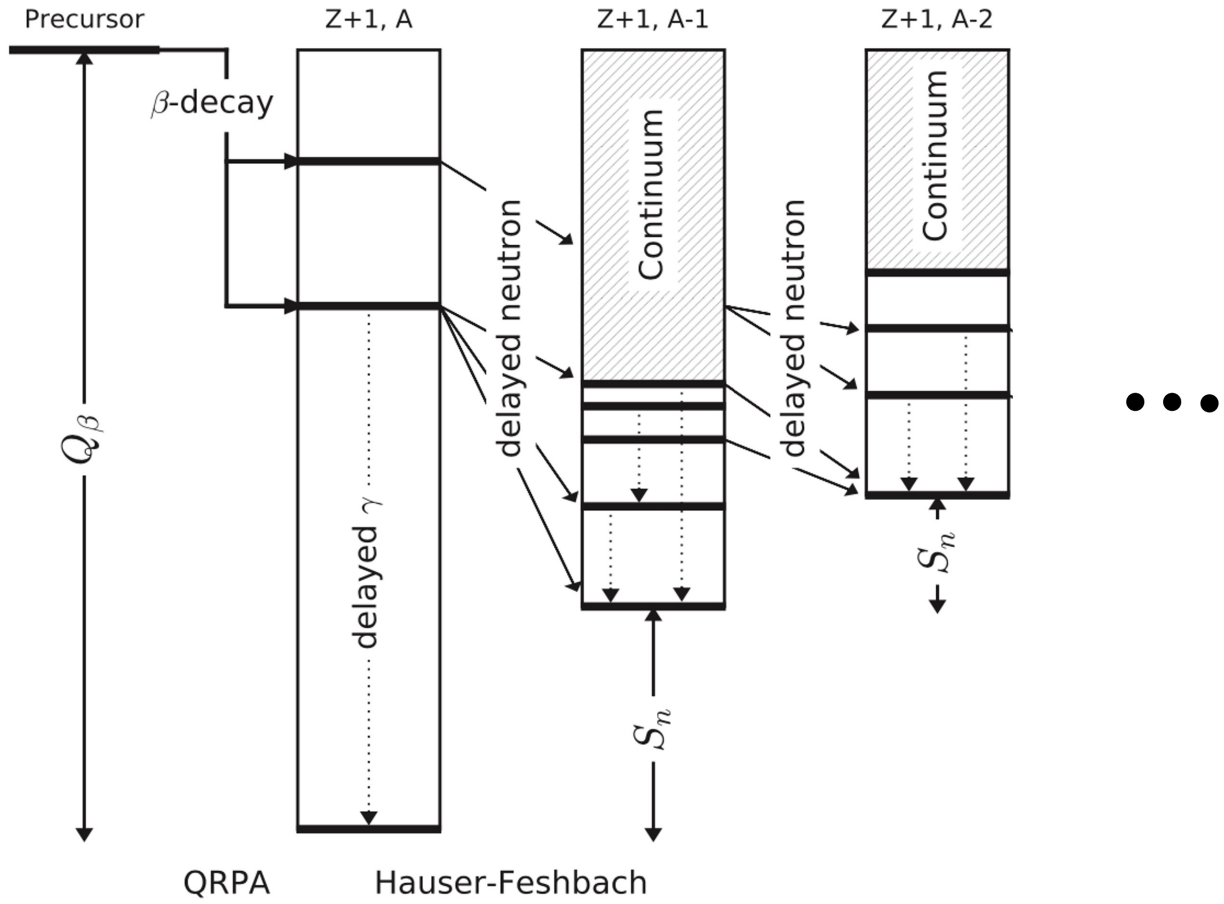


Figure 1.5: Schematic of the QRPA and Hauser-Feshbach approach to study β decay and delayed neutron emission [16]. The β decay of the precursor is calculated by QRPA, and the subsequent delayed neutron and γ emission is treated in Hauser-Feshbach statistical approach.

The excited states in the emitter nucleus can be discrete or in the continuum. If the levels are not experimentally known, Gilbert-Cameron level density formulation is used, which adopted a constant temperature model at low energies and the Fermi gas formula at high excitation energies [18]. The γ ray competition is also included, where the γ transmission coefficients are determined using the generalized Lorentzian γ -strength function (γ SF) for E1 transitions [19]. The compound nucleus hypothesis agrees with recent experimental measurements but needs more data on very neutron-rich nuclei to verify its universality. One of the motivations for studying β -delayed neutron emission is to test the validity of these models for a variety of areas in the chart of nuclei.

1.2.2 Astrophysical Application: The r-process

The synthesis of elements heavier than iron in stars occurs mainly via two nucleosynthesis processes; slow neutron-capture process (s-process) and rapid neutron-capture process (r-process). The s-process path runs close to the valley of β -stability and occurs on a longer time scale than β decay. On the other hand, the r-process involves nuclei on the very neutron-rich side of the nuclear chart and happens on a relatively short time scale. The r-process occurs in extreme astrophysical environments such as recently observed neutron star mergers [20] or during the core collapse of the massive stars [21].

The nuclear mass, neutron capture cross-sections, neutron separation energies, and β decay properties (branching ratios and half-lives) are the key nuclear parameters required to model the r-process nucleosynthesis [22]. β -delayed neutron emission plays an important role during the freeze-out phase after the astrophysical explosion. It provides the additional particles so the neutron capture can proceed and changes the decay paths to β -stability. Without β -delayed neutron emission, the nucleus decays back to the stability line via long β decay chains, but due to single or multiple neutron emissions, the path could go through the neighboring mass chains, as shown in Figure 1.6 for new isotopes at extremes (^{122}Nb , ^{129}Ru) [23]. The final abundance pattern of the r-process nucleosynthesis changes due to the emission of delayed neutrons, shifting towards lower masses. Thus, accurate measurements of half-lives and β -delayed neutron emission probabilities provide necessary data for modeling astrophysical processes.

Many isotopes involved in the r-process nucleosynthesis are not yet experimentally accessible. In such cases, the r-process calculations rely on nuclear model predictions for the nuclear structure properties of unmeasured nuclei. These models require the knowledge of the β decay strength function, which can be calculated in β -delayed neutron spectroscopy. The strength function provides crucial information to constrain the calculations which predict the properties of r-process nuclei.

1.2.3 Applied Research

β -delayed neutron emission also plays an important role in nuclear technology, such as reactor operation and decay heat calculations [9]. Accurate description and measurement of the prompt and delayed neutron spectra and multiplicities are critical for reactor design and safety management. Neutron detection is also integral to nuclear security, neutron radiography, and neutron interrogation techniques.

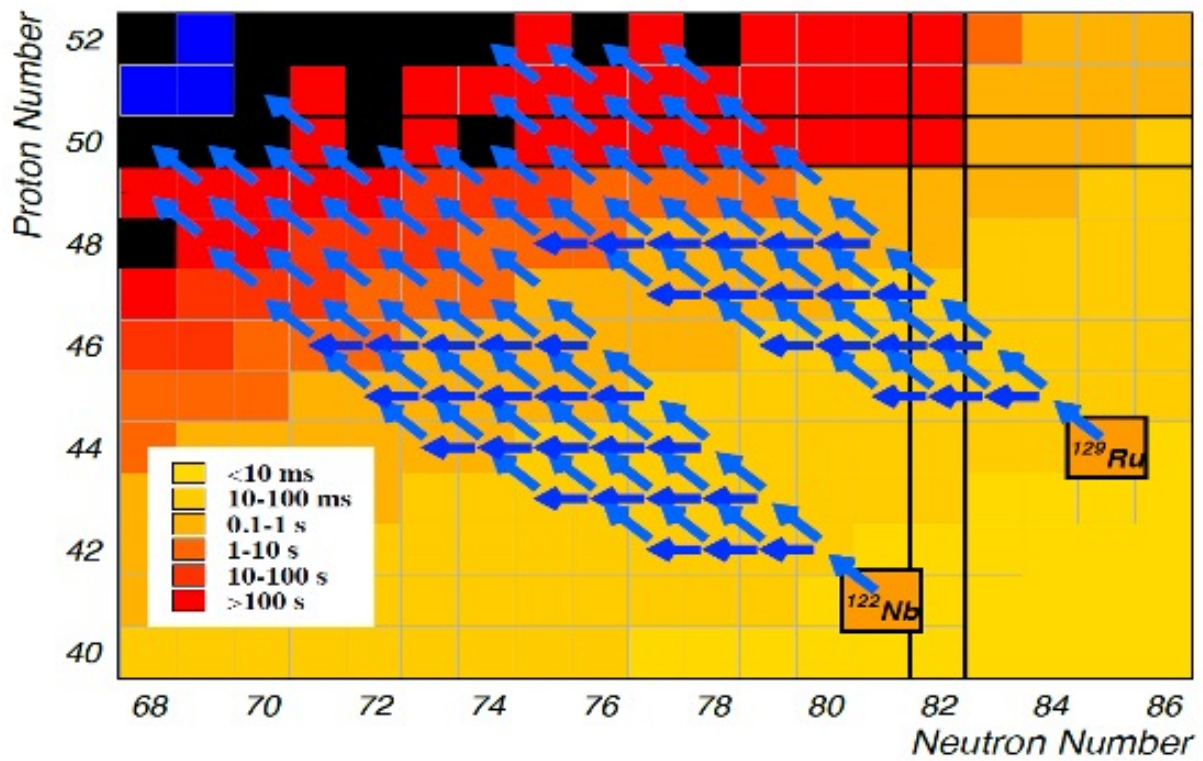


Figure 1.6: An example showing the effect of β -delayed neutrons in the decay path towards the β -stability [23].

Chapter 2

Neutron Detectors

2.1 Neutron Detection Mechanism

Neutron, as a neutral particle, does not interact electromagnetically with electrons in matter. So, the neutron detection mechanism has to be based on indirect methods. The neutrons can be detected when they interact with nuclei in detector material and generate charged particles. The ionization caused by the charged particles produced a light pulse. The light pulse is then detected by photo-sensors optically coupled to the scintillator, and information about the incident neutron will be obtained.

Neutron detection is based on two basic types of interaction. First, the neutron scatters off the nucleus in the detection material and transforms some of its energy into the nucleus. The energy of recoiling of the nucleus is converted into scintillation light. This method is only effective when neutrons interact with light nuclei, namely hydrogen and helium. Second, the incident neutron will initiate reactions in the detector material that lead to the production of secondary particles such as protons, alpha particles, gamma rays, and other residual products. Detecting these particles will give information about the incident neutron. Modern neutron detectors exploit either recoil or reaction mechanisms to detect neutrons and employ solid/liquid scintillators or gas-filled mediums.

2.2 Neutron Detectors in Decay Studies

The neutron detectors used in the study of β -delayed neutron emission are based on either neutron counting or energy measurement. The detectors based on neutron counting employ either ${}^3\text{He}$ or BF_3 filled tubes. BEta deLayEd Neutron (BELEN) detector at JYFL and GSI [24], 3Hen at ORNL [25], β -delayed neutron measurements at RIKEN (BRIKEN) [26], and the Neutron Emission Ratio Observer (NERO) at NSCL [27] are some examples of currently available neutron counters. These detectors are comprised of several gas-filled counters embedded in a neutron moderator and detect the neutrons via either ${}^3\text{He}(n,p){}^3\text{H}$ or ${}^{10}\text{B}(n,\alpha){}^7\text{Li}$ reactions. Since the detectors take advantage of high-detection efficiency by moderating the incoming neutrons, the information about initial neutron energy before moderation will be lost.

The other detector types measure neutron energy. The neutron energy detectors are based on time-of-flight or ion chambers. The time-of-flight detectors use plastic, liquid, or ${}^6\text{Li}$ -glass scintillators. The Versatile Array of Neutron Detector at Low Energy (VANDLE) [28] and the Low Energy Neutron Detector Array (LENDa) [29] are some examples of currently available plastic scintillator-based neutron time-of-flight detector arrays. The time-of-flight technique, which is a focus of this dissertation, is detailed in the next section. ${}^3\text{He}$ neutron spectrometers are the examples of the ion-chamber-based detectors to measure the neutron energies [30].

Recently, recoil-ion spectroscopy has been implemented to perform β -delayed neutron spectroscopy using trapped ions. One example is Beta-decay Paul Trap (BPT) [31, 32]. In this technique, the neutron energy spectrum is reconstructed by measuring the time-of-flight of the recoil ion following the neutron emission [33]. Deuterated scintillator-based detector arrays are also in use to detect the fast neutron using the spectrum unfolding technique. The Deuterated Scintillator Array for Neutron Tagging (DESCANT) at TRIUMF [34] and ORNL Deuterated Spectroscopic Array (ODeSA) [35] are some examples of such detector arrays.

2.3 Time-of-Flight Technique

The detectors which employ the neutron counting technique have high detection efficiency and are insensitive to γ rays but have to slow down the neutrons to the thermal energy before they can be detected. In that case, the knowledge of neutron energy before slowing down will be lost. An alternative technique of neutron detection is via scintillation using organic scintillators, namely plastic and liquid scintillators. Plastic scintillators are more common because of their flexibility in use and relatively cheaper compared to other organic scintillators. They are commercially available in various shapes and forms and can be easily shaped into desired forms if necessary. A good scintillator should have relatively high scintillation efficiency, transparent to its own radiation and be spectrally matched with the photosensor's response.

Neutrons interact with scintillator material via elastic scattering with the nuclei, mainly hydrogen (proton) and carbon. The kinetic energy of recoiling nuclei is converted into visible light and will be detected for further processing. The neutrons incident on the scintillator might not lose all its energy in a single interaction. To entirely stop the neutron, it might need an excessive amount of scintillator material which makes the detector array large and expensive. But because of the availability of fast scintillators (fast signal rise and decay times), it is possible to measure neutron energy via precise timing measurements referred to as a neutron time-of-flight technique. In this detection technique, the TOF is measured between a trigger detector, which provides the start time, and a neutron detector, which provides the stop time, over a specific flight path length, as shown schematically in Figure 2.1. The energy is then computed classically using Equation 2.1.

$$E_n = \frac{1}{2}mv^2 = \frac{1}{2}m\left(\frac{L}{TOF}\right)^2 \quad (2.1)$$

Where $m = 939.56 \frac{MeV}{c^2}$ is the mass of a neutron, and L is a flight path over which TOF is measured.

2.4 Neutron-Gamma Discrimination

One disadvantage of using a scintillator-based neutron detector is that it is sensitive to γ radiation. Scattered γ rays are the main source of background in this kind of detector. For precise neutron spectroscopy, the particles that are not of interest might need to be rejected; the process is called neutron-gamma (n- γ) discrimination.

Organic scintillators can have prompt and delayed fluorescence - called fast and slow components of the scintillation light. The major component of the scintillation is the prompt fluorescence, but a slower longer-lived component is also observed, which corresponds to the delayed fluorescence. The fast component has a characteristic decay time of a few tens of nanoseconds, while the slow component typically has a decay time of about a few hundred nanoseconds. The total light output is usually the sum of these two exponential decay components. The amount of light emitted during the delayed fluorescence often depends on the nature of the incoming particle; heavier particles produce more delayed fluorescence. Figure 2.2 shows the scintillation response produced by different incoming radiation particles in Stilbene, which is a solid organic crystal scintillator. By exploiting this dependence, one can distinguish between particle types that have a different rate of energy loss but produce the same amount of scintillation. While using an organic scintillator as a neutron detection, this technique is commonly used to reject γ ray-induced events from neutron events.

Many commercially available organic scintillators can provide good n- γ discrimination. Stilbene, para-terphenyl and liquid scintillators are commonly in use. Recently, the neutron-gamma discrimination capability is also incorporated in many commercially available plastic scintillators.

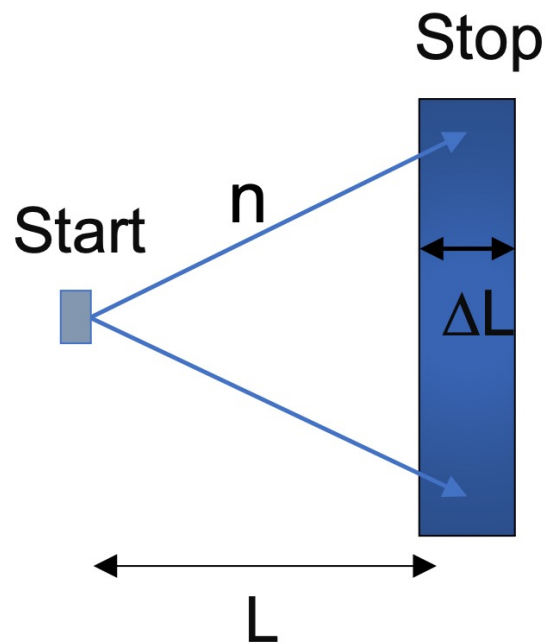


Figure 2.1: Schematic of the neutron time-of-flight technique with “straight” shape scintillators. The time-of-flight of the neutron is measured between the start detector and the neutron detector (stop) over a specific flight path length L .

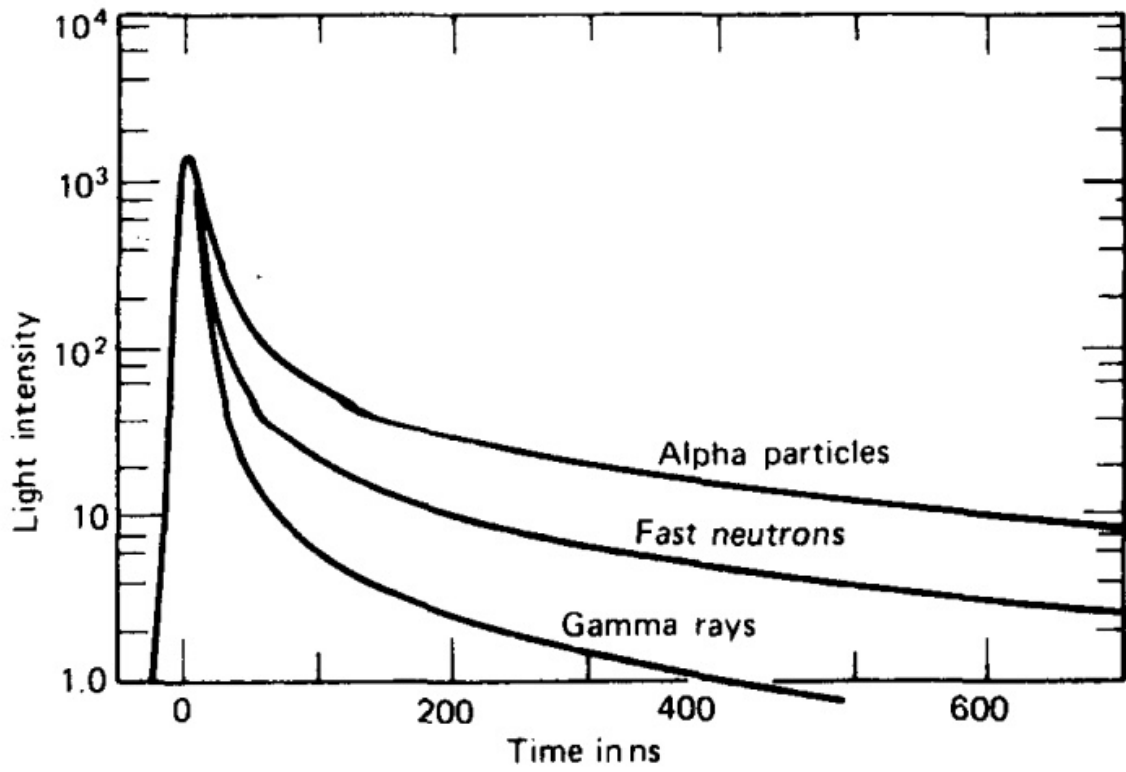


Figure 2.2: Scintillation response of the organic scintillator for different exciting particles. The figure is adapted from J.F. Knoll [36].

Chapter 3

Development of New High-Resolution Neutron Detector

Experimental studies of β -delayed neutron emitters are difficult because of challenges in the production of short-lived neutron-rich nuclei. However, the new capabilities of next-generation radioactive ion beam facilities allow us to access very neutron-rich nuclei [37]. Because of the low production rate of neutron-rich exotic nuclei, identifying the single or multiple β -delayed neutron emitters and extracting their nuclear properties requires an efficient and high-energy resolution neutron detector system.

Very few available neutron detector arrays are capable of measuring neutrons of energy range 100 keV to 10 MeV. They also lack some important aspects of neutron detection, like neutron-gamma discrimination, better energy resolution, and high detection efficiency. In this light, a neutron detector array that incorporates all these aspects of neutron detection will be needed for the future study of exotic nuclei. A new detector concept, Neutron dEtector with Xn Tracking (NEXT), has been developed to fulfill this necessity.

3.1 NEXT Concept

The energy of the β -delayed neutrons can be measured using the time-of-flight technique, as detailed in Section 2.3. While measuring energy using this method, the energy resolution

depends on the timing resolution and the uncertainty in flight path length, as expressed by Equation 3.1.

$$\frac{\Delta E}{E} = \sqrt{\left(\frac{2\Delta T}{T}\right)^2 + \left(\frac{2\Delta L}{L}\right)^2} \quad (3.1)$$

Where ΔT is the uncertainty in the neutron TOF, T , and ΔL is the uncertainty in the neutron flight path, L . The uncertainty in the flight path mainly arises due to a lack of precise determination of the neutron interaction position in the detector. Basically, the uncertainty in the flight path length is determined by the thickness of the detector. Since the neutron detection efficiency is directly proportional to the thickness, the thick detector will have higher detection efficiency but at the expense of energy resolution. Figure 3.1 shows how the energy resolution changes with the detector thickness calculated using Equation 3.1. There is always a trade-off between efficiency and resolution. One possible way of improving the energy resolution is to make the flight path length longer, which in turn reduces the solid-angle coverage and efficiency. The measurements with rare isotopes require a detector with efficiency as high as possible because of the very low production rate. The large array could have higher geometric efficiency, which makes the detector prohibitively expensive.

NEXT uses the idea of optically segmenting the active detector volume along the direction of the neutron flight path. Segmenting the detector will reduce the uncertainty in the flight path determination by localizing the neutron interaction position in the detector in the TOF measurement. The segmentation is implemented along the x and y axes with higher segmentation along the neutron flight path direction (x-axis), as shown schematically in Figure 3.2 with possible segmentation. This significantly improves energy resolution without losing detection efficiency. NEXT also incorporates the neutron- gamma (n- γ) discrimination which allows performing measurements in high background conditions. The details of the conceptual design and the first results from the proof-of-principle measurement are reported in the Reference [38].

3.2 NEXT Modules

A typical NEXT Module has 4×8 segments (eight layers/columns and four rows), where the higher segmentation is along the neutron flight path. Each segment is a bar of plastic scintillator developed by Eljen Technologies [39]. The 6 mm thick, 12.7 mm wide, and 254 mm (10 inches) long segments are assembled to form a scintillator array of active scattering volume of $48 \times 50.8 \times 254$ mm³. The individual scintillator bars are optically separated from the others using a double layer of 3MTM Enhanced Specular Reflector(ESR) [40]. The scintillator array is coupled to a multi-anode photomultiplier tube (MAPMT), Hamamatsu H12700 [41], on either side for light readout. H12700 MAPMT has 8×8 6×6 mm² pixels with an effective area of 48.5×48.5 cm², as shown in Figure 3.3. A fully assembled detector can be seen in Figure 3.4 with the details of the segmentation.

Two plastic scintillators manufactured by Eljen Technologies, EJ-200, and EJ-276, were used to construct the modules. The EJ-276, with a scintillation efficiency of 8600 photons per 1 MeV e^- , is an n- γ discriminating plastic, while EJ-200 does not have any n- γ discrimination capabilities, but it has about 15% higher light yield than EJ-276 (10000 photons per 1 MeV e^-). The modules are designated by the plastic type and length; for instance, EJ276-10 is made of EJ-276 plastic scintillator and 10 in long in the following text.

The signals from the MAPMT are read out using Anger Logic boards, designed and manufactured by Vertilon Corporation [42]. The Anger Logic board, an array of matched resistors, significantly reduces the number of readout channels to five per MAPMT; four anode signals for neutron interaction position analysis and a dynode signal for timing and pulse-shape analysis. The details of the signal readout scheme can be found in Section 3.3. The signals from each Anger Logic board are recorded using 16-bit, 250 MHz Pixie-16 digitizers developed by XIA LLC [43]. Pixie-16 has 16 input channels per module, as shown in Figure 3.5, and allows to perform coincident data acquisition across the channels and modules.

3.3 Readout scheme of NEXT

Each MAPMT used for the light readout provides one common dynode and 64 anode signals. The common dynode signal, shown in red in Figure 3.6, is used for timing, pulse-shape analysis, and triggering purposes, enabling an evolved implementation of the trigger scheme developed initially for VANDLE [44]. The 64 anode signals are routed to the Anger logic resistive network, as shown schematically in Figure 3.7 [42]. Using charge division, four anode signals, for instance, L1 to L4 in Figure 3.6 (labeled by V1, V2, V3, and V4 in Figure 3.7), generated at the corners of the resistor network. These signals will be used to extract high-resolution position determination, as explained in Section 3.5.

Anger logic provides a cost-effective readout method of a pixelated array like NEXT because only ten electronic channels are needed to read 128 anodes and two dynodes per detector. However, there are challenges in using the resistive network readout, especially for neutrons that deposit very little energy in the scintillator. As a result of charge division, the low-energy signals can be lost when their amplitude becomes too small. This is often the case when the interaction takes place close to the edge of the detector.

3.4 High-Resolution Timing Analysis

High-resolution timing measurement is a critical part of NEXT development. The timing of the digitized signals extracted from the pixie timestamps will have the timing resolution corresponding to the sampling frequency of the digitizer, for instance, 4 ns for the 250 MHz digitizer. To extract sub-nanosecond timing resolution, the high-resolution-timing (HRT) analysis is performed on the digitized dynode signals using the polynomial Constant Fraction Discrimination (polyCFD) algorithm [45], as shown graphically in Figure 3.8. The algorithm first finds the maximum of the digitized trace from the third-order polynomial fit around the peak. It then sets the CFD threshold as a fraction of the difference between the maximum of the trace and the baseline. The phase of the trace is determined by the crossing point of the linear interpolation between the points around the CFD threshold in the leading edge of the digitized trace and the CFD threshold. Generally, the CFD threshold fraction is set

between 40-50% for the optimal timing. The HRT of the digitized trace is then determined using Equation 3.2.

$$HRT = timestamp - tracedelay + phase \quad (3.2)$$

3.5 High-Resolution Position Analysis

The neutron flight path depends on the scattering position as it traverses through the detector volume. High-resolution position determination is required to extract the proper flight path length. Because of the optical segmentation, NEXT can localize the neutron interaction position, which enables precise position determination. The position information is provided by four anode signals read at the corner of the resistive circuit 3.7. Anger logic algorithm [46], widely used in medical physics for radiation imaging [47], is adapted to extract the position image. Using the notations in Figure 3.6, two-dimensional (X and Y) coordinates for the centroid of the photon distribution arriving to the MAPMT are calculated using Equations 3.3a and 3.3b.

$$X = \frac{(L_1 + L_4) - (L_2 + L_3)}{L_1 + L_2 + L_3 + L_4} \quad (3.3a)$$

$$Y = \frac{(L_1 + L_2) - (L_3 + L_4)}{L_1 + L_2 + L_3 + L_4} \quad (3.3b)$$

Where $L_1 - L_4$ denote the integral of the pulse within a given time range for each anode signal. Figure 3.9 shows an example of a position profile determined using this approach, where the pixels represent the detector segmentation. This position information will be used to correct the TOF for the flight path. The correction procedure and improvements in the energy resolution after correction is demonstrated in Chapter 5.

3.6 Trigger configurations

A coincidence triggering is required to operate the detector system with a low energy threshold without saturating data acquisition. Two types of trigger configurations are

incorporated in the Pixie-16 firmware to enable the coincidence measurements in the time-of-flight setting: triple coincidence trigger and external fast trigger mode.

The triple coincidence mode generates two types of coincidence triggers: pairwise channel and global triggers. The pairwise triggers are generated between two neighboring channels (0&1, 2&3, ...) where signals from the left and right sides of the detector are connected. This approach is already advantageous in reducing detection thresholds in double-ended neutron TOF detectors. To further reject background events, a global trigger can be generated based on the TOF pairwise triggers that are coincident, within a specified time window, with channels corresponding to TOF start signals, as shown in Figure 3.10a. The start signals can either be a real observation of a β particle scattering in a plastic scintillator, a gamma from a fission source, or an RF signal tightly correlated with a beam packet arrival on a reaction target. Once a global trigger has been generated, any channel whose local fast trigger is validated alongside the global trigger records the channel event data to the FIFO.

Figure 3.10b shows the schematics of the triple coincidence trigger configuration. The caveat to this trigger mode, when used with NEXT, is that the anodes, which should always be in coincidence with dynodes of the same detector, may not be recorded if the signals are too small to cross their local trigger threshold. Usually, this could be remedied by simply lowering their threshold to near zero, but these anodes not only listen to the global triggers but can also generate global triggers. If the anodes are set to near-zero thresholds, then too many global triggers would be generated, and the data rate would be unsustainable. Also, a proper data analysis requires four anode signals corresponding to each dynode. If any of the four anode signals do not exist, then the event is discarded. For events with low energy deposition localized near the corner of the detector, sharing the signal through the Anger logic resistive network will result in the opposite corner likely not triggering because its signal will be too small. This may result in a relatively high detection threshold in the measurement.

Another trigger scheme is available in the Pixie-16 firmware based on an unconditional readout trigger called external fast trigger mode. This allows the forced recording of a channel if a global trigger is generated. In this scheme, anodes do not contribute to generating the coincidence triggering; they are set to the external fast trigger mode such that they are

recorded whenever there is a global trigger generated between the TOF start signals and a pairwise trigger, as shown schematically in Figure 3.10c. This triggering scheme is very advantageous in improving the detection threshold. The experimental demonstrations of the effects of these triggering schemes are presented in Chapter 4.

3.7 Signal Readout Assembly

The signal readout assembly consists of two identical Anger logic readout PCBs (SIB064-2003) for Hamamatsu H12700 MAPMT and the associated cables, as shown in Figure 3.11 [42]. The cables carrying power to PCBs and high-voltage bias to PSPMTs are connected to the master PCB on the right side of the readout assembly. These cables are routed to the slave PCB on the left side of the readout assembly by jumper cables to power the slave PCB and the MAPMT. The MAPMTs mounted on either side provide 64 anode outputs, which are reduced to four signals using Anger logic and an associated resistive network implemented in each PCB. The onboard preamplifier amplifies the four Anger logic outputs and MAPMT's last dynode to ten times the original pulse height. The five preamplified signals from the slave PCB send off to the master PCB using coaxial jumpers, where they combine with five preamplified signals from the master PCB into the ten-positions coaxial cable, which is connected to digitizers for further processing.

3.8 New Digitizers

In future experiments with NEXT, the signals will be recorded and digitized using 32-channel Pixie modules (updated Pixie-16 modules) called Pixie-16x2, developed by XIA LLC. This high-channel density digitizer is designed explicitly for NEXT to handle a large channel density but can also be used with any other detector type with a slight modification in the firmware. The significant upgrades compared to Pixie-16 are replacing the FPGA processing chips and moving ADC to mezzanine PCB with ADC for greater flexibility. This will provide a wide range of digitization options for application-specific modifications. There are four ADC daughter cards per Pixie module, each of which has eight channels of 14-bit, 250 MHz

digitizers. Another major change is the front input interface, where each ADC card has a single input of 8-position coaxial cable, as shown in Figure 3.12.

3.9 NEXT array

3.9.1 Prototyping Stage (Phase-I)

In the prototyping stage (Phase-1) of the NEXT development, a detailed test of the different components to build the detector module was performed along with the GEANT4 simulations [38]. Based on these tests and simulations, NEXT modules were designed, constructed, and tested in β decay and reaction experiments.

At the end of this phase, twelve detector modules were constructed. After characterizing each of them, an array of ten NEXT modules was assembled for the experiment at Argonne National Laboratory (ANL), as shown in Figure 3.13. The modules differ in the type of plastic scintillator (EJ276 or EJ200), segmentation (4×8 or 5×10), reflector layer (single or double ESR layer), polished or unpolished scintillator bars, and either adhesive material between the segments or just the air gap. Polishing the scintillator bars increases the light yield and thus results in better detection efficiency. Also, the double reflector layer (ESR) between the segments results in better isolation and improves the position resolution, as shown in Figure 3.14c–3.14f. The NEXT modules are continuously optimized for better performance (better timing and position resolution, low detection threshold, and higher efficiency). All the experiments discussed in this dissertation were performed with the modules constructed in this phase.

3.9.2 Phase-II

At the end of this phase, a full array of about 50 detector units will be constructed. The detector units will be constructed from EJ-299-33M plastic scintillator as recommended by the supplier (Eljen Technologies). This plastic has a higher light output and similar n- γ discrimination compared to the EJ-276. Each module will have 4×8 segments optically separated by double layers of ESR and air gap between them. About 15 new modules are

already constructed and are stored in a chamber filled with Nitrogen gas, as shown in Figure 3.15, to avoid the degradation of the plastic scintillator while exposed to open air.

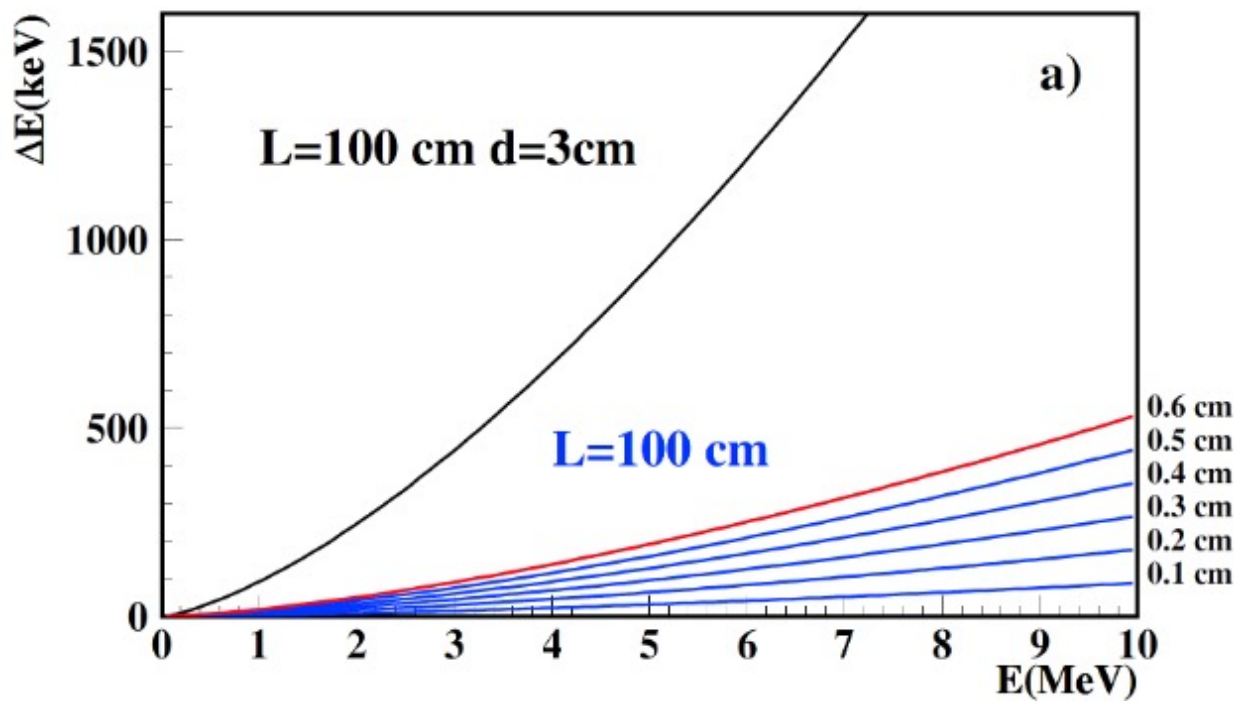


Figure 3.1: Energy resolution as a function of neutron energy for different segment thicknesses calculated using Equation 3.1.

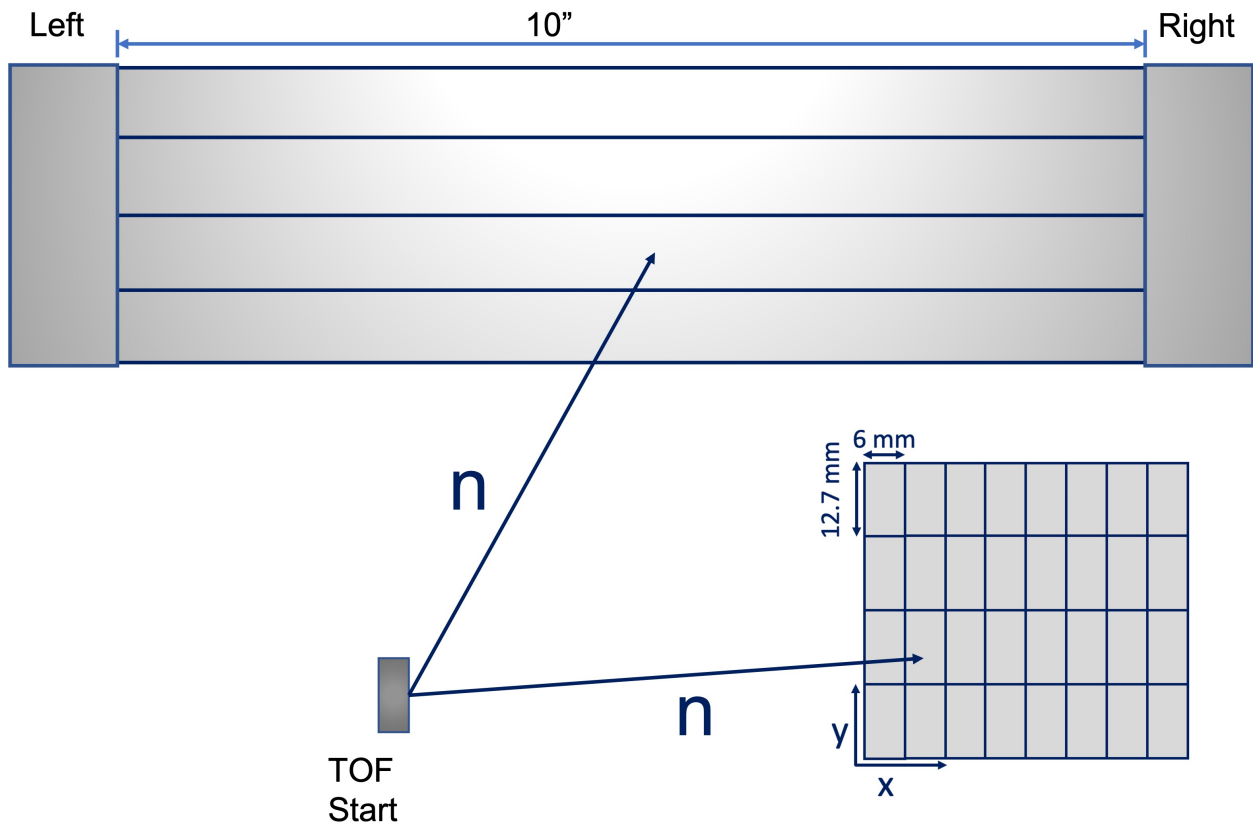


Figure 3.2: Schematic drawing of NEXT in the TOF setup. A single detector unit with the photosensors coupled on either side (top). The detector is facing the neutron's flight path direction. Side view of the detector showing the possible segmentation, higher segmentation along the neutron flight path direction (bottom).

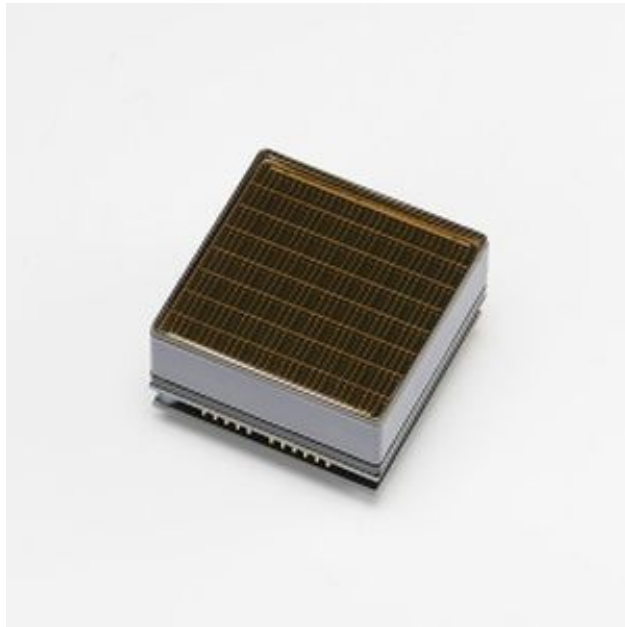
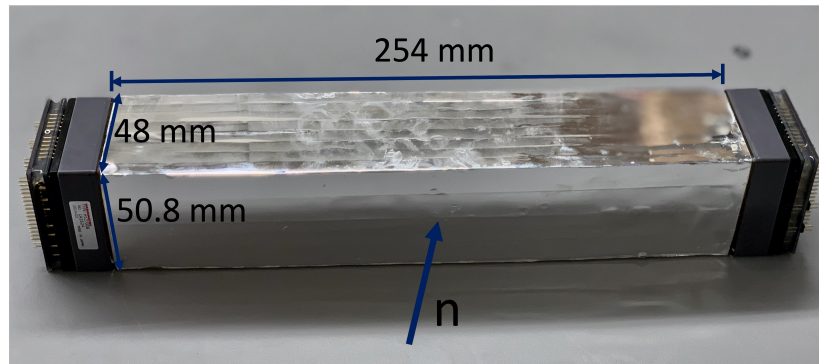
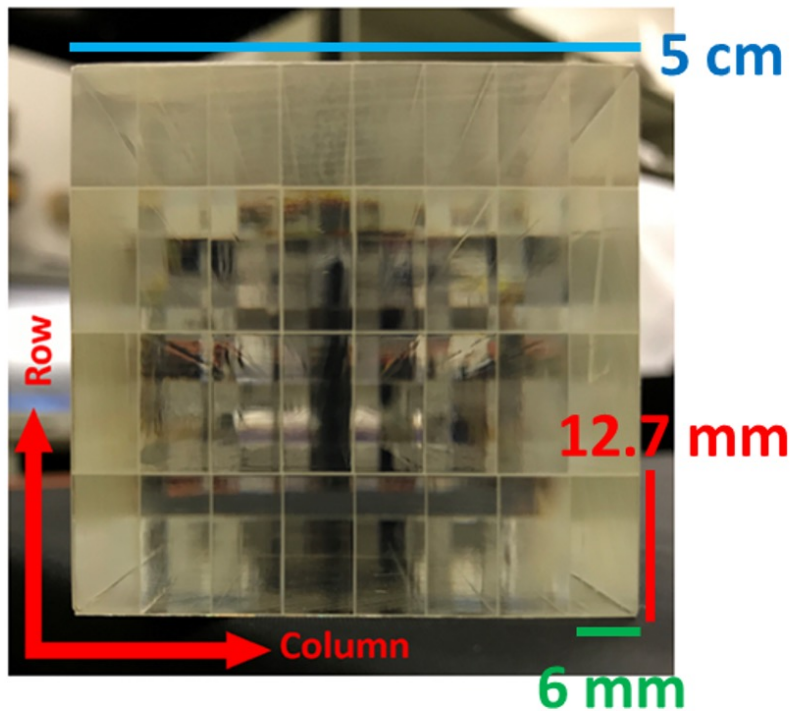


Figure 3.3: Multianode PMT (MAPMT) model H12700B developed and manufactured by Hamamatsu Corporation [41].



(a)



(b)

Figure 3.4: (a) A typical NEXT Module. The segmented plastic scintillator is coupled to the Hamamatsu H12700 position-sensitive PMTs on either side for the light readout. (b) Cross-section view of the detector. Higher segmentation is along the direction of the neutron flight path (along the x-axis). The segments along the x-axis are referred to as the detector layers/columns, and segments along the y-axis are referred to as rows. There are eight detector layers/columns and four rows in a fully assembled detector module.



Figure 3.5: Pixie-16 16 channel digitizer from XIA LLC [43].

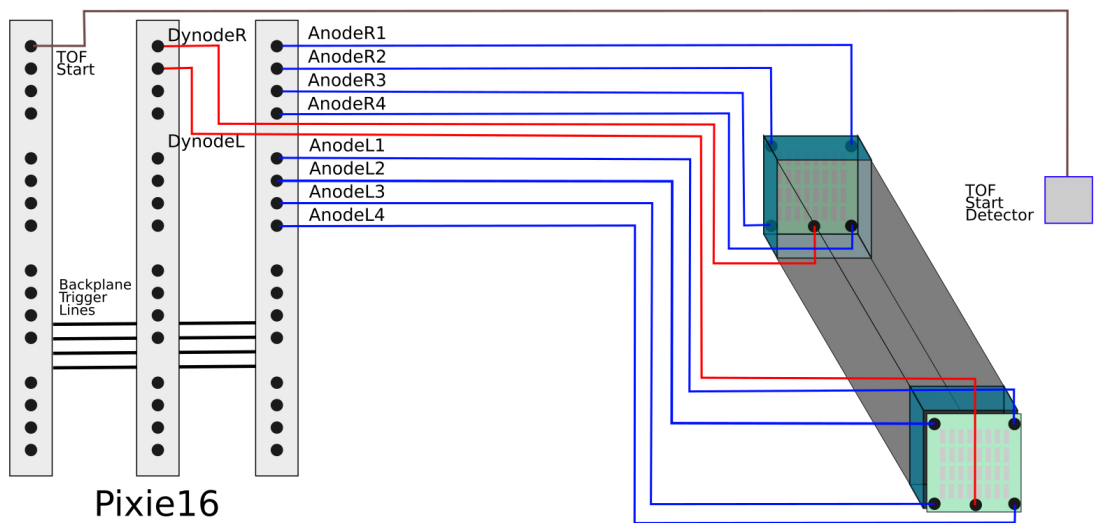


Figure 3.6: A schematic representation of the NEXT readout in TOF setup with start detector. The five signals from each side of the NEXT (dynode: red, anodes: blue) and a signal from the TOF start detectors are digitized using Pixie-16 digitizers. The TOF start detector provides a reference signal for the time-of-flight measurement. These signals communicate using backplane trigger lines to generate the coincident trigger configurations.

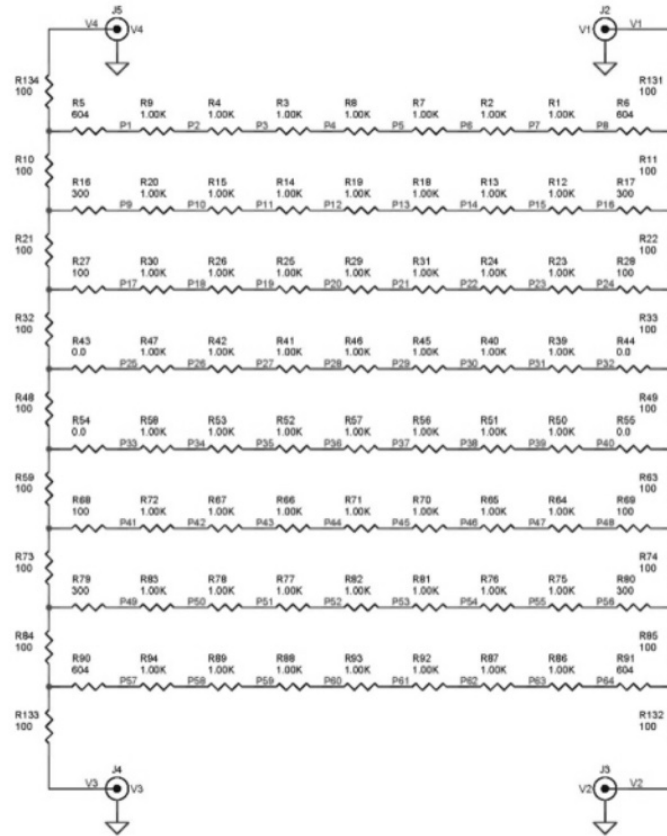


Figure 3.7: Anger logic resistive circuit by Vertilon Corporation [42].

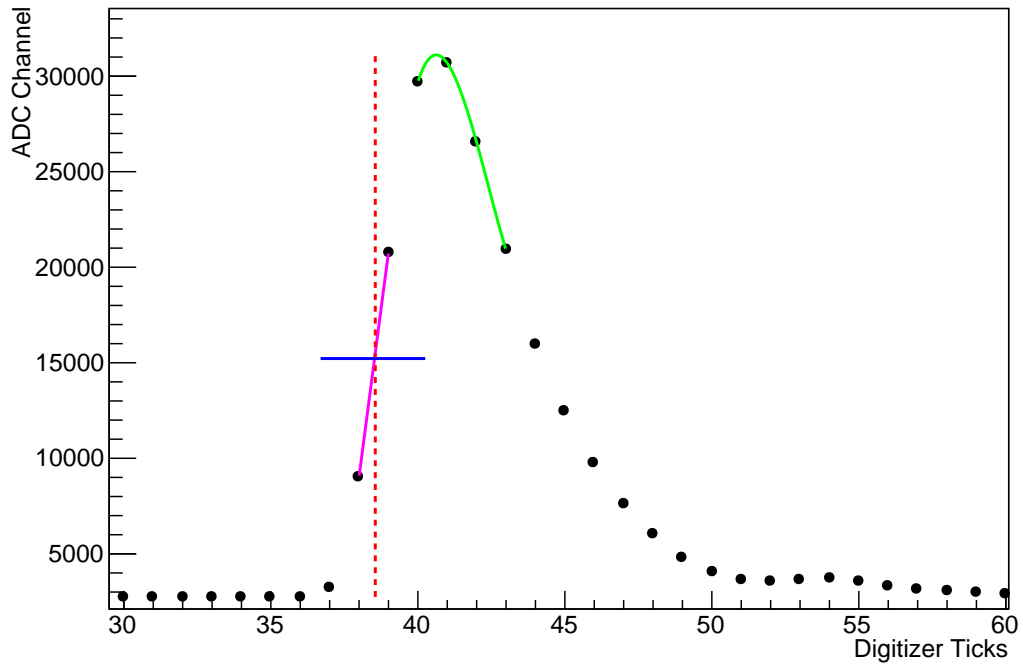


Figure 3.8: A typical digitized trace with the polyCFD algorithm for the CFD threshold of 45%. The third-order polynomial fit to find the peak maximum is shown in green, while the linear interpolation between the points around the CFD threshold is shown in magenta. The crossing point between the magenta and green line (CFD threshold), represented by the dashed red line, determines the high-resolution timing.

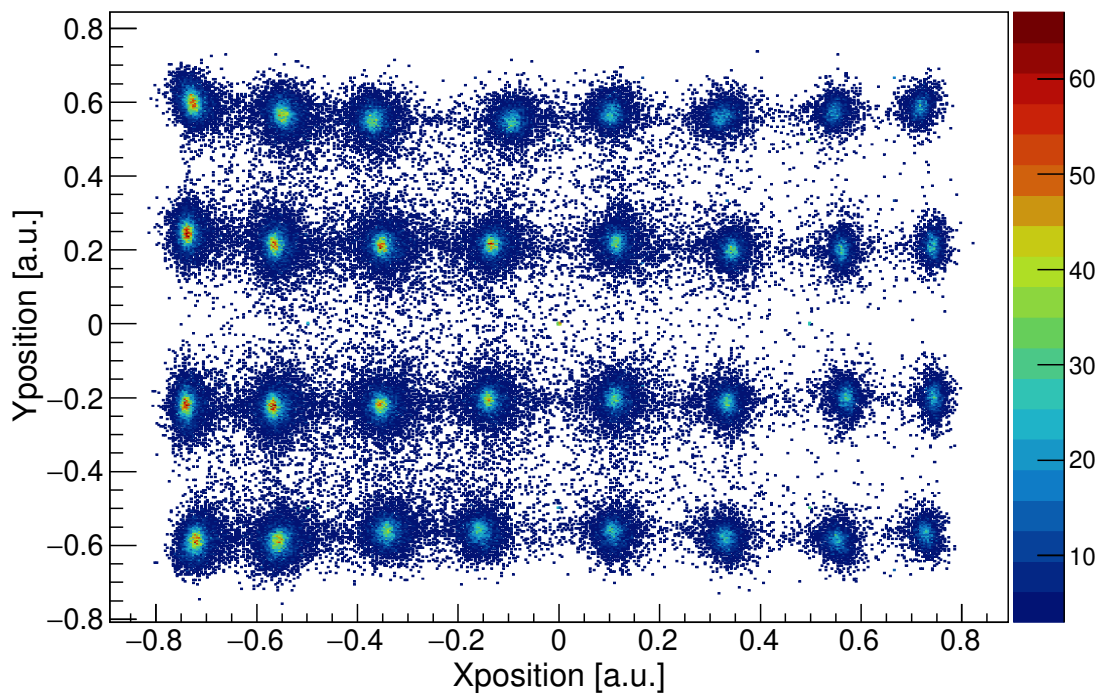
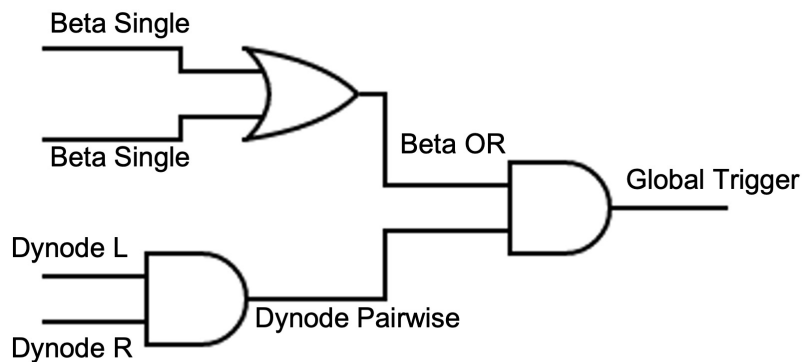
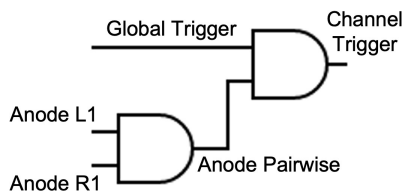


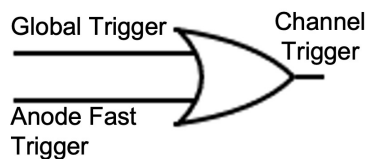
Figure 3.9: The neutron interaction position in the detector extracted using Equations 3.3a and 3.3b.



(a)



(b)



(c)

Figure 3.10: The schematic representation of the coincidence trigger schemes. (a) Generating the global validation trigger using start detectors (beta singles) and NEXT dynodes. (b) A triple coincidence trigger scheme, where anodes are always required to be in coincidence with dynodes from the same detector. (c) A new trigger configuration based on unconditional readout of the anode signals. This trigger scheme allows the forced recording of a signal if a global trigger is generated.

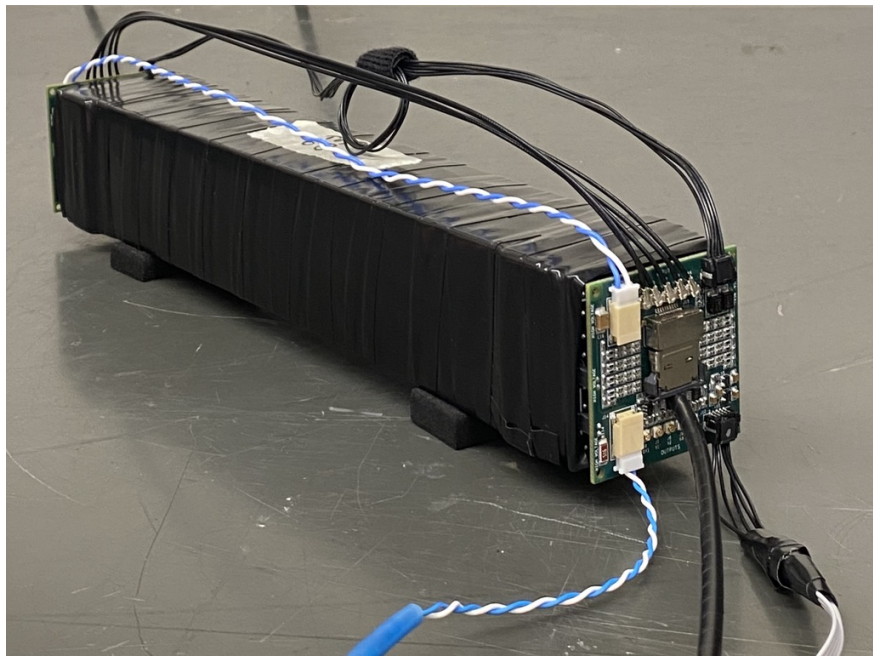
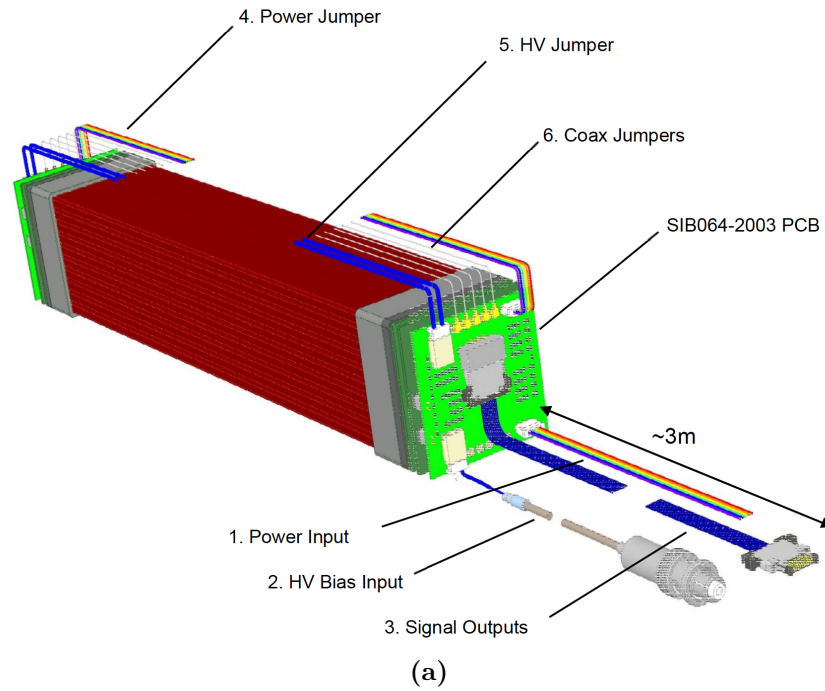


Figure 3.11: Schematic view of new signal readout assembly developed by Vertilon Corporation top). Actual boards coupled to a 10 inches long module (bottom).

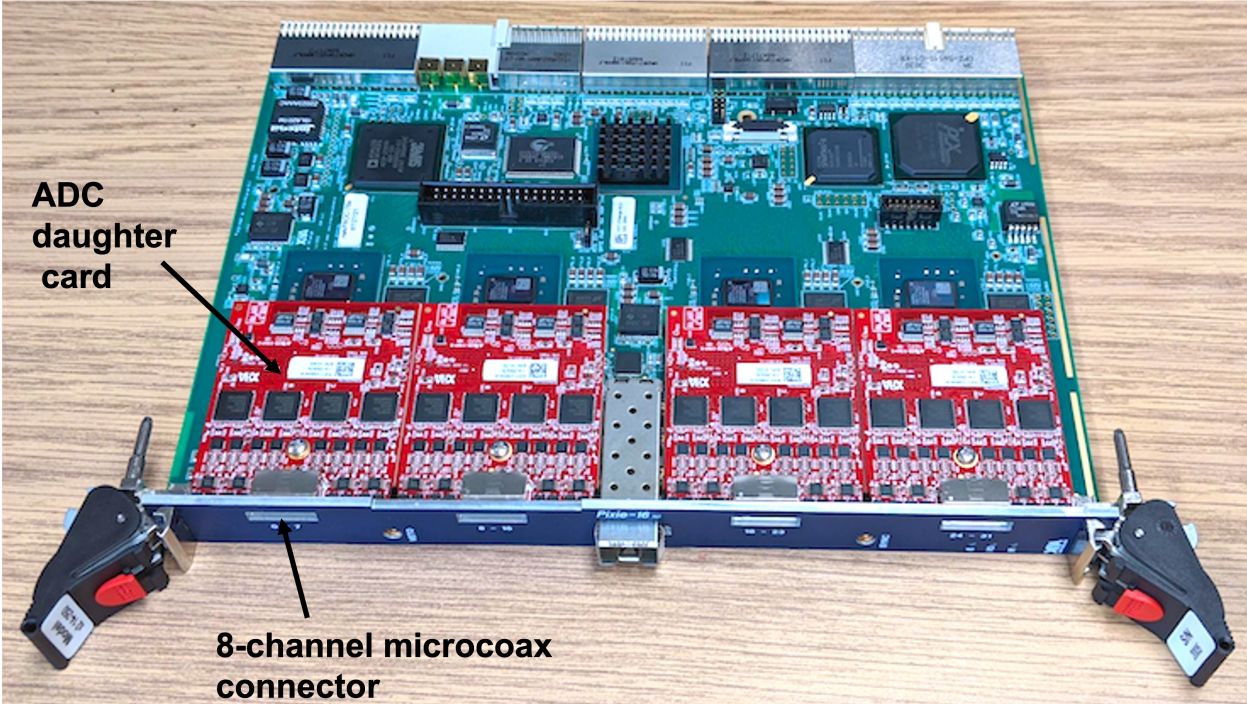


Figure 3.12: New Pixie digitizer (Pixie-16x2).



Figure 3.13: An array of 10 NEXT modules assembled for the experiment at Argonne National Laboratory.

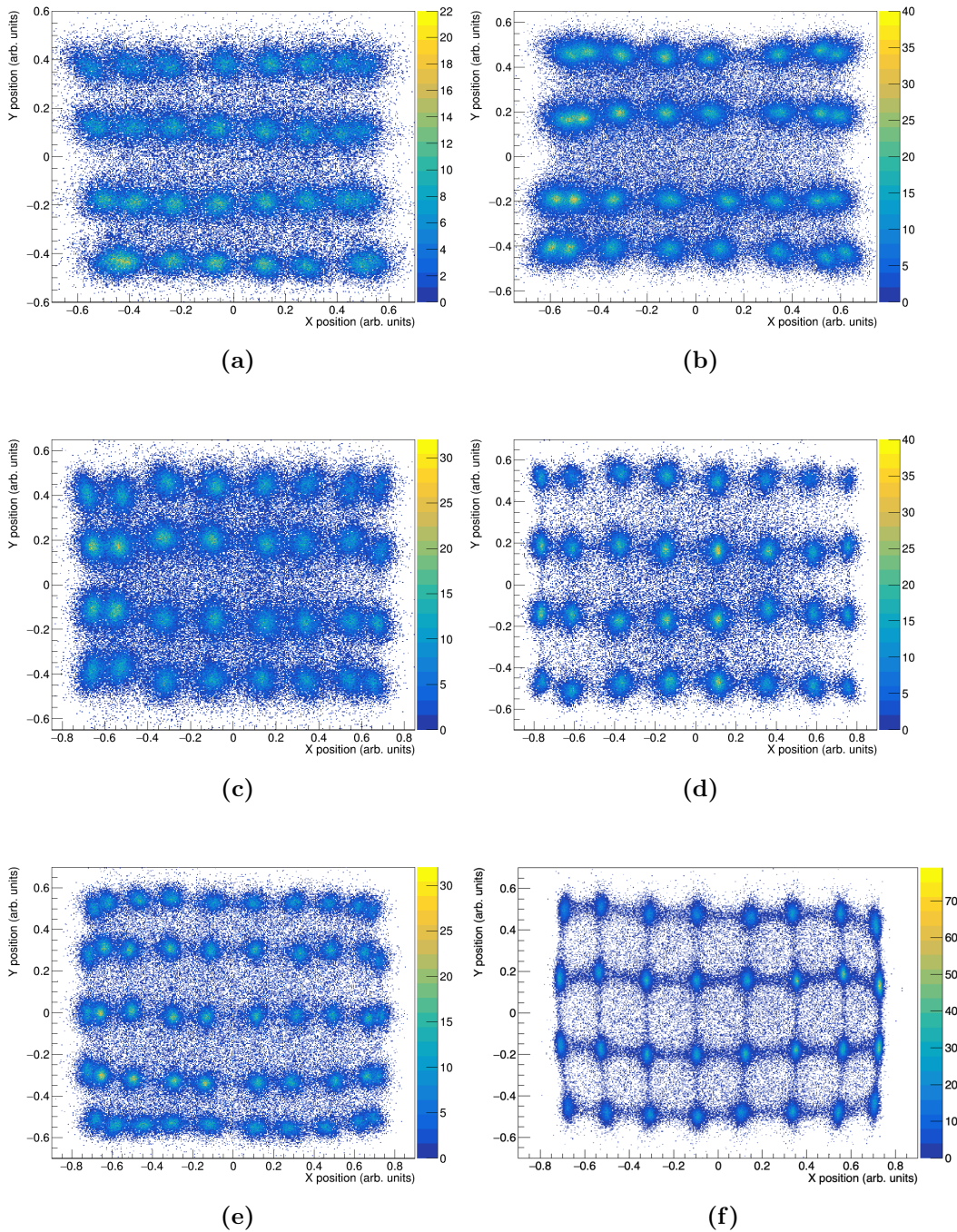


Figure 3.14: The scintillation position inside the different NEXT modules reconstructed using the Anger logic algorithm.

- (a) EJ276, single layer ESR, polished sides, and adhesive material between the segments.
- (b) EJ200, single layer ESR, polished sides, and adhesive material between the segments.
- (c) EJ276, double layer ESR, polished sides, and adhesive material between the segments.
- (d) EJ276, double layer ESR, unpolished sides, and adhesive material between the segments.
- (e) EJ276, 5X10 segmentation, double layer ESR, polished sides, and air gap between the segments.
- (f) EJ276, double layer ESR, polished sides, and air gap between the segments.

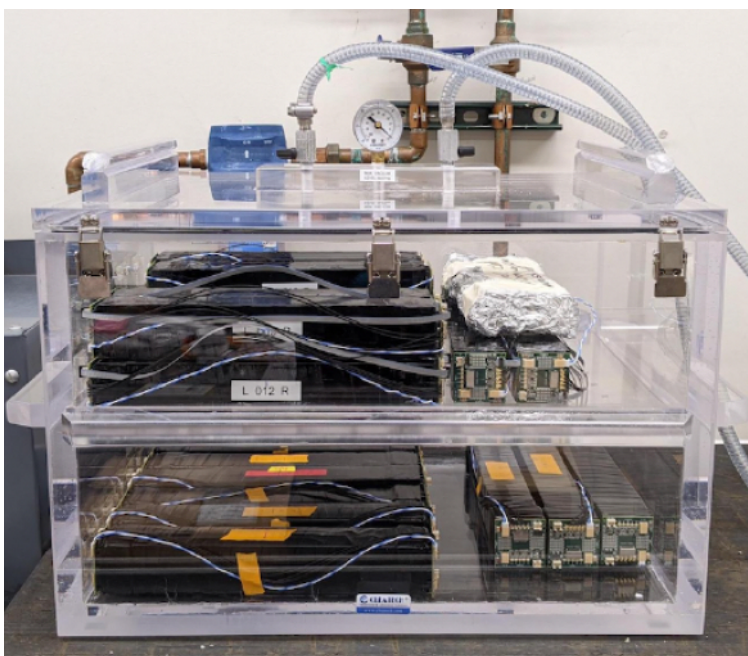


Figure 3.15: NEXT modules stored in a chamber filled with Nitrogen gas to avoid the scintillator degradation.

Chapter 4

Efficiency Measurement

4.1 $^{27}\text{Al}(\text{d},\text{n})$ Measurement

The neutron detection efficiency measurement of different NEXT modules was performed at the Ohio University's Edwards Accelerator Laboratory (EAL), which provides a wide range of neutron energies using $^{27}\text{Al}(\text{d},\text{n})$ reactions [48]. The 7.44 MeV deuteron beam impinges on an ^{27}Al target, producing neutron energy spectra at different angles relative to the beam direction. The neutron energy spectrum shown in Figure 4.1 is well described at 120° relative to the beam direction and can be used as a standard spectrum to measure the efficiency of the neutron detectors.

The measurement was performed with five NEXT modules, four of which were constructed from EJ-276 and one from EJ-200 plastic scintillator. Four of the modules were 10 in long, and one of them was 5 in long. Three typical modules, EJ276-10, EJ200-10, and EJ276-05, were considered for the analysis.

Each NEXT module was placed at a distance of 5 m from the target assembly inside the 30 m long concrete tunnel, as shown in Figure 4.2. The distance was chosen such that the NEXT module was fully illuminated, and the neutron rate would be sufficient to make reliable measurements. A chopped pickoff signal from the beam buncher was used as a reference signal for the neutron time-of-flight measurement. Figure 4.3 shows a typical TOF spectrum measured by the EJ276-10 module in the beam, and the module moved out of the beam. The flat nature of the out-of-beam TOF spectrum indicates the absence of scattered

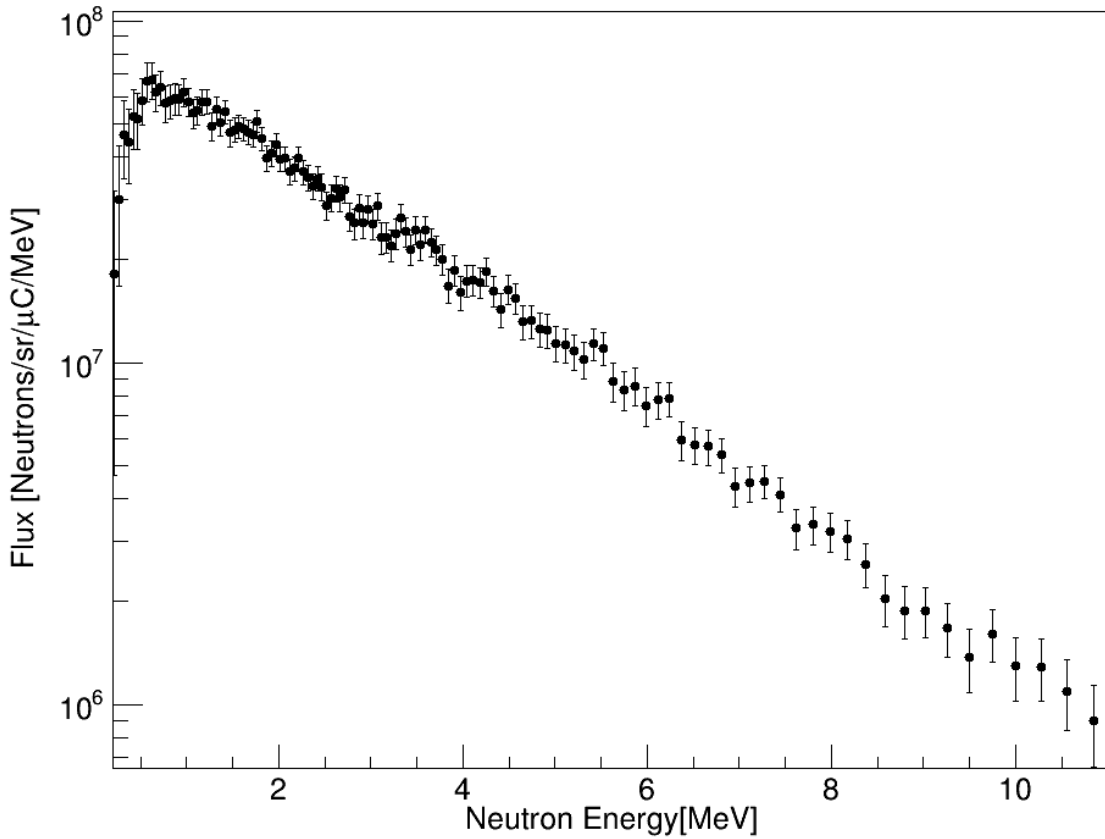


Figure 4.1: A reference neutron spectrum with known neutron flux for $^{27}\text{Al}(d,n)$ at 120° measured at the Edwards Accelerator Laboratory (EAL) at Ohio University [48].

neutrons inside the tunnel. The background is mainly composed of prompt and scattered γ rays, which can be easily subtracted to obtain the actual neutron time-of-flight spectrum.

For intrinsic efficiency, the neutron flux (neutrons/sr/ μ C/MeV) was measured for each NEXT module and compared with the reference neutron spectrum provided by the facility. Figure 4.4 shows the intrinsic efficiency of three NEXT modules measured at EAL using the $^{27}\text{Al}(\text{d},\text{n})$ reactions at 120° . The higher light output of the EJ-200 scintillator led to the better performance of the EJ200-10 module for low-energy neutrons compared to the other two modules.

4.2 Simulations: *NEXTsim*

NEXTsim [49], a GEANT4 [50, 51] based simulation framework developed to characterize the NEXT module, was used to simulate neutron detection efficiency for the various NEXT modules.

In *NEXTsim*, the same experimental setup as the one used at EAL was rendered, and the same neutron flux spectrum provided by the facility was used as a source. Comparative studies have been performed between measured and simulated intrinsic efficiency for each NEXT module.

Figure 4.5 shows the intrinsic efficiency calculated using *NEXTsim* compared to the measured efficiency for the three NEXT modules EJ200-10, EJ276-05, and EJ276-10. The EJ200-10 and EJ276-05 modules showed good agreement between measured and simulated efficiencies within the uncertainties; however, the measured intrinsic efficiency is lower than the simulated efficiency for the module EJ276-10 for energies below 1.5 MeV. The discrepancy is attributed to a low light yield of the EJ-276 scintillator, the limitation of the Anger Logic readout, and the trigger schemes used.

The trigger scheme used in the efficiency measurement at EAL was the triple coincidence trigger and shown schematically in Figures 3.10a and 3.10b. In this scheme, left-right anodes also contribute to generating the coincidence triggering. If any of the anode signals are weak to generate the trigger because of the Anger logic and the charge division, the event is lost. This is usually the case when the interaction occurs at the edge of the NEXT module,

which results in a pseudo-threshold that effectively raises the detection threshold in the front and back layers of the NEXT module in the EAL measurement, as seen in Figure 4.6a. This causes the discrepancy in low-energy neutron detection. To improve the low-energy neutron detection, a new trigger scheme based on unconditional readout was implemented in the measurement. The schematic of this trigger scheme is shown in Figure 3.10c. In this scheme, anodes do not contribute to generating triggers and are set to unconditional readout mode so that they are recorded whenever there is a coincidence trigger between TOF start and left-right dynode signals. The immediate improvement in the detection of the low-energy events can be seen in Figure 4.6b. Next section details the measurement performed with a new trigger scheme to recover low-energy neutron detection for the EJ279-10 module.

4.3 ^{252}Cf measurement with new trigger scheme

A measurement of the ^{252}Cf fission neutron spectrum was performed to show the improvement in the low-energy neutron detection using a new trigger scheme compared to the trigger scheme used during efficiency measurement at EAL.

The measurement was performed using the old triple coincidence trigger and the new external fast trigger configurations in the same experimental setup. The same NEXT module (EJ276-10) from the EAL measurement was used and placed at a distance of 94.4 cm from the source. The start signal for the TOF measurement was provided by detecting prompt γ -rays from fission in a $25.4 \times 25.4 \times 12.7$ mm³ plastic scintillator (EJ-200) placed close to the source and the NEXT module provided the stop signal. A shadow bar measurement was also performed in a similar setup to see the background neutrons scattered off the floor, walls, and the surrounding materials. The blocks of polyethylene cubes inserted between the source and the NEXT module blocked direct neutrons from the source. After subtracting the background, a clean time-of-flight spectrum was obtained, and corresponding neutron energies were extracted.

Figure 4.7a shows the ratio of the number of neutrons detected per energy bin in the new and old trigger configurations. With the new trigger configuration, the detection efficiency for the low-energy neutrons (below 1.5 MeV) is higher than the old one. This removed

the discrepancy seen in Figure 4.5c between the measured and simulated efficiency for the EJ276-10 module, as shown in Figure 4.7b. The efficiency measured at EAL was multiplied by the ratio of the neutron detected in the new and old trigger schemes to get the corrected efficiency.



Figure 4.2: The experimental setup at EAL. The NEXT modules were placed at a distance of 5 m from the target assembly inside the 30 m long neutron time-of-flight tunnel. The neutron beam was collimated using concentric polyethylene collimators.

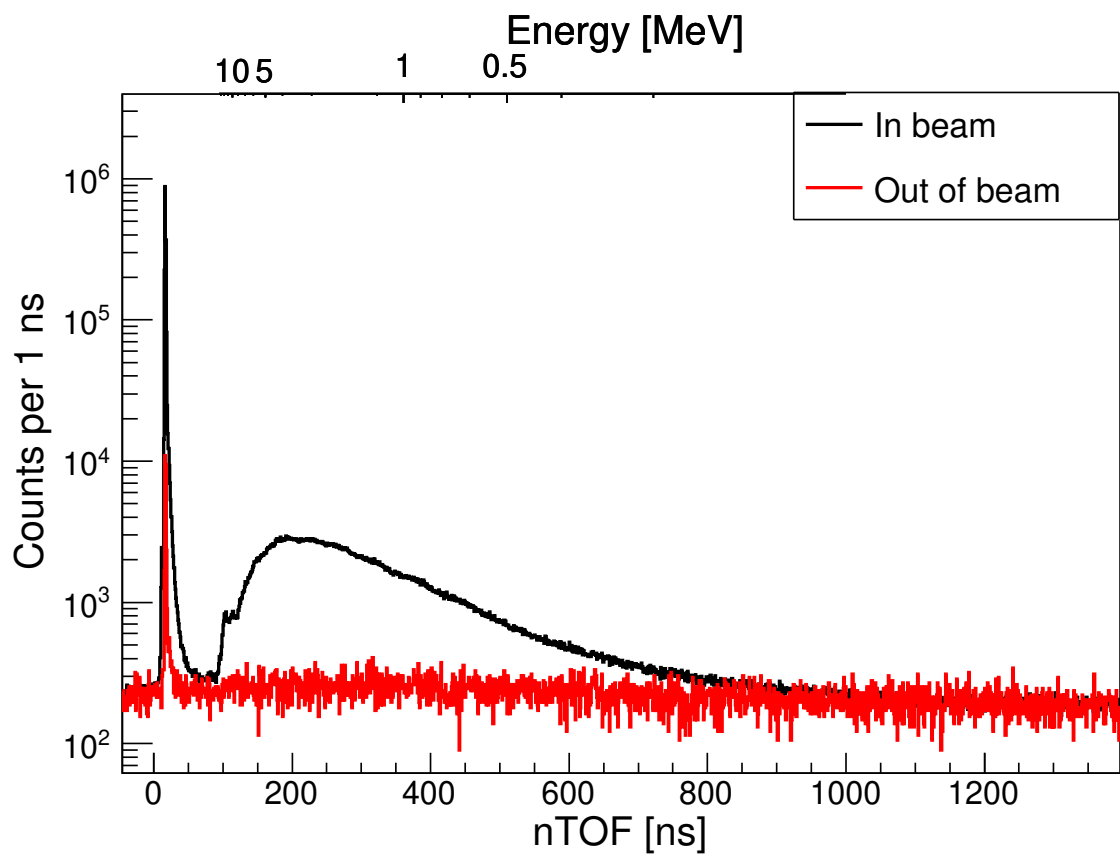


Figure 4.3: The time-of-flight spectra measured by EJ276-10 module with $^{27}\text{Al}(d,n)$ at 120° with a module in beam (black), the module moved out of the beam (red).

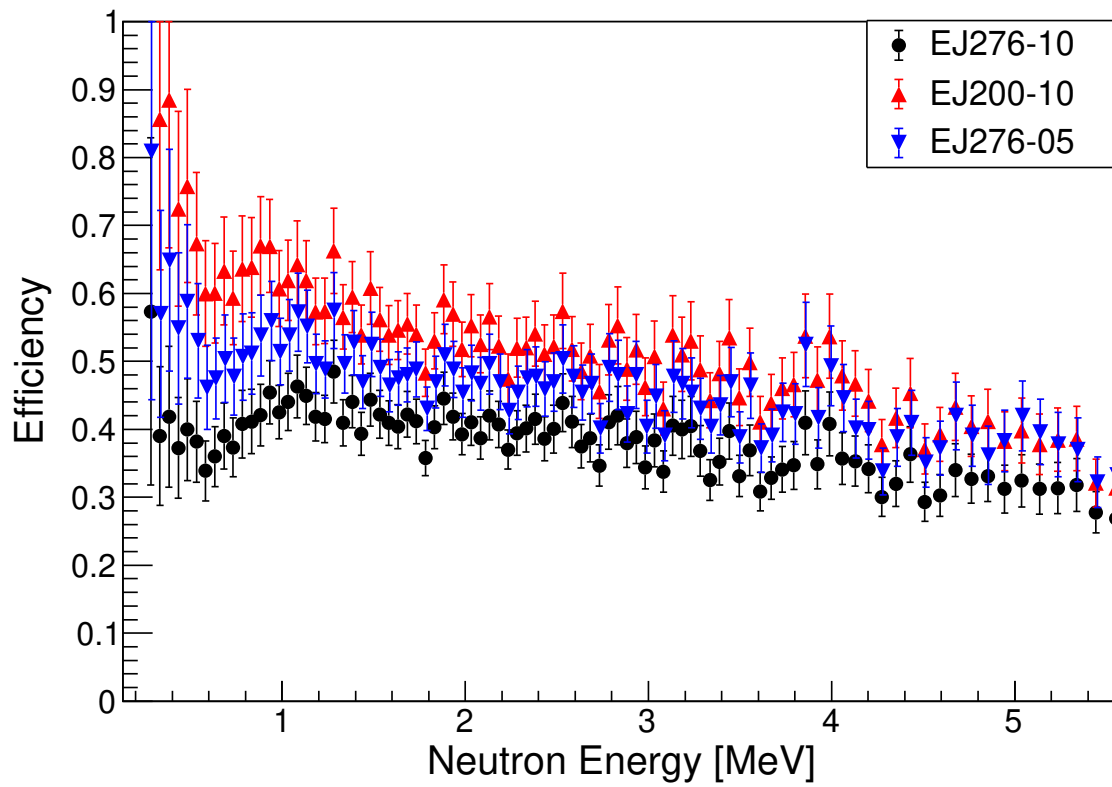
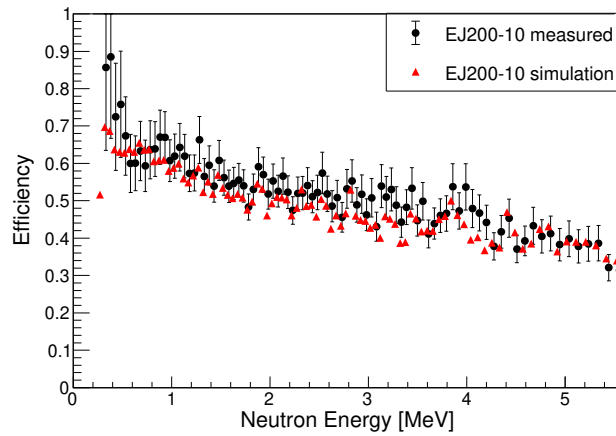
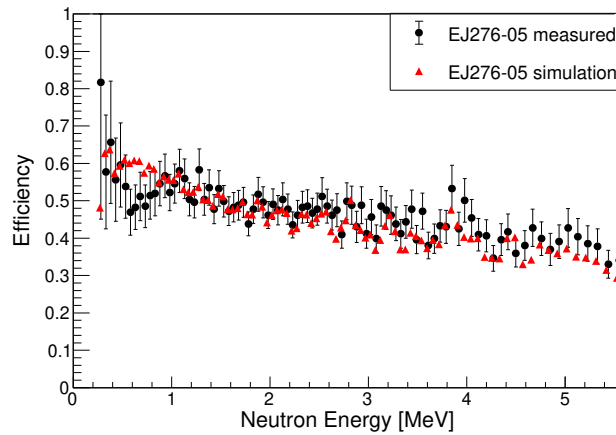


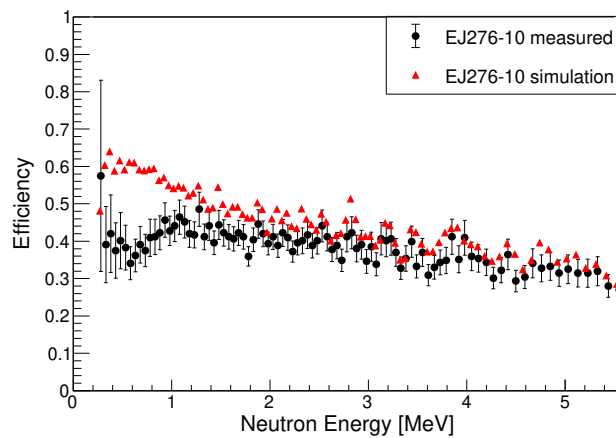
Figure 4.4: The efficiency for EJ276-10 (black), EJ276-05 (blue) and EJ200-10 (red) modules obtained from $^{27}\text{Al}(d,n)$ reactions at 120° with a 20 keVee threshold.



(a)

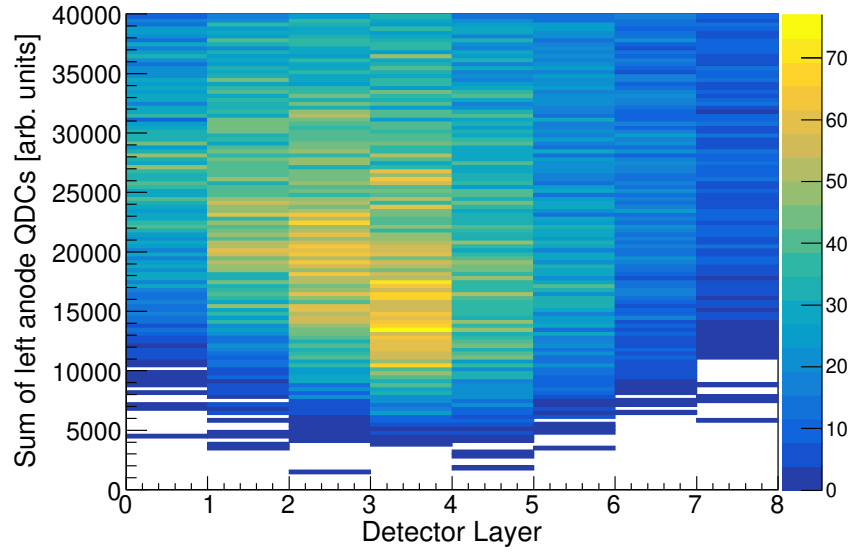


(b)

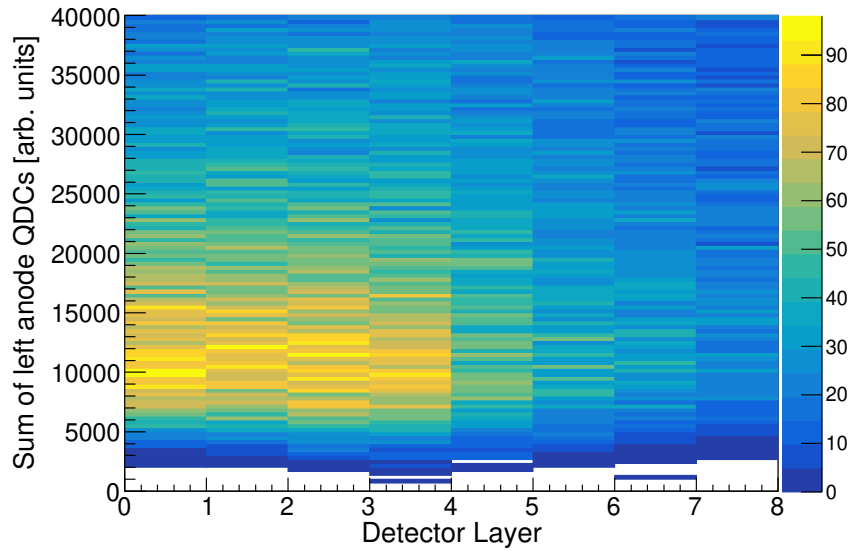


(c)

Figure 4.5: The measured intrinsic efficiency using $^{27}\text{Al}(d,n)$ reactions at 120° at EAL with 20 keVee threshold (black) compared to the NEXTSim calculation (red) for EJ200-10 (a) EJ276-05 (b) and EJ276-10 (c) modules.

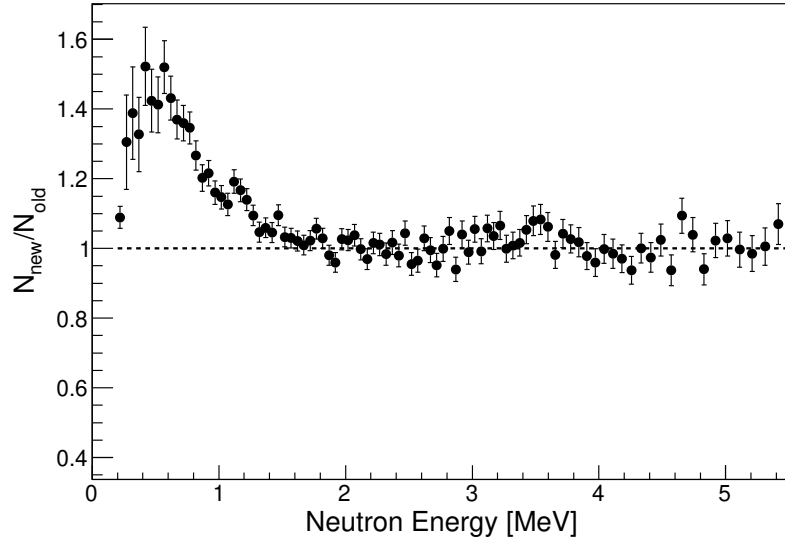


(a)

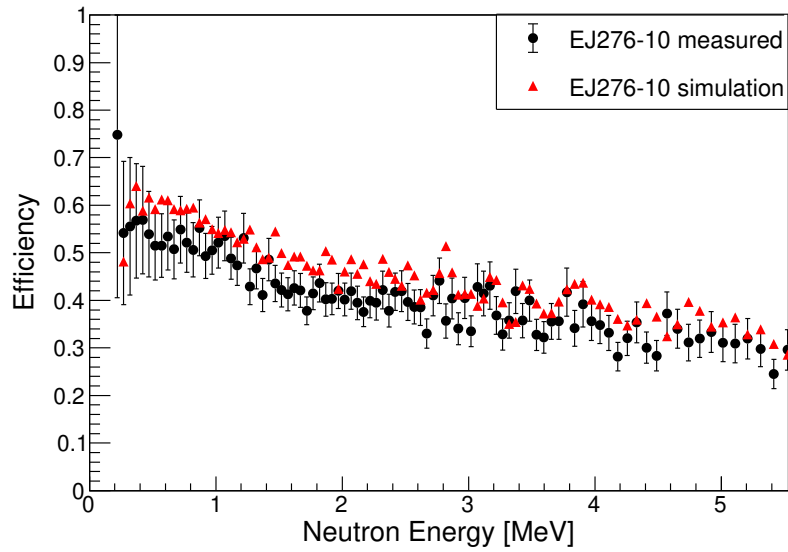


(b)

Figure 4.6: Two-dimensional histograms showing the sum of the left anode QDCs (integral of the pulse within a given time interval) plotted against the corresponding detector layer for events taken with the triple coincidence trigger (a) and the new external trigger configuration (b). The zeroth layer indicates the layer closest to the source. The higher QDC threshold in the front (towards the source) and back (away from the source) layers seen in the top plot does not exist in data taken with the new trigger mode. The detection threshold is consistent between the layers, as shown in the bottom plot.



(a)



(b)

Figure 4.7: (a) Ratio of number of neutrons measured per energy bin in new and old trigger schemes with the EJ276-10 module using ^{252}Cf source. (b) The efficiency of the EJ276-10 module measured at EAL was corrected using the ratio of neutrons detected in the new and old trigger schemes shown in Figure 4.7a.

Chapter 5

Position-Timing Correlation and Correction

Neutron time-of-flight detectors are often comprised of thick bars of the scintillator to achieve high detection efficiency. In the neutron time-of-flight experiments, the uncertainty in the flight path length measurement is due to the uncertainty in the neutron interaction position determination, which is basically the thickness of the detector. In other words, the neutron flight path depends on the interaction position as it traverses through the detector. Because of the segmentation, NEXT has the capability of localizing neutron interaction positions which enables a precise determination of flight path length. This chapter demonstrates the correlation between neutron time-of-flight and the interaction position and the time-of-flight corrections using interaction position.

5.1 TOF Corrections

In our data analysis procedure, the detector response function is derived based on the neutron TOF, which also incorporates the spectrum's features due to scattering from the surrounding materials. The TOF spectrum is then deconvolved into neutron energies using the response function. This is a conventional procedure and relies on the fact that the neutron response function can be easier to characterize using TOF through measurements and simulations.

The chosen procedure for the TOF correction in the following text is a consequence of this choice.

The neutron TOF spectrum should reflect measurements at a specific path length for precise energy determination. For this, the TOF must be corrected for the flight path length as it depends on the neutron interaction position in the detector volume. To correct, the TOF is extracted for the original flight path and scaled to the fixed flight path for each event by,

$$t_0 = t \times \frac{L_0}{L}, \quad (5.1)$$

where L_0 is the fixed flight path and L is the original flight path. If the TOF is scaled to the fixed flight path for each detector, the TOF for all detectors can be combined into a single spectrum and converted to an energy spectrum using a deconvolution procedure.

For a typical neutron TOF detector, the flight path length correction can be made only in one dimension, along the bar, which limits the detector's energy resolution. The distance along the detector axis is typically determined using time difference or light sharing between PMTs at opposite ends of the scintillator.

NEXT can localize the neutron interaction position in three dimensions in the detector, as shown schematically in Figure 5.1. This allows the scattering position to be corrected with greater precision, resulting in better energy resolution. The internal scattering position can be written into parallel and perpendicular components relative to a fixed flight path length. For NEXT, using the notations in Figure 5.1, L is then defined as $L = \sqrt{(L_0 + l_x)^2 + l_y^2 + l_z^2}$.

An example of the 2D reconstructed neutron scattering position (X and Y positions) in a NEXT module obtained utilizing four anode signals and the Anger logic algorithm [46], as described in the Section 3.5, is shown in Figure 5.2. The pixels in Figure 5.2 are correspond to the module segmentation. In the TOF correction process, pixels are defined by their physical size and position; the image in Figure 5.2 is used to identify which pixel the neutron interacted with. A group of pixels at the same X-position is referred to as a “column/layer,” and the one at the same Y-position is referred to as a “row”. The actual flight path length and corresponding TOF are determined exclusively for each pixel using this reconstructed

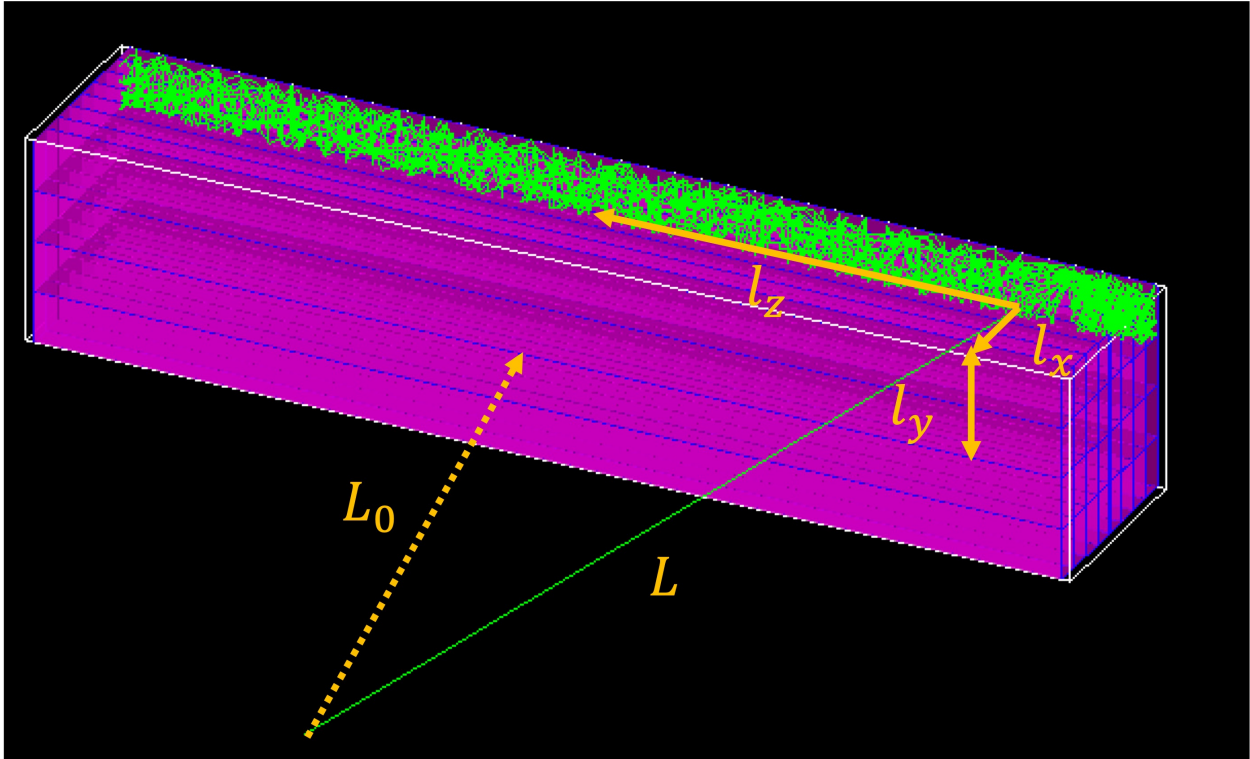


Figure 5.1: The schematic demonstration of TOF correction procedure using the neutron interaction position inside the detector. Based on interaction position, the original flight path length (L) can be resolved into x, y, and z components with respect to a fixed flight path length (L_0). The TOF is corrected for the flight path by scaling the actual TOF measurement by the ratio of L_0 and L .

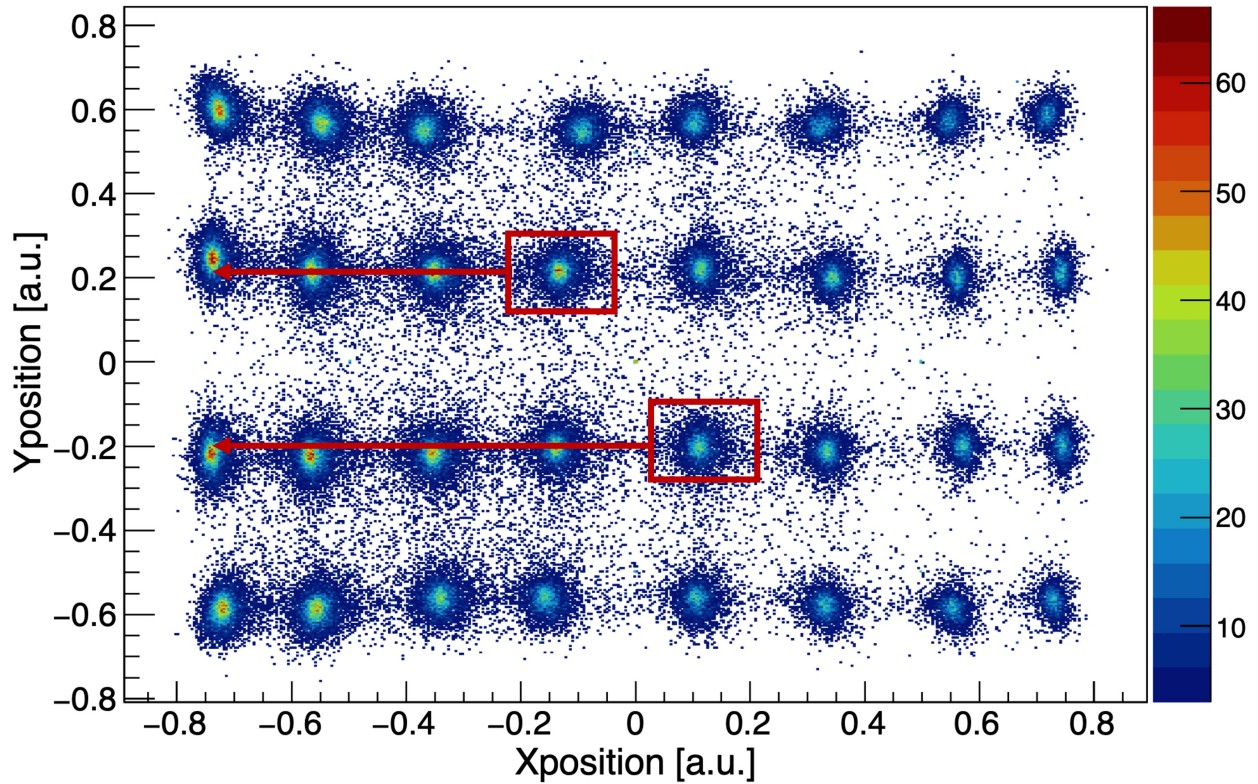


Figure 5.2: The reconstructed neutron interaction position in a NEXT module. The X and Y positions are the same as shown in Figure 5.1. The pixels represent the module segmentation. The original TOF is obtained exclusively for each pixel and scaled to the middle of the first layer using Equation 5.1 as indicated by the red lines. See the text for the detail.

position. The TOF is then scaled to the fixed flight path length, which is the middle of the first detector layer, using Equation 5.1, as shown graphically in Figure 5.2 by red lines.

The following sections detail the TOF corrections using interaction position in the neutron TOF measurements. The term “uncorrected” refers to the TOF correction for the flight path is not implemented (treating as a typical non-segmented neutron detector), whereas “corrected” refers to the TOF correction implemented.

5.2 ^{17}N β -delayed neutron emission

The β decay of ^{17}N is well known for its subsequent neutron emission at energies of 383 keV, 1171 keV and 1700 keV, see Figure 5.3 [52, 53], which are suitable to characterize the NEXT array. The measurement was performed at National Superconducting Cyclotron Laboratory (NSCL) with an array of ten NEXT modules: one EJ200-10, one EJ200-20, and the rest EJ276-10. NEXT modules were arranged in a circular arch with a flight path of ~ 50 cm from the ion implant position as shown in Figure 5.4. Ions were implanted on Yttrium Orthosilicate (YSO) based segmented detector of dimensions $50.8 \times 50.8 \times 12.7$ mm³ [54], which also provided a start signal for the neutron TOF measurement.

The neutron TOF spectrum measured at individual detector layers (8 layers) is shown in Figure 5.5a, where a shift in the TOF centroid is observed with respect to the layer position. Once the TOF is corrected for flight path length using Equation 5.1, the TOF centroids lined up as seen in Figure 5.5b. Figure 5.6 shows the summed TOF spectra for all the layers without correction (black) and after correction (red). The TOF correction resulted in better-resolved peaks.

Another way of looking into the position-dependent timing is plotting the TOF against the neutron scattering position along the flight path direction (X-position). A linear relationship is observed between the TOF and scattering position for all three neutron groups with a slope depending on the neutron energy, as seen in Figure 5.7a. This is translated into a poor separation between the TOF peaks, especially between the two high-energy peaks. After the correction, TOF becomes independent of the interaction position as shown in Figure 5.7b, resulting in better-separated peaks.

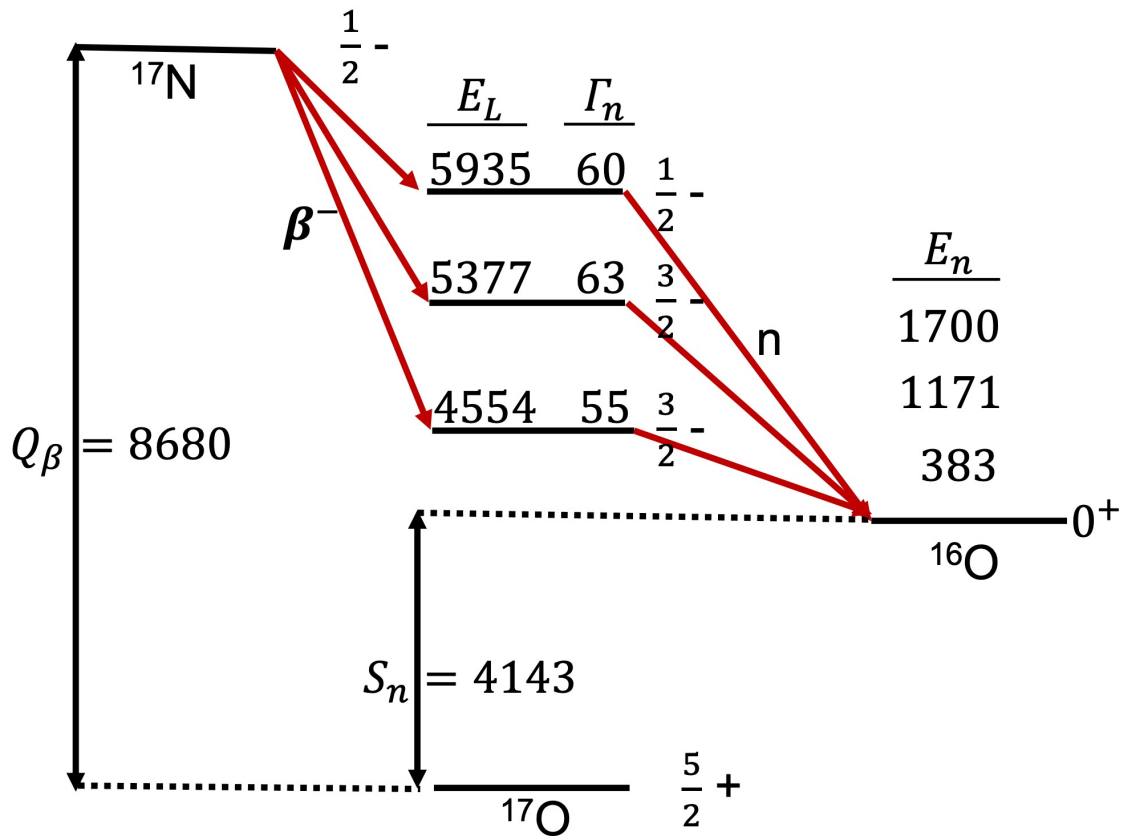


Figure 5.3: The decay scheme of ^{17}N . The β decay of ^{17}N populates the states above neutron separation energy in ^{17}O , which de-excite to the ground state of ^{16}O via neutron emission. All the energies are in keV.

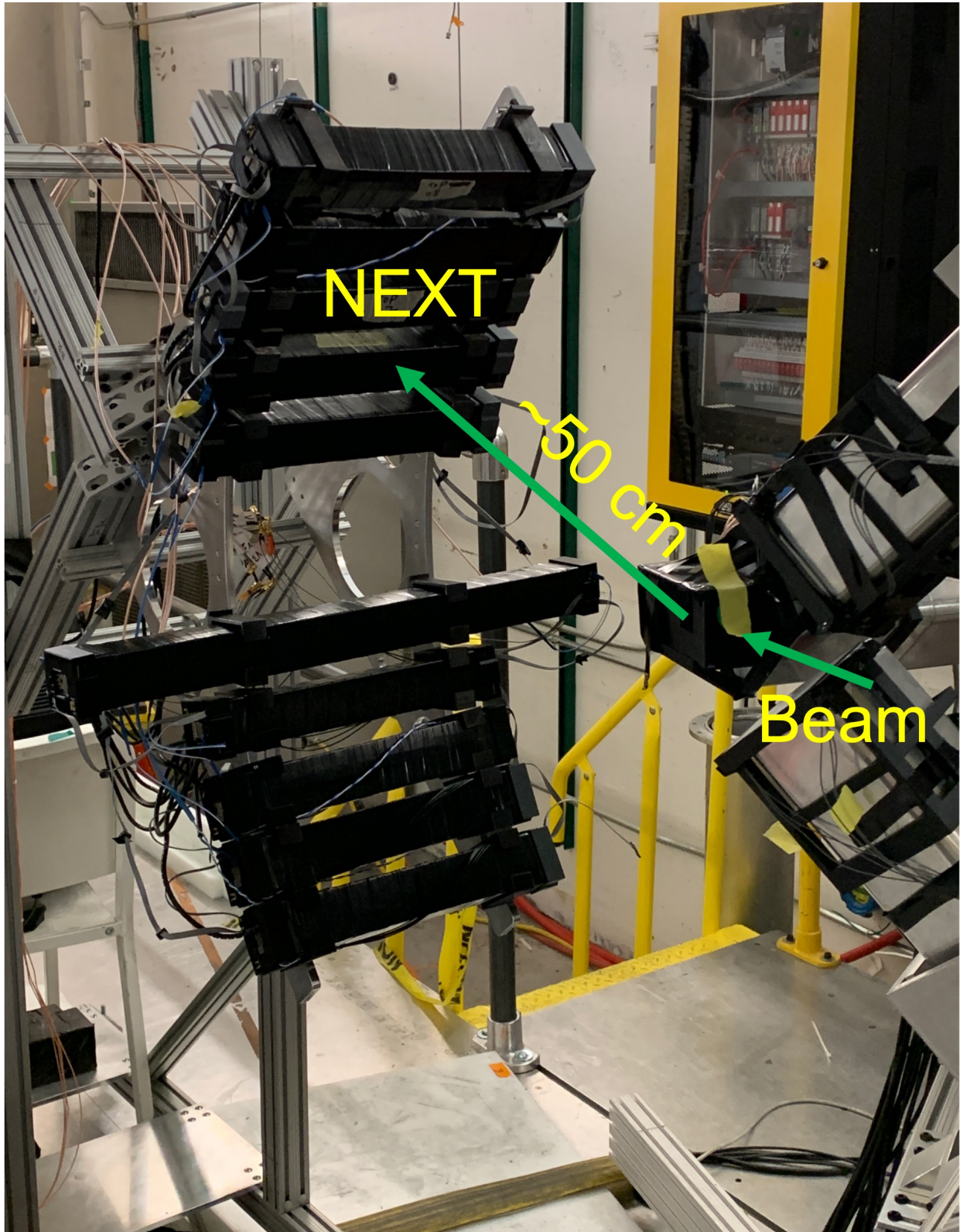
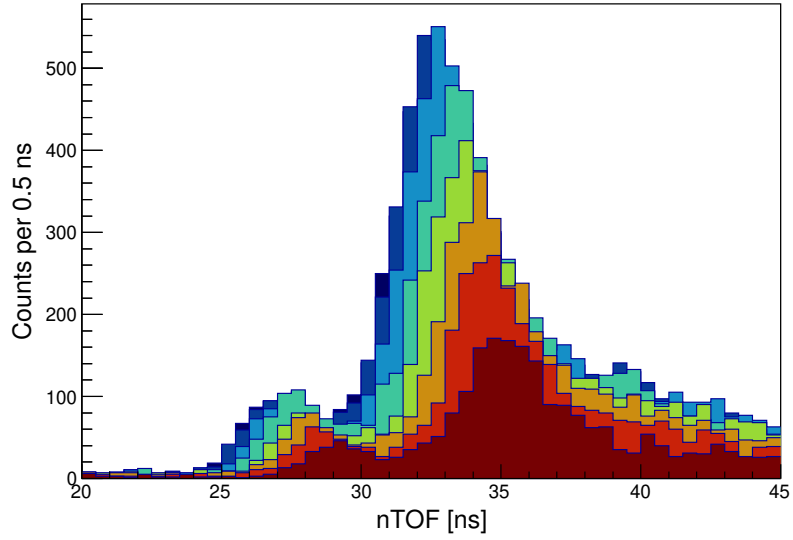
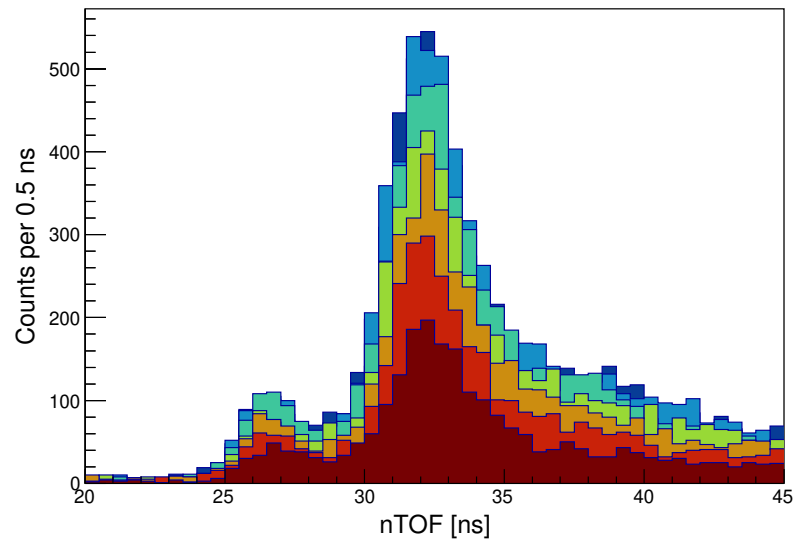


Figure 5.4: The experimental setup at NSCL. Ten NEXT modules were arranged around the ion implant position at a distance of ~ 50 cm.



(a)



(b)

Figure 5.5: The neutron TOF measured at the individual layers before the TOF correction (a) and after the TOF correction (b). The spectra are zoomed around two high-intensity peaks for clarity.

The neutron emitting states in ^{17}O have non-negligible level widths [52], which are greater than the energy resolution of our detector. This added additional broadening in the neutron TOF peaks on top of our detector’s resolution, ~ 700 ps from the implantation detector, and ~ 600 ps [38] from the NEXT. To see the effect of the level widths in the neutron TOF spectrum, simulation of the ^{17}N neutron emission was performed using NEXTSim [38]. NEXTSim is a GEANT4-based simulation framework developed to characterize the NEXT modules. NEXTSim was updated to incorporate the simulation of an array of NEXT modules mimicking the real experimental scenario. The same experimental setup used at NSCL was rendered in NEXTSim, and the three neutron energies, 383 keV, 1171 keV, and 1700 keV were simulated with and without level widths added. The level widths were taken from Reference [52]. The width of the neutron emitting states added a significant broadening to the neutron peaks, which can be seen in Figure 5.8.

Even though the energy resolution is limited by the timing resolution of the implant detector and the level width of the neutron emitting states, this measurement was successful in demonstrating the neutron interaction position localization capability of NEXT in real β -delayed neutron measurement.

5.3 $^{27}\text{Al}(\text{d}, \text{n})$ Thin Target Measurement

Neutron detection efficiency of various NEXT modules was measured at Ohio University’s Edwards Accelerator Laboratory (EAL), which provides neutrons with a wide energy distribution using $^{27}\text{Al}(\text{d}, \text{n})$ reactions [59]. The key results from this measurement were reported in the Reference [60]. After the efficiency measurements were completed, an additional $^{27}\text{Al}(\text{d}, \text{n})$ measurement was performed with a thin ($\sim 50 \mu\text{g}/\text{cm}^2$) ^{27}Al target to test the energy resolution capability of NEXT. The 7.44 MeV deuteron beam impinging on a thin Al target allowed the measurement of well resolved high energy neutron peaks. A pickoff signal from the beam buncher was used as a reference signal for the neutron TOF measurements.

Two detector modules (EJ276-05 and EJ276-10) were stacked together to achieve higher efficiency in detecting high-energy neutrons and placed at a distance of 5 m from the target assembly, as shown in Figure 5.9.

The raw TOF spectrum for stacked detectors without any correction made for internal scattering is shown in black in Figure 5.10. Using interaction position information, the TOF is corrected for flight path length using Equation 5.1. Once the correction is implemented, the peaks become better resolved, as shown in red in Figure 5.10, signifying the importance of the NEXT's neutron tracking capability in making more accurate and precise energy measurements. Here improvement in the energy resolution is limited by the timing resolution of the pickoff signal (~ 1 ns) used as the start of the TOF and the short transit time (1-2 ns) for the neutrons to traverse the detector thickness.

5.4 ^{106}Nb β -delayed neutron emission

Another demonstration of NEXT's capabilities in β -delayed neutron measurement was carried out at the Argonne National Laboratory (ANL) using the beam from CARIBU Facility. The experiment took place at the focal plane of Modular Total Absorption Spectrometer (MTAS) [61]. As part of a survey of nuclei around ^{106}Mo , ^{106}Nb ($t_{1/2} = 1.02$ s, $P_n = 4.5\%$) ions were implanted on a tape system where the subsequent β -delayed neutron emission was observed from the neutron unbound states of ^{106}Mo , as shown schematically in Figure 5.11. The allotted time for this isotope was only 8 hours.

A silicon photomultiplier (SiPM) based plastic scintillator detector was developed to detect β decays and generate a start signal for neutron TOF measurements. The β detector had to fit into a small space directly behind the tape implant point, so SiPMs were used because of their small form factor. Two 6×6 mm² Sensl J-Series SiPMs were mounted on a single readout board and coupled to a piece of the plastic scintillator (EJ-200). Figure 5.12 shows the two SiPMs through the uncovered plastic scintillator. SiPMs are known for their characteristic dark counting, identical in shape to the pulse of detected photons. A coincidence between the two SiPM signals was required for a valid event in the analysis.

Five NEXT modules (four EJ276-10 and one EJ200-10) were installed with a ~ 30 cm flight path length around the implant position, as shown in Figure 5.13. The raw TOF spectrum for all modules combined without the TOF correction is shown in black in Figure 5.14. Once the TOF correction for flight path length was implemented using Equation 5.1, a clear neutron peak at ~ 760 keV above background was observed and shown in red in Figure 5.14. This first measurement of ^{106}Nb β -delayed neutron emission was important to show why a detector of this design is essential to the future study of neutron-rich nuclei. When isotope production and neutron branching ratios are not sufficient for the traditional neutron TOF detectors, NEXT can be easily adapted to provide a precise and efficient measurement.

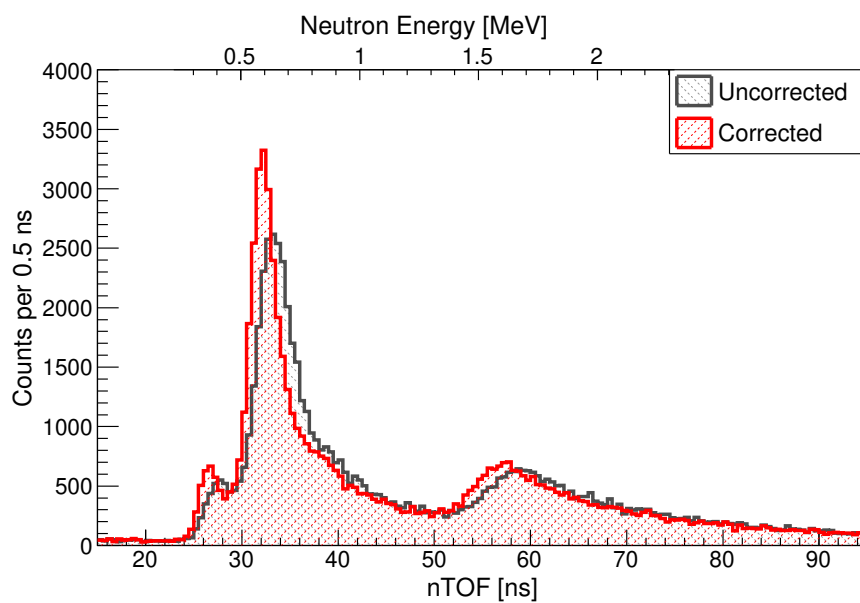
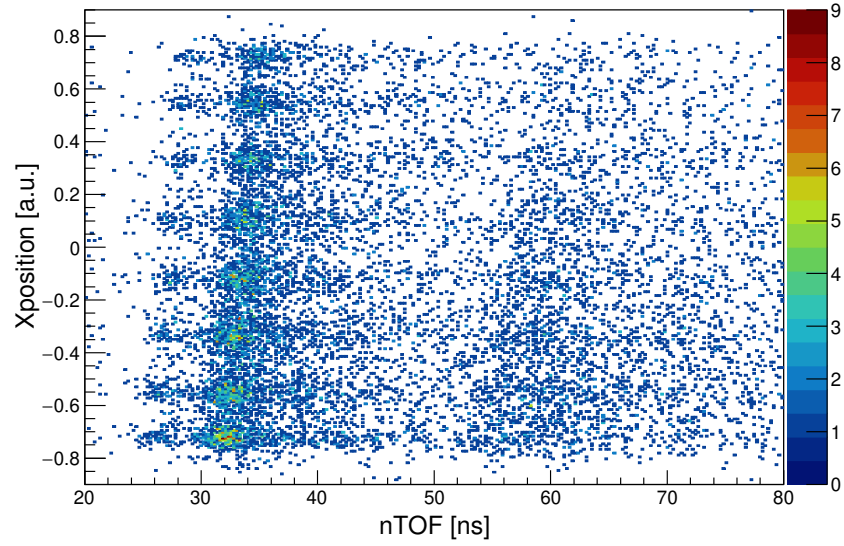
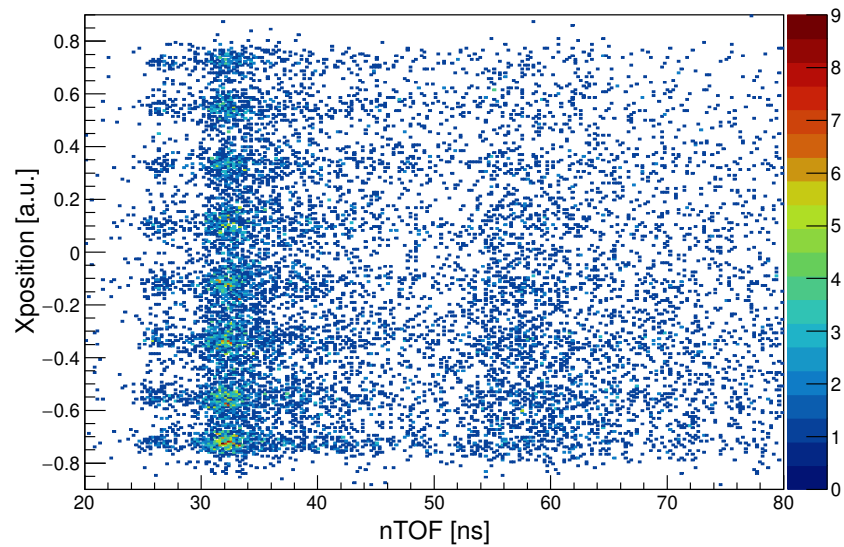


Figure 5.6: The summed neutron TOF spectrum for ^{17}N β -delayed neutron emission before the TOF correction (black) and after TOF correction (red).



(a)



(b)

Figure 5.7: The neutron TOF plotted against the interaction position along the flight path direction (X-position) for one of the NEXT modules before the TOF correction (a) and after the TOF correction (b).

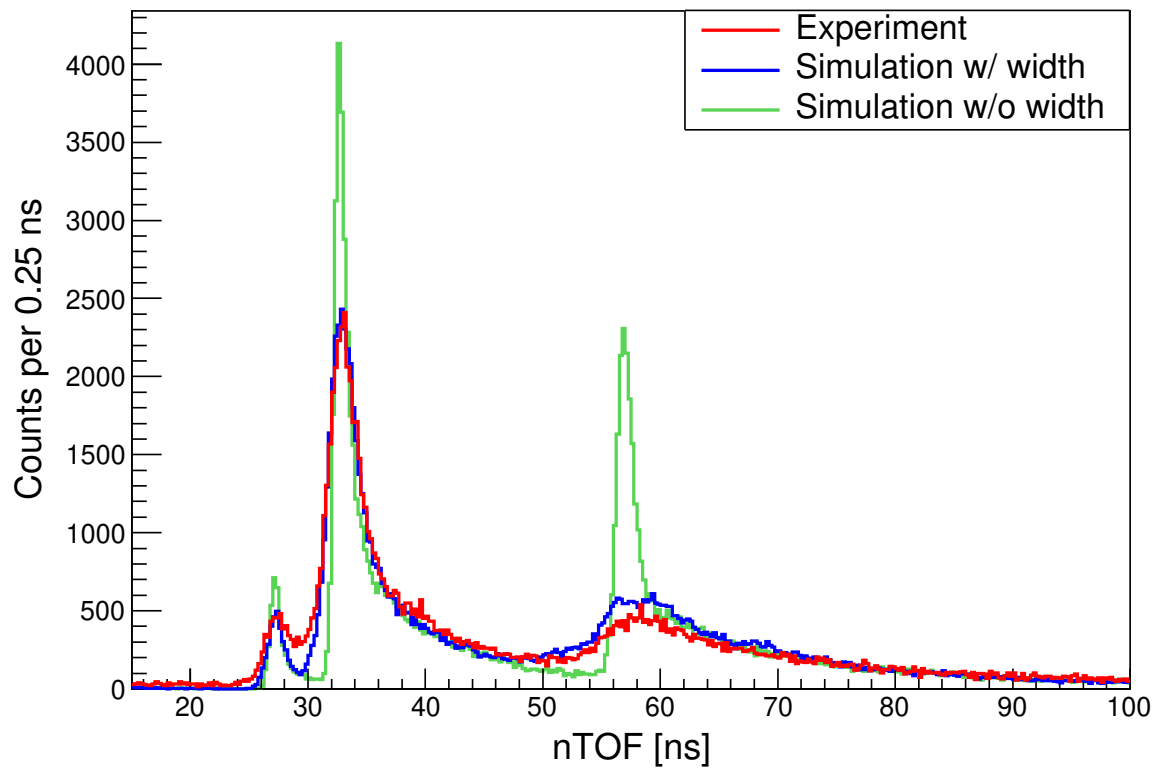


Figure 5.8: The simulation of the ^{17}N neutron emission without widths (green) and with widths (blue) added to the neutron emitting states in ^{17}O , compared with the measured spectrum (red).

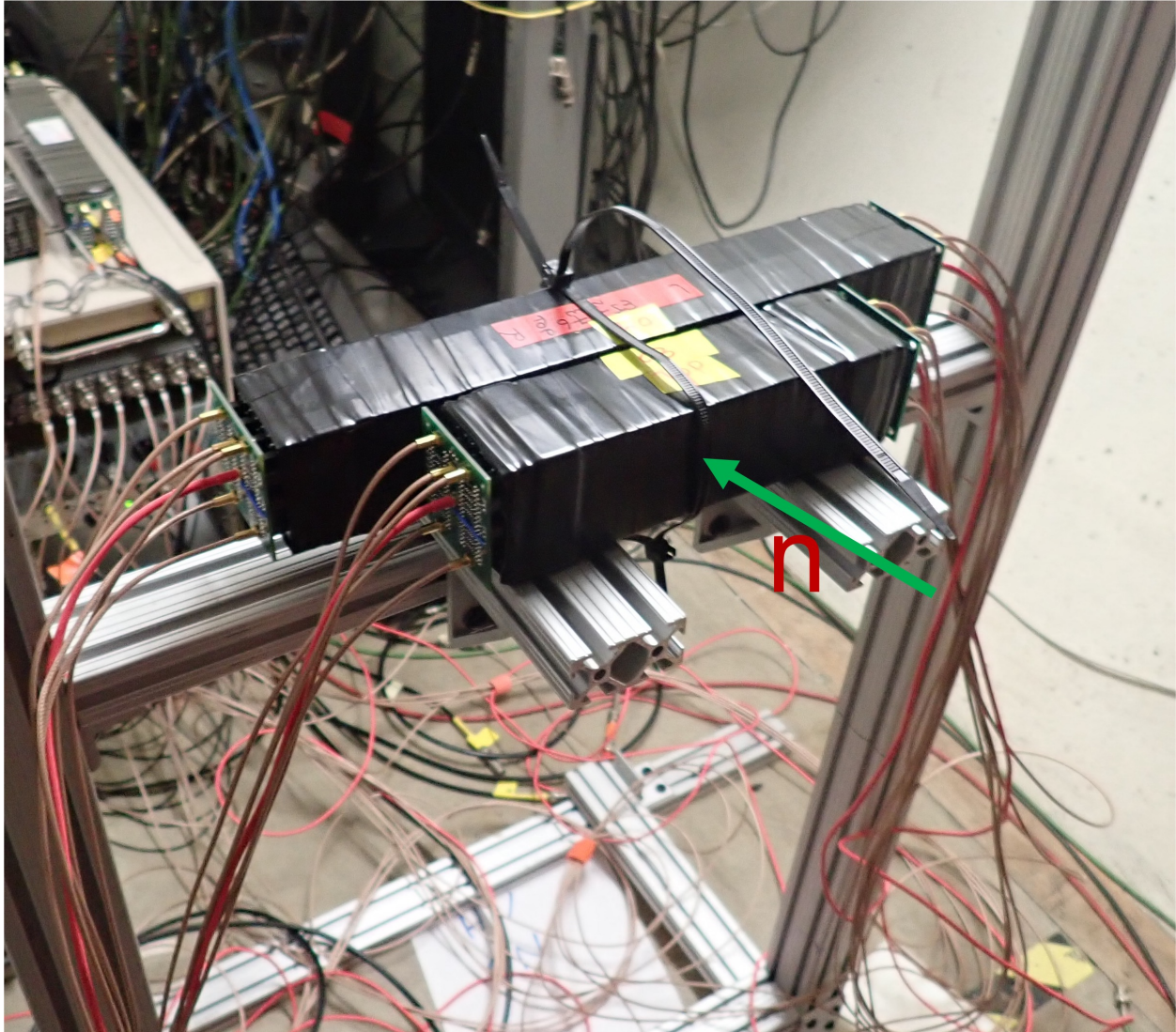


Figure 5.9: The experimental setup at EAL. A 5" and 10" NEXT prototype stacked together to increase neutron detection efficiency for neutrons above 5 MeV.

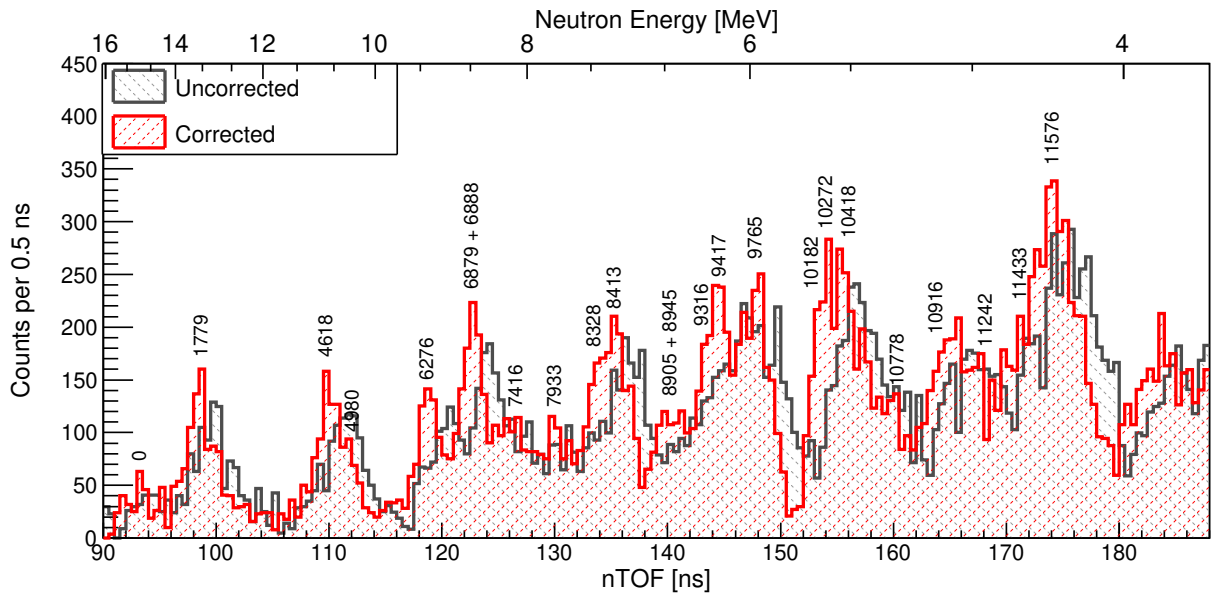


Figure 5.10: The neutron TOF spectra for stacked detectors measured at EAL using $^{27}\text{Al}(d,n)$ reactions at 120° before the TOF correction (black) and after the TOF correction (red). The labels on the neutron peaks on the red histogram represent the corresponding excitation energies in keV in the residual nucleus ^{28}Si taken from previous $^{27}\text{Al}(d,n)$ and $^{27}\text{Al}(d,n\gamma)$ measurements [55, 56, 57, 58].

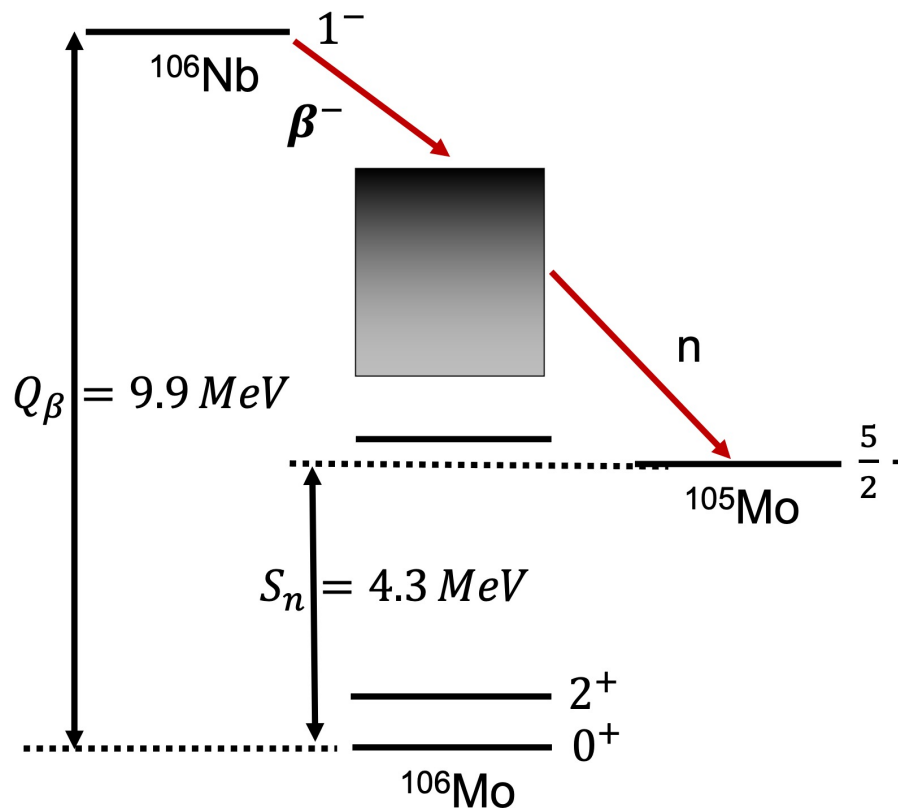


Figure 5.11: The decay scheme of ^{106}Nb . The β decay of ^{106}Nb populates the neutron unbound states in ^{106}Mo , which finally decay to the ground state of ^{105}Mo via neutron emission.

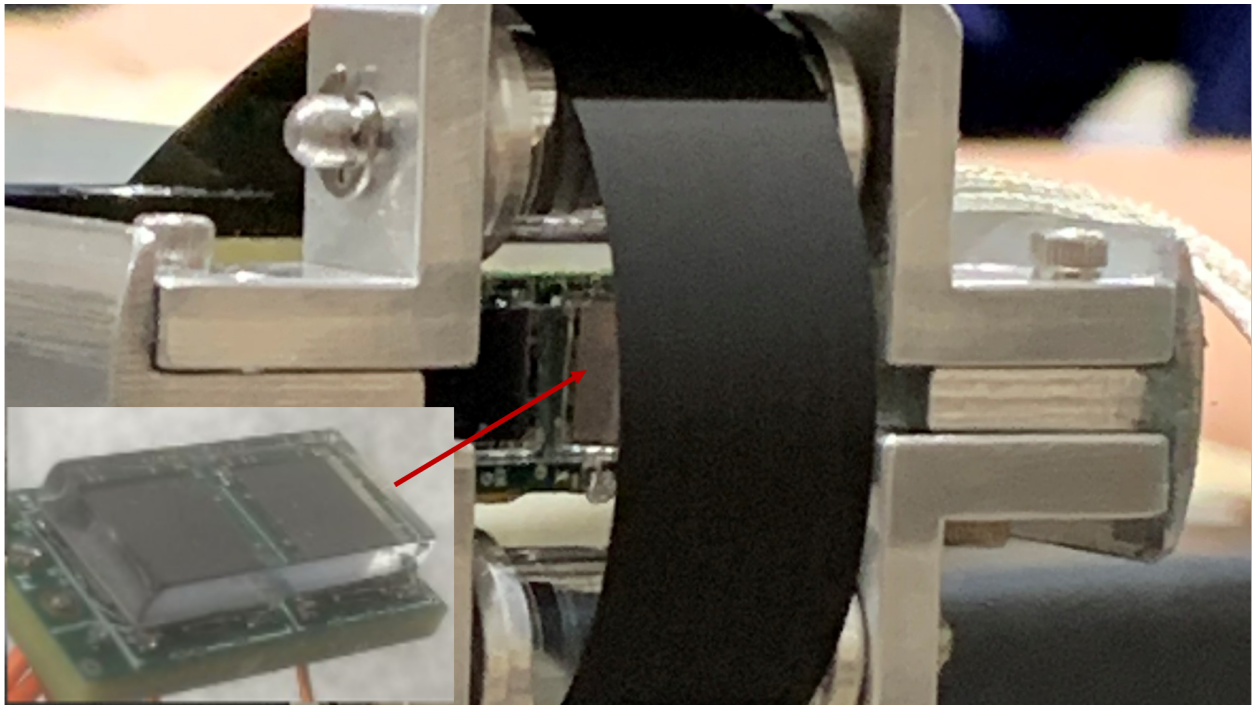


Figure 5.12: Silicon Photomultiplier-based miniature plastic scintillator detector (inset in the lower left) situated behind the front of the tape system where ions are implanted.

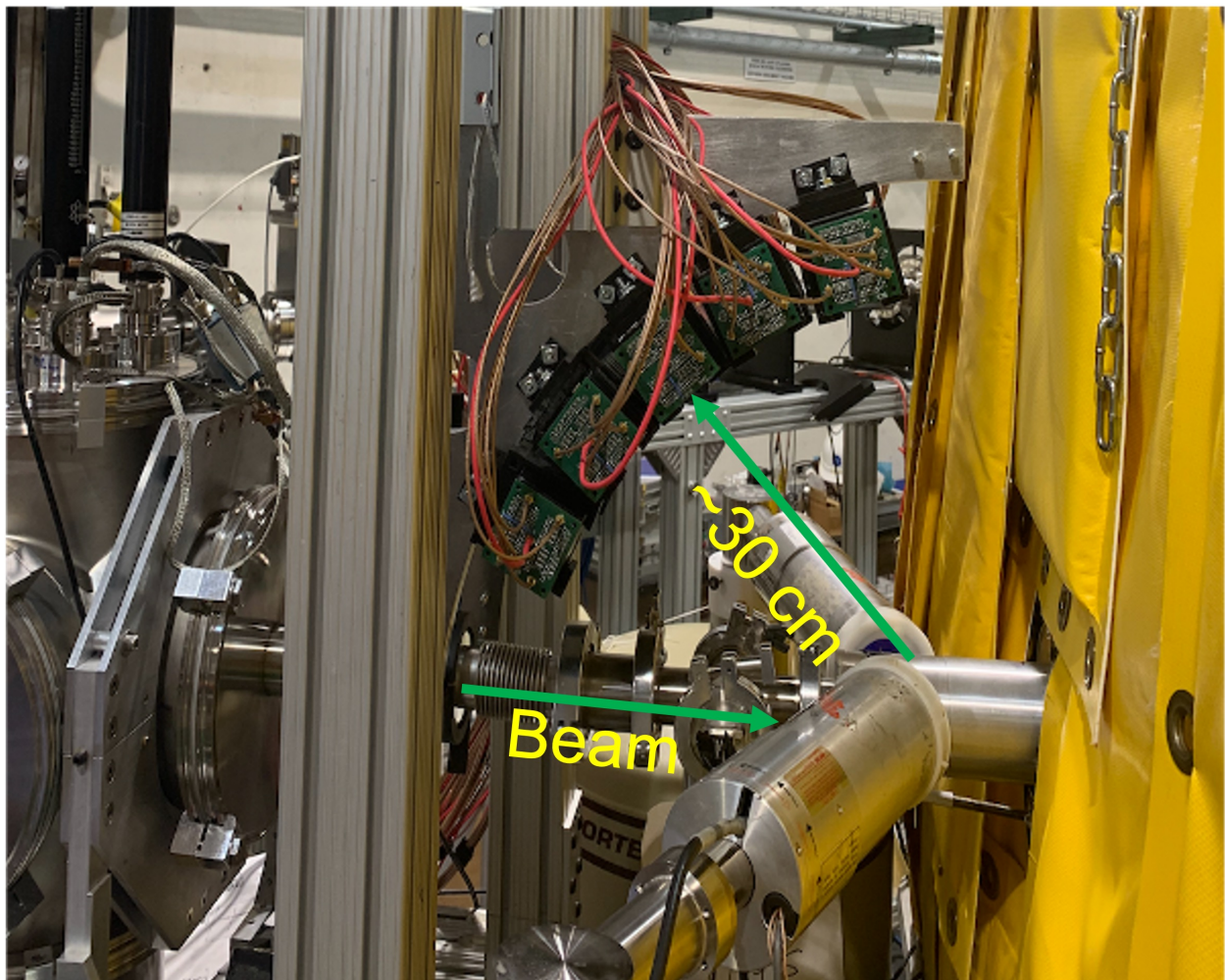


Figure 5.13: Arrangement of the 5 NEXT modules around the beam implant point at the focal plane of Modular Total Absorption Spectrometer (MTAS).

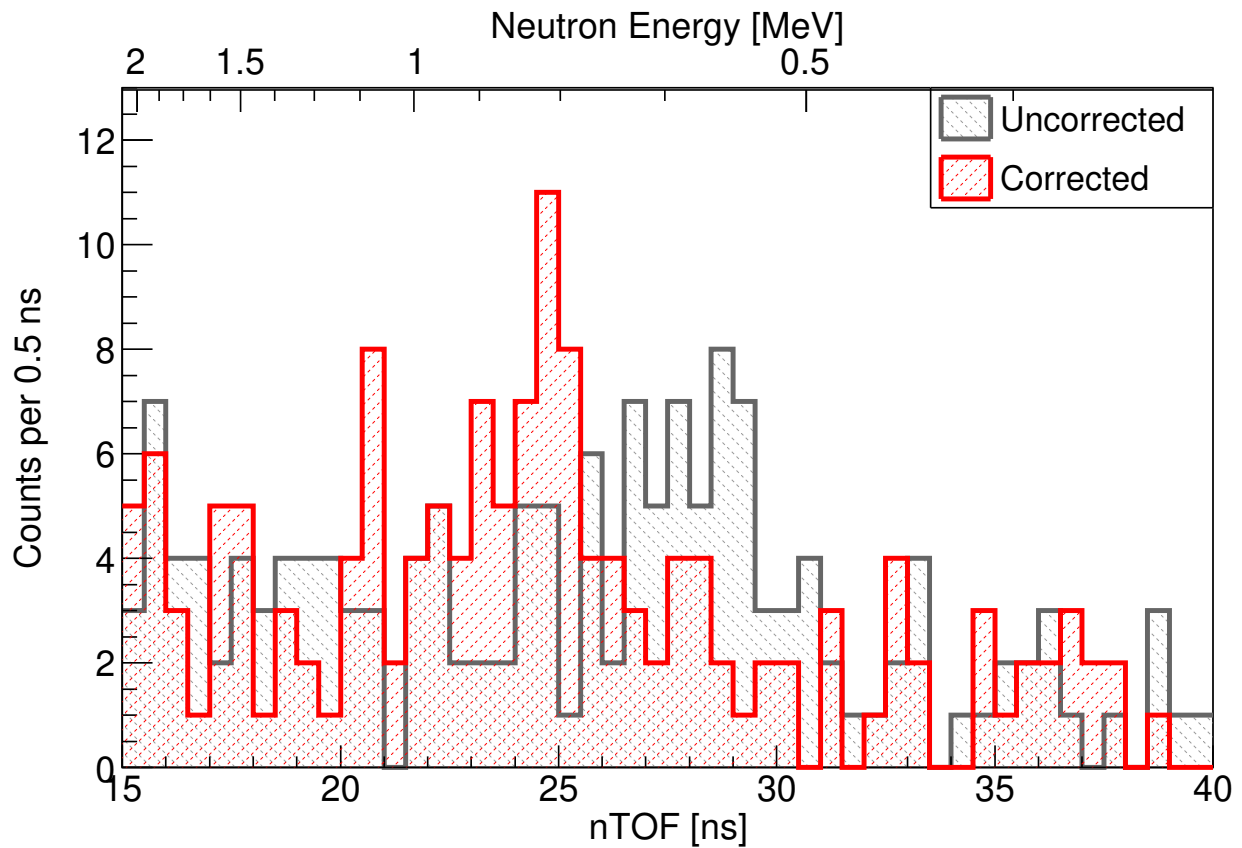


Figure 5.14: The ^{106}Nb neutron TOF spectrum before the TOF correction (black) and after the TOF correction (red). After the correction, a defined peak at ~ 760 keV (25 ns) is observed. As the transit time for 760 keV neutron to traverse the detector thickness (~ 5 cm) is about 4 ns a clear shift of 4 ns in TOF is seen after the correction in the 25 - 29 ns time range.

Chapter 6

Beta-delayed Neutron Spectroscopy of ^{24}O Using VANDLE and NEXT

6.1 Motivation

Large proton-neutron asymmetry plays a vital role in determining the nuclear structure of the neutron-rich nuclei. It is important to explore how the single-particle configuration of the neutron-rich nuclei evolves towards the drip line. One of the prime focuses of the next generation of radioactive ion beam facilities is to study the nuclear structure of neutron-rich nuclei approaching drip-line [37]. Recent experimental measurements observed significant changes in the nuclear structure; for instance, the disappearance of conventional magic numbers and the appearance of new magic numbers [1, 2], the location of the drip line [3, 4], and the neutron halos near the drip line [5]. Currently, very little spectroscopic information is available for neutron-rich nuclei, especially near drip line nuclei. Also, most of the experimental studies focused on studying the nuclear states below neutron separation energy, and minimal information is available for the neutron unbound states. The present measurement focuses on studying the nuclear structure of light drip-line nuclei at and below the island of inversion with the first-ever neutron spectroscopy.

6.1.1 Nuclear Shell Model

Several nuclear models are available to describe the arrangement of the nucleons inside the nucleus. They focus on determining the bulk properties of the nucleus from the microscopic nucleon-nucleon interactions. In the simple shell model picture, the motion of each nucleon is driven by a central potential where the mean field is self-generated by nucleons in the nucleus with the inclusion of corrections from two or three body interactions outside shell closure. Different potentials are included in the shell model to represent the central potential to reproduce experimental observations. The Wood-Saxon potential with spin-orbit interaction successfully reproduced experimentally observed shell closures for the nuclei at and near the valley of stability [62, 63]. The nuclear single-particle levels produced using Wood-Saxon potential with spin-orbit interaction up to nucleon number 50 is shown in Figure 6.1. The magic numbers are the ones corresponding to the number of nucleons filling groups of levels below the large shell gap.

The disappearance of the conventional magic numbers and the appearance of new magic numbers is observed away from the valley of stability toward the neutron-drip line. One of the experimental evidence of the existence of a magic number is the observation of relatively high energy of the first 2^+ excited state in even-even nuclei. For example, the observation of the first 2^+ excited states at 3198(8) keV for ^{22}O [1] and at 4790(11) keV for ^{24}O [2] provided the evidence for $N=14$ and $N=16$ shell closures. In this light, the study of nuclei near the drip line is especially important to see the evolution of single-particle levels.

6.1.2 Previous measurements and knowledge on structure of ^{24}O

^{24}O is a last bound isotope of the Oxygen isotopic chain [64, 65]. Recently, multiple experimental measurements provided the indication of $N=16$ spherical shell closure in ^{24}O , making it doubly-magic drip-line nuclei [66, 67, 2]. The single particle level scheme of ^{24}O is shown in Figure 6.2. The one neutron drip line (after which S_n becomes negative) is experimentally known for Carbon, Nitrogen, and Oxygen at $N=16$, but it rapidly changes to $N=22$ for $Z = 9$ (Fluorine). This sudden jump in drip-line from Oxygen to Fluorine is referred to as the “Oxygen-anomaly” [68]. Thus, studying ^{24}O may provide hints about

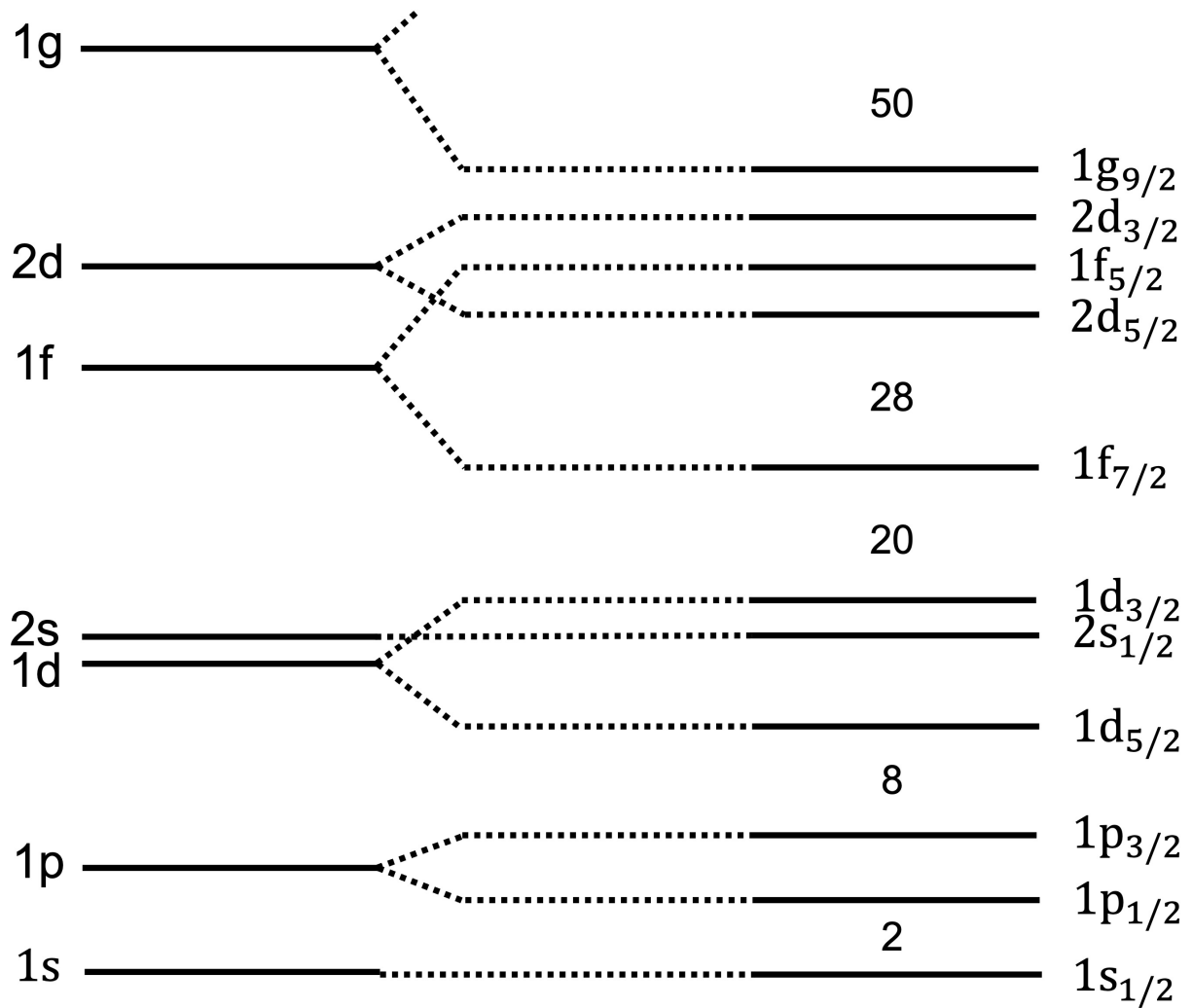


Figure 6.1: Schematic diagram showing the single-particle states with Wood-Saxon potential and the splitting with the inclusion of spin-orbit interaction.

the Oxygen-anomaly and the effects of three-nucleon forces and coupling to the continuum in neutron-rich Oxygen isotopes [68, 69]. It is also an excellent case to benchmark nuclear model calculations near the drip line.

The β decay of ^{24}O was first measured by Mueller et al. [70] at GANIL using 4π neutron detector in coincidence with β particles detected in Si(Li) and they reported decay half-life of 61_{-19}^{+31} ms and neutron branching ratio $P_n = 58(12)$ %. A similar measurement performed by Reed et al. [71] at GANIL reported a decay half-life of 65(5) ms, which agrees within uncertainties with the Mueller et al. but significantly lower neutron branching ratio of $P_n = 18(6)$ %. About 9000 ions of ^{24}O were implanted in the Si telescope detector, and subsequent γ and neutron emissions were detected using four high-volume germanium detectors and 42 ^3He proportional counters, respectively. Also, Penionzhkevich et al. [72] measured a similar half-life and neutron branching ratio of 67(10) ms and 12(8) % respectively. But the most recent measurement performed by Caceres et al. [73] reported a slightly higher half-life of 80(5) ms and neutron branching ratio of 43(4)%. About 10^5 ions of ^{24}O were implanted into a double-sided silicon strip detector (DSSD), and four segmented germanium clover were used to provide β - γ coincidence.

Three γ ray transitions with energies 521 keV, 1309 keV, and 1830 keV associated with 521 keV and 1830 keV levels in ^{24}F were reported by Reed et al. and Caceres et al. Both measurements assigned spin and parity of 2_1^+ and 1_1^+ to 521 keV and 1830 keV respectively by comparing with shell model calculations. This is only the information available on excited states in ^{24}F from β decay measurement, Caceres et al. also performed complementary measurements using in-beam γ spectroscopy. They proposed three new excited states in ^{24}F at energies 2384 keV, 2739 keV, and 3562 keV. But, no information on excited states above neutron separation energies is currently available. The present measurement intends to provide a broad picture of excited states in ^{24}F using γ and neutron spectroscopy.

6.2 Isotope Production and Particle Identification

Isotopes of interest were produced and separated using NSCL's Coupled Cyclotron Facility (CCF) and A1900 fragment separator, respectively [74]. A primary beam of ^{48}Ca was injected

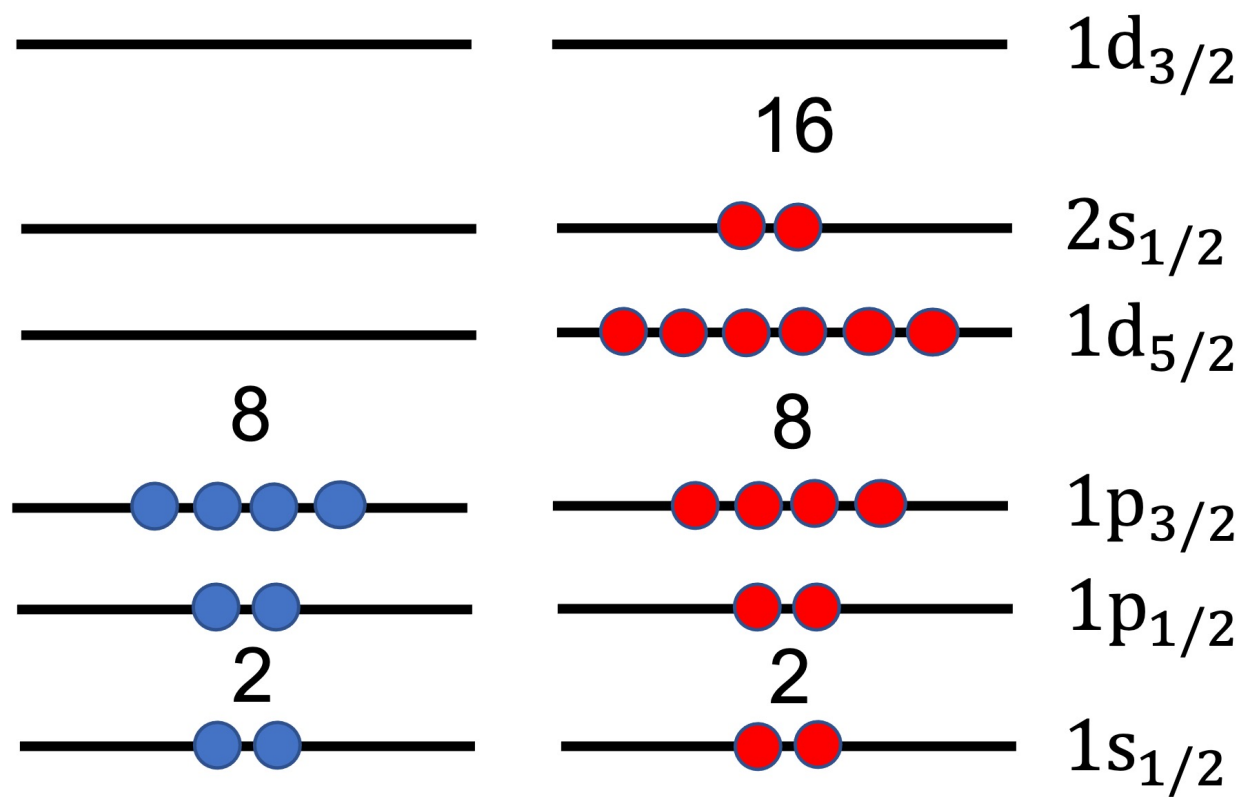


Figure 6.2: Schematic diagram showing the occupation of the single-particle states in ^{24}O .

into an Electron Cyclotron Resonance (ECR) ion source, where electrons were stripped, and $^{48}\text{Ca}^{8+}$ ions were extracted. The partially ionized ^{48}Ca ions were fed into the K500 cyclotron and accelerated to 12.3 MeV/A. The ions were fully stripped using thin carbon foil before feeding into the K1200 cyclotron. A fully stripped ^{48}Ca beam was accelerated to 140MeV/A of 80 pna intensity within the K1200 cyclotron.

A beam of fully accelerated ^{48}Ca ions impinged into a production target (thin foil of beryllium). The fragmentation reactions occurred inside the target, producing a secondary beam of ions. The thickness of the target was optimized to maximize the production rate of nuclei of interest. The isotopes of interest were separated from all other reaction products and guided to the experimental area using an A1900 fragment separator. The layout of NSCL's Coupled Cyclotron Facility and A1900 fragment separator is shown in Figure 6.3. With the momentum acceptance of $\frac{\Delta p}{p} = 5\%$ and solid angle acceptance of $\Delta\Omega = 8 \text{ msr}$, making it a high acceptance fragment separator. The major components of the A1900 separator are four dipoles bent at 45° and eight quadrupole triplets. A1900 utilizes fragment separation method based on magnetic-rigidity and energy-loss in the degrader material [75].

The secondary fragments with a specific momentum-to-charge ratio (mv/q) were selected by the magnetic rigidity ($B\rho$) of the first dispersive half of the A1900 separator. The momentum acceptance can be changed using a slit system installed in all dispersive focal planes to achieve high collection efficiency. Further selection can be accomplished by passing the fragments through a wedge shape energy degrader placed at the image two positions, as shown in Figure 6.3. Fragments with different charges (Z) will experience different energy losses as they pass through the degrader and emerge with different momentum. Thus, the second dispersive half of the A1900 separator provides the isotopic separation. Finally, the isotopes of interest were delivered to the final focal plane of A1900.

The isotopes in the secondary beam transported through the A1900 fragment separator were identified event-by-event utilizing a set of silicon detectors by the time of flight and energy loss measurement. The isotopes were implanted into the implantation detector to observe the β decay. Figure 6.4 shows the identification of all the isotopes implanted into our implantation detector.

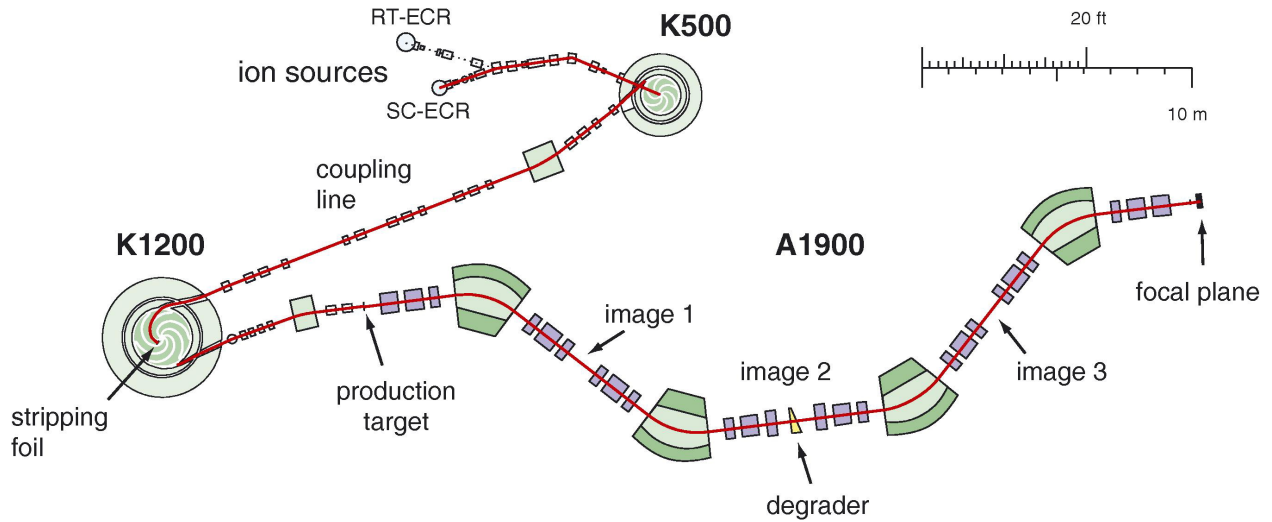


Figure 6.3: A schematic diagram of NSCL's Coupled Cyclotron Facility and A1900 fragment separator [74].

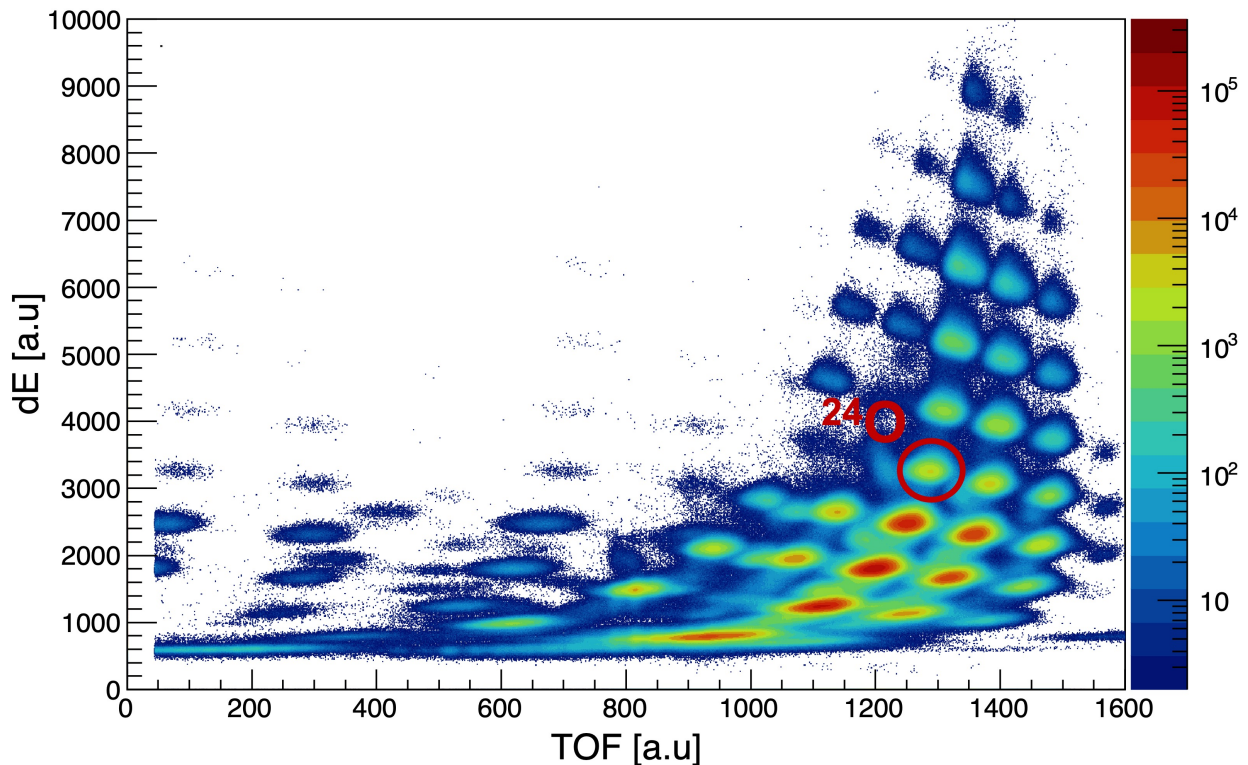


Figure 6.4: Identification of the nuclei produced in the Experiment. The nuclei were identified using the time of flight between silicon detectors and the energy loss in the dE detector. ^{24}O is highlighted in red.

6.3 Experimental Setup

The Experimental setup comprised an implant detector system and neutron and γ detector arrays. The isotopes of interest were implanted in an implantation detector, and subsequent β -delayed γ rays and neutron emissions were observed using γ and neutron detector arrays, respectively.

Yttrium orthosilicate (YSO) based detector was used as an implant detector [54] in this experiment. A segmented array of YSO scintillator of dimensions $48 \times 48 \times 12$ mm³, comprised of 24×24 segments, was coupled to the position-sensitive multianode PMT (H12700B-10) from Hamamatsu Photonics [41] via acrylic light guide of dimensions $48 \times 48 \times 5$ mm³ with similar segmentation as YSO array. The PMT provides 64 anodes and one common dynode signal. The dynode will be used to extract energy and timing information And anodes provide the position information. An Anger logic resistive network was used to read the anode signals from PMT which outputs four signals for the position reconstruction. A similar approach as used for NEXT was implemented to extract the reconstructed interaction position.

Each of the four anode signals and a dynode signal were split and used with two different gain settings in the Pixie-16 digitizer. A set of five signals (four anodes and one dynode) in high gain mode with ten times amplification was used for β events. For ions, signals were used in a low gain mode without amplification. The dynode signal in high gain mode was used as a start of the timing for the neutron time of flight arrays.

Two neutron detector arrays were used for the β -delayed neutron measurement. The first is the Versatile Array of Neutron Detector at Low Energy (VANDLE). VANDLE is a plastic scintillator-based neutron time of flight array [28]. A full array consisting of 48 VANDLE bars, each with dimensions of $120 \times 5 \times 3$ cm³, was placed at a distance of 105 cm from the center of the implantation detector. A newly developed segmented neutron array NEXT was also used alongside the VANDLE. Ten NEXT modules were arranged at a distance of 50 cm from the center of the YSO array. Three high-purity germanium detectors (Clovers) were used for the γ ray detection. Figure 6.5 shows the experimental setup with all detector systems and supporting materials.

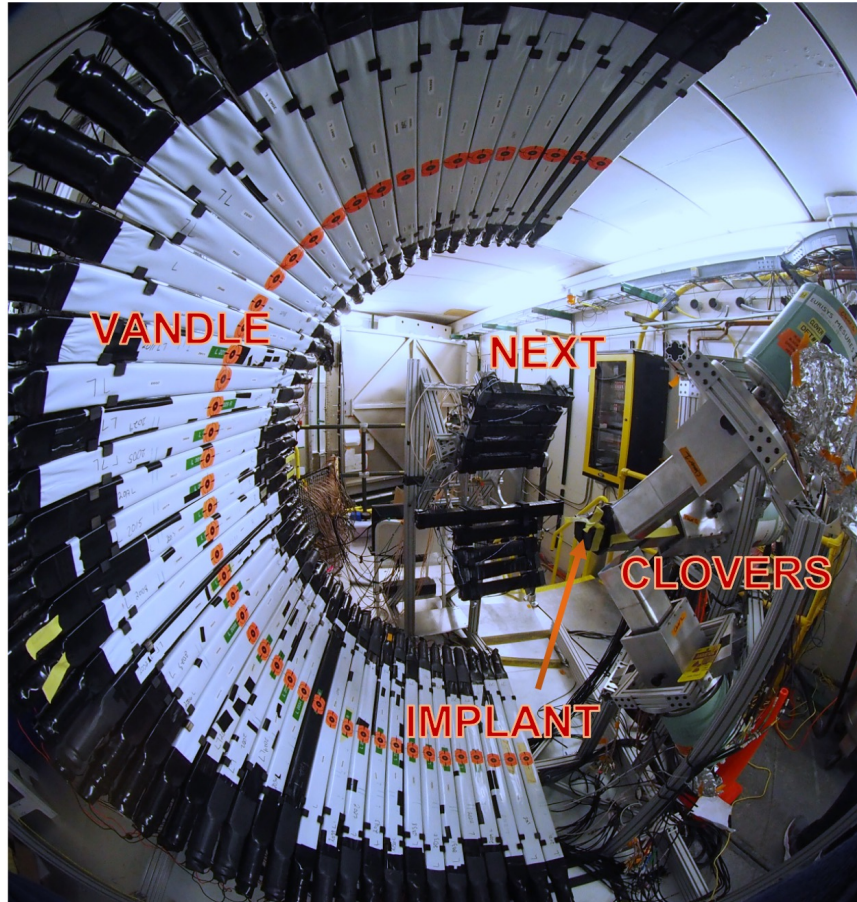


Figure 6.5: The experimental setup at NSCL. The setup comprised of implant detector, neutron detector arrays (VANDLE and NEXT) and γ ray detectors (Clovers).

6.4 Ion-Beta Correlations

One of the important tasks in β decay spectroscopy is establishing a correlation between implanted ions and corresponding β events. For this, the timing and position information of the implanted ion is recorded. After a characteristic time, the ion will undergo β decay, and the emitted β particle will be detected, as shown schematically in Figure 6.6a. The time and position of the β particle are also recorded and correlated with the corresponding implanted ion based on time and position information. A position gate (correlation radius, r) is determined utilizing x-y positions of ion (x_{ion}, y_{ion}) and β particle (x_{β}, y_{β}) using equation 6.1. The β and ion position profile for a particular nucleus is shown in Figure 6.7. The optimal correlation radius was determined to have a high β detection efficiency. The correlated events within the pre-defined gate, shown schematically in Figure 6.6b, were considered valid events for the analysis.

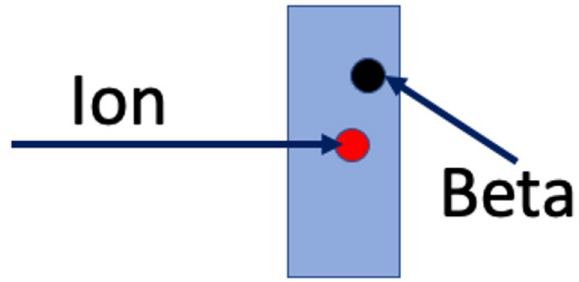
$$r = \sqrt{(x_{\beta} - x_{ion})^2 + (y_{\beta} - y_{ion})^2} \quad (6.1)$$

6.5 Analysis of the ^{24}O Decay

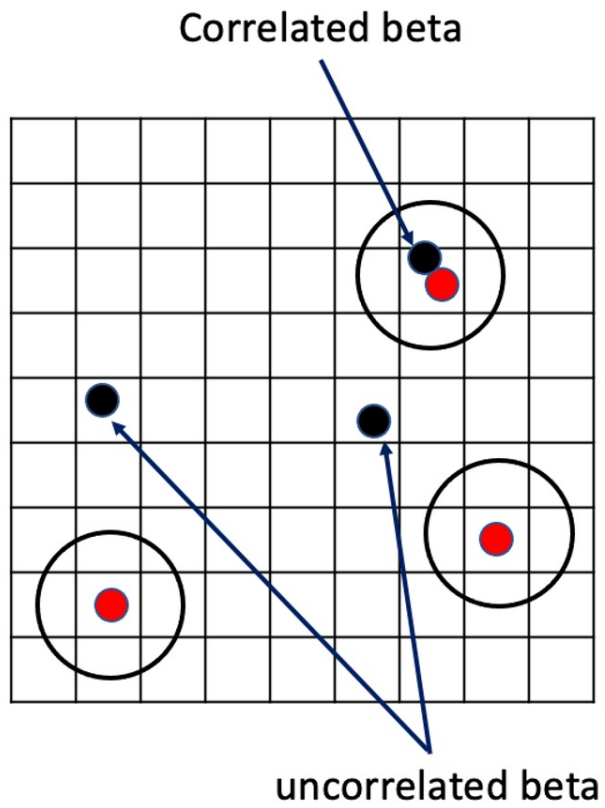
Doubly magic ^{24}O was one of the Oxygen isotopes implanted in the implantation detector. ^{24}O , with a Q_{β} value of 10.96 MeV, β decays to ^{24}F which eventually undergoes a β -delayed neutron emission to ^{23}F . The possible decay chain of ^{24}O is shown in Figure 6.8, where black boxes indicate stable nuclei.

6.5.1 Half-life Determination

β decay half-life can be determined using a decay curve, which represents the time distribution between implanted ion and subsequent β decay events ($T_{\beta} - T_{ion}$) within a given correlation timing window and radius. Because of the large neutron excess, the daughter and granddaughter of β decay, and the daughter and granddaughter from the β -delayed neutron branch can still be radioactive. The decay curve should include the contribution from all the nuclei. In the case of the ^{24}O , because of the longer half-life of other descendants, only the contributions from ^{24}F and ^{23}F to the total decay curve were included. The decay

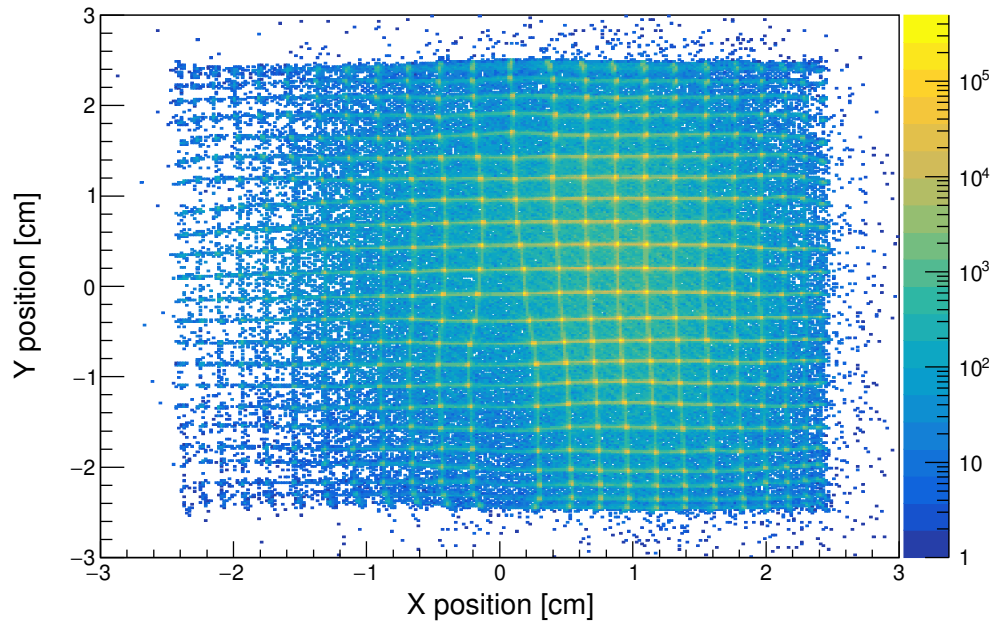


(a)

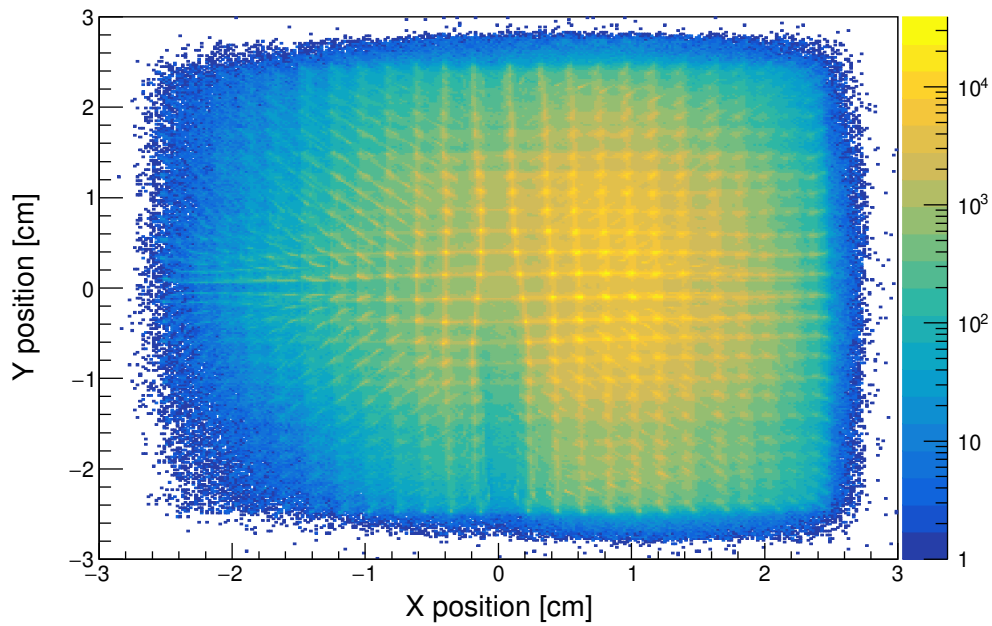


(b)

Figure 6.6: (a) A schematic showing the ion implantation and subsequent beta particle emission. (b) An illustration of the ion-beta correlation. The ion and β events within a given correlation radius were considered valid events in the analysis.



(a)



(b)

Figure 6.7: Ion(a) and Beta(b) position profiles.

activity of parent nuclei and the growth activities of daughters and granddaughters are well described by a set of equations called Bateman equations [76]. The half-life of the implanted nuclei is obtained by fitting the experimental time spectrum using a theoretical function (Bateman equations). The decay curve obtained for the ^{24}O decay is shown in Figure 6.9 within a correlation timing window of 1000 ms and correlation radius of 0.35 cm. The decay curve was fitted with the Bateman equations, and the half-life of 125(9) ms was obtained from the fit. The error includes statistical and systematic errors from the uncertainties from preset parameters in the fitting such as half-lives of descendants and neutron branching ratio of parent nuclei. The half-life obtained in this work is longer than the literature value [70, 71, 72, 73]. But, the analysis procedure was verified by extracting the half-lives of other nuclei in this region, which agrees well with the literature value, as summarized in Table 6.1.

6.5.2 Background Estimation for Neutron and Analysis

The decay curve obtained for the ^{24}O decay is shown in Figure 6.10 for an ion-beta correlation time window of -500 to 500 ms, which sits on the top of the huge background. The background is due to the random correlation of the events with other implanted ions. The random background has a slope going upward towards $T_\beta - T_{ion} = 0$. The slope is due to the beam fluctuation during the experiment.

For the neutron TOF analysis, the background was determined by gating on the negative time window (-T) of the decay curve. The correlated neutron spectrum was then obtained by subtracting the background spectrum from the neutron spectrum gated on the positive time window (T) bin-by-bin basis, as represented schematically in Figure 6.10. A similar approach was implemented for the γ ray analysis.

6.5.3 Gamma Ray Analysis

The β -gated γ ray spectrum following the decay of ^{24}O within the ion-beta correlation time window of 500 ms is shown in Figure 6.11. The γ rays at 521, 1309, and 1830 keV were observed in this analysis, which were reported in previous β decay measurements [77, 73].

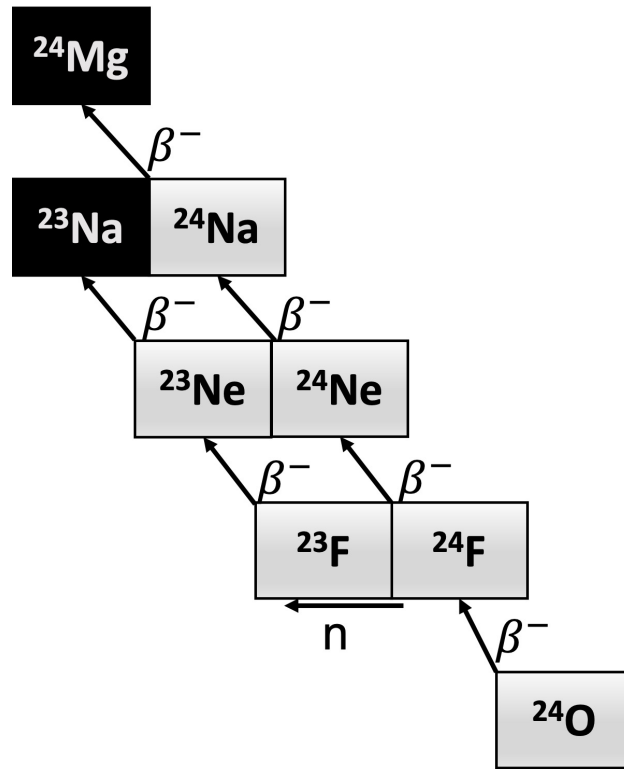


Figure 6.8: Possible ^{24}O decay chain leading to the stable nuclei indicated by black boxes.

Table 6.1: The half-lives for various isotopes obtained in this work compared with literature values.

Isotope	This work (ms)	Literature (ms)
^{24}O	125(9)	80(5)
^{23}N	15.8(1.5)	14.1(1.4)
^{22}N	23(1)	23(3)
^{20}C	92(2)	90(2)

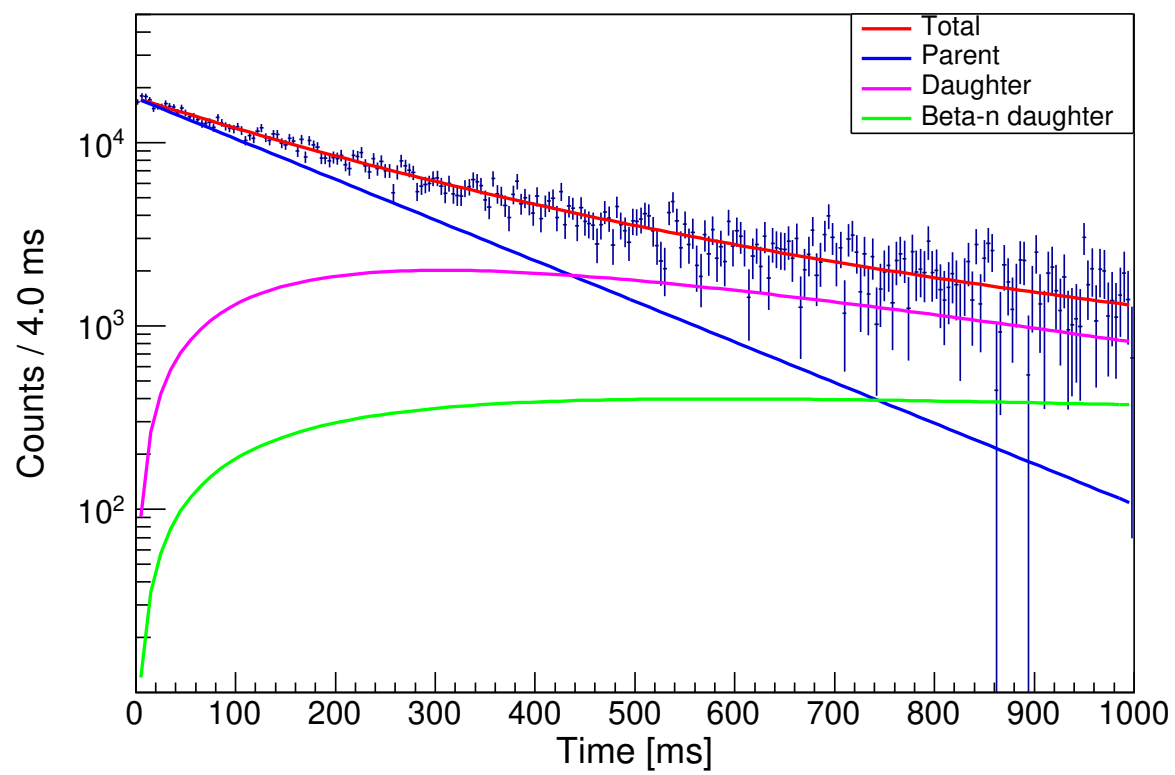


Figure 6.9: The decay curve for ^{24}O fitted with Bateman equations.

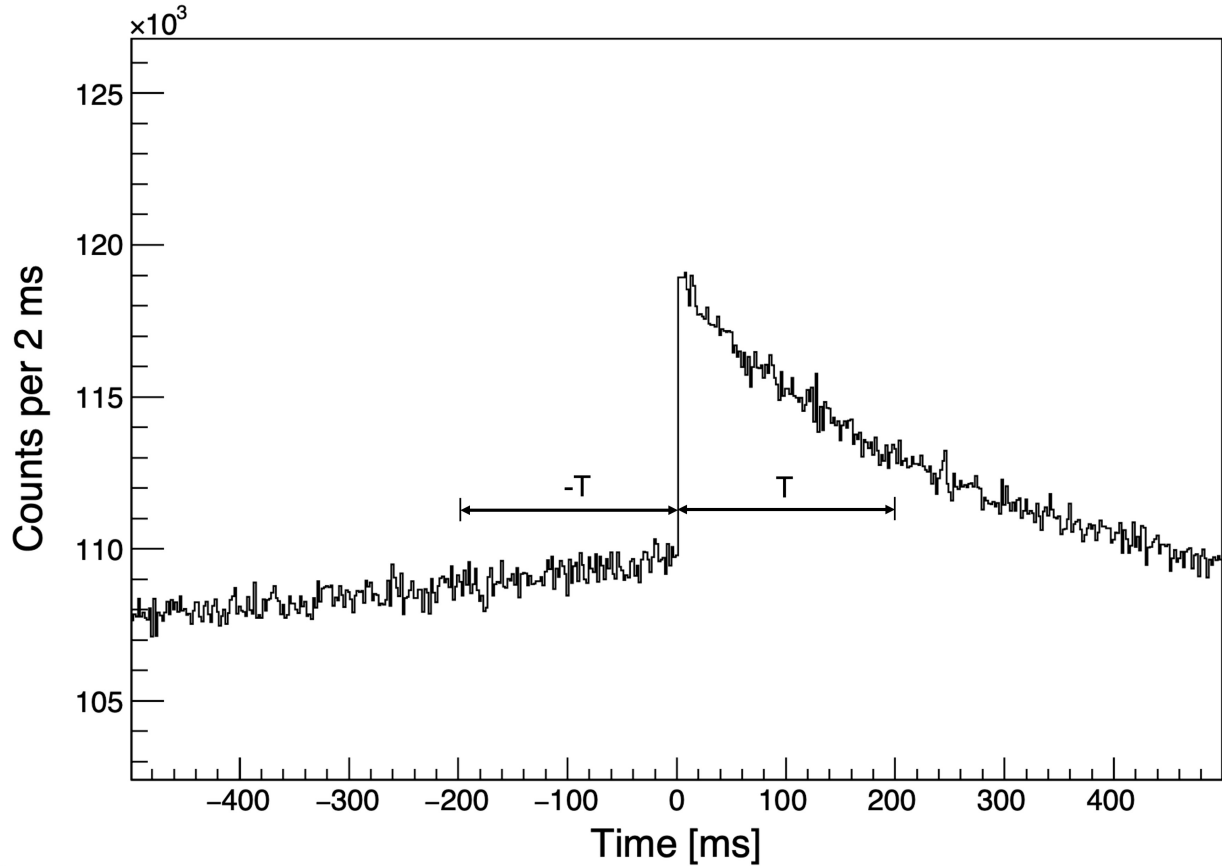


Figure 6.10: The decay curve obtained for ^{24}O with the ion-beta correlation window of -500 to 500 ms. The decay curve sits on the huge background, which arises due to the random correlation with other implanted ions. The random background has a slope going upward towards $T_\beta - T_{ion} = 0$. The slope is due to the beam fluctuation during the experiment.

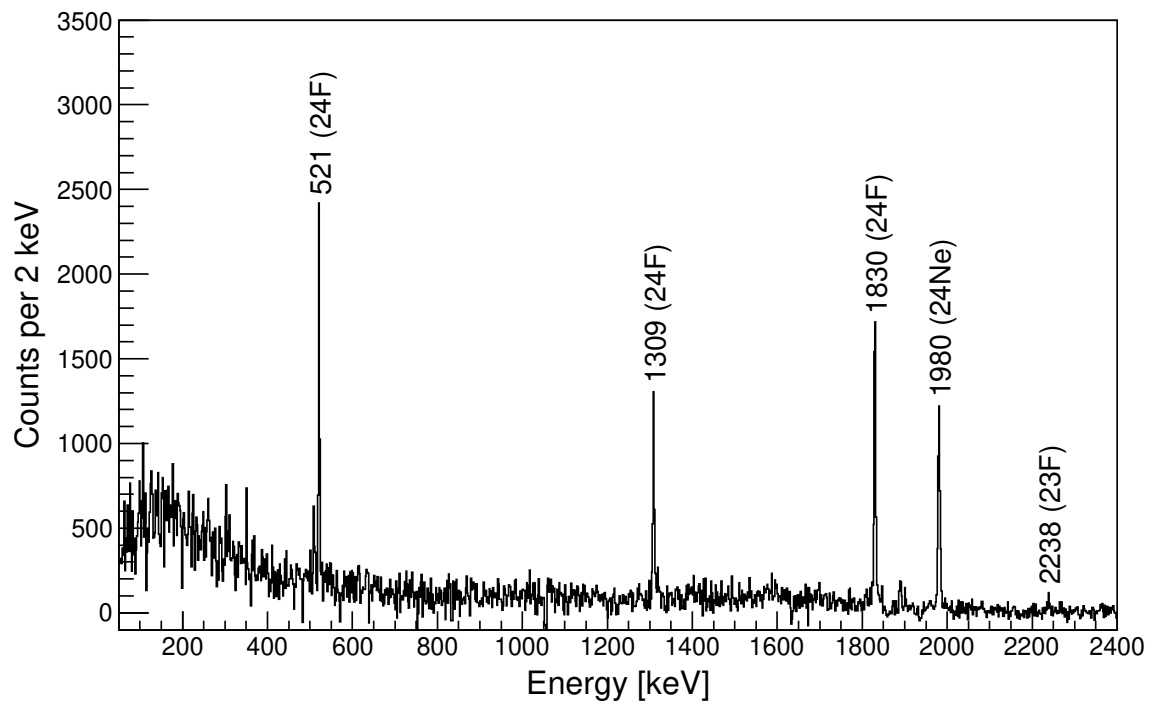


Figure 6.11: γ ray spectrum following the decay of ^{24}O occurring within 500 ms of implantation.

These were attributed to the transitions in ^{24}F , which has ground state spin and parity of 3^+ and neutron separation energy of $S_n = 3.81$ MeV. The first excited 1^+ state at 1830 keV was populated in the β decay, which decays by emitting cascades of 521 and 1309 keV γ rays, as shown schematically in Figure 6.12. The 1309 keV γ ray originating from 1830 keV state populates 2^+ state at 521 keV. The 1830 keV state also has a competing branch that directly feeds the ground state of ^{24}F . The logft value of 4.3(0.1) was obtained for the 1^+ 1830 keV state, which favors the Gamow-Teller transition.

The observed γ ray at 1980 keV was assigned to the $2^+ \rightarrow 0^+$ transition in ^{24}Ne following the β decay of ^{24}F [78]. A very weak γ ray was also observed at 2238 keV which assigned to the first excited state in ^{23}F [79], meaning majority of neutrons emission from excited states of ^{24}F populate ground state of ^{23}F .

6.5.4 Analysis of Neutron Time-of-Flight Spectrum

Detector's Response Function

To properly analyze the experimental neutron TOF spectrum, the detector's response function needs to be extracted using simulations and calibration data. Each neutron TOF detector array has its characteristic response based on neutron scattering from the surrounding materials. The response function should incorporate the TOF spectrum's features due to scattering from the surrounding materials. To extract the response function, the whole experimental setup was rendered in GEANT4, as shown in Figure 6.13, and mono-energetic neutrons with energy ranging from 200 keV to 5 MeV were simulated. For each set of simulations, an isotropic point neutron source with specific energy was placed at the center of the YSO implantation detector, and the TOF of neutrons arriving at each detector array was measured. Figure 6.14 shows an example of the simulated TOF spectrum for the NEXT array for 1 MeV neutrons. The TOF spectrum for each neutron energy was fitted with an asymmetric Lorentzian-shaped function plus three exponential decay tails, and response parameters were extracted. The parameters were plotted against the corresponding TOF centroids, and energy-dependent parametrization was extracted from the various polynomial

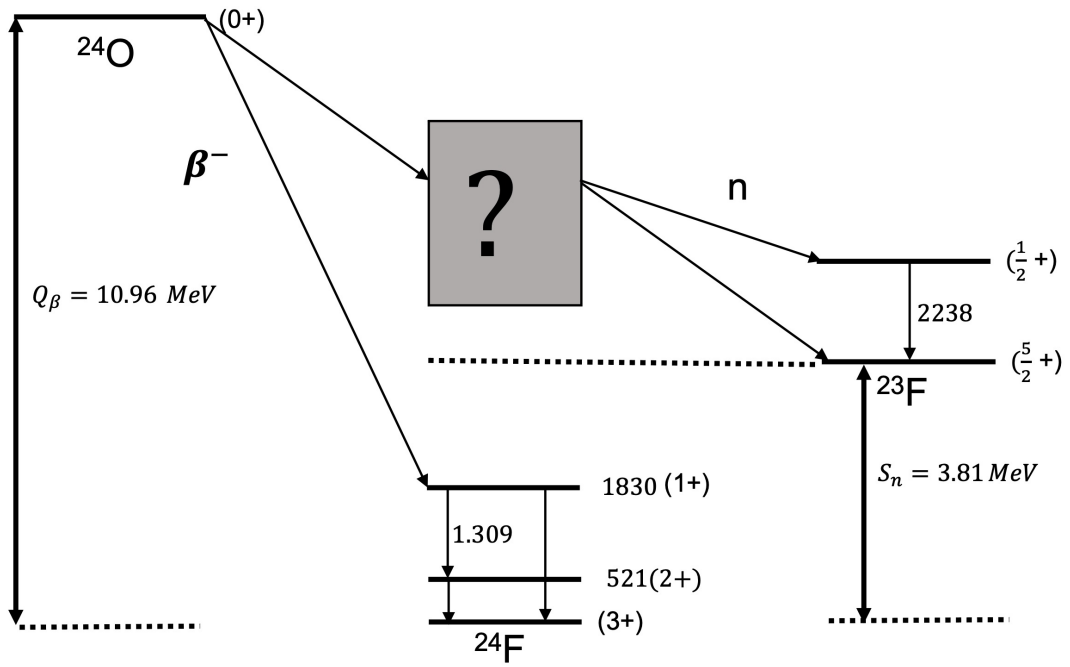


Figure 6.12: Schematic diagram of ^{24}O decay and consequent β -delayed neutron emission.

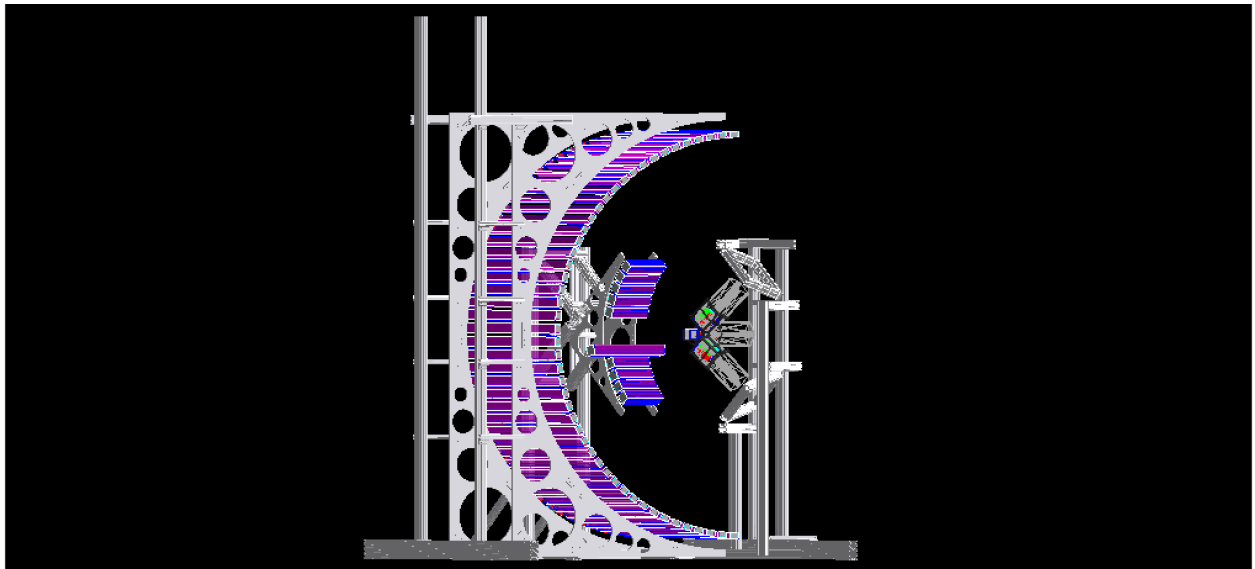


Figure 6.13: A screenshot of the GEANT4 graphical user interface showing experimental setup with all detector systems and supporting materials.

fitting. Using this parametrization, the energy-dependent detector response function was constructed and used to deconvolve the experimental TOF spectra.

The response function extracted using simulation was verified with the online calibration data taken with ^{17}N . The β decay of ^{17}N is well known for its subsequent neutron emission at energies of 383 keV, 1171 keV, and 1700 keV [52, 53], which are suitable for calibrating the neutron detector arrays. The β -delayed neutron time-of-flight spectra for ^{17}N for VANDLE and NEXT are shown in Figure 6.15. The spectra were fitted with the respective response function. The response function was not wide enough to adequately capture the experimental spectrum. The width of the Lorentzian-shaped function needed to adjust until it fits well with the measured spectrum. The total analytical response function is shown in red in Figure 6.15, with the contribution from individual neutron peaks shown in blue.

Neutron TOF Spectrum and Deconvolution

The neutron time-of-flight spectrum for each neutron array was obtained within the ion-beta correlation time window of 500 ms. Since daughter and β -delayed neutron emission daughter have relatively long half-lives and small neutron branching ratios, it was safe to consider a longer ion-beta time correlation window for neutron spectra. The neutron “singles” TOF spectra (no neutron- γ coincidences) obtained for the VANDLE and NEXT arrays are shown in Figure 6.16a together with the analytical fitting functions. Since the two neutron emission is energetically prohibited, the contribution was solely from one neutron emission. Each neutron “singles” spectrum was fitted with the corresponding detector response function to deconvolve into the energies. A few well-defined neutron transitions are seen in both arrays. Because of a very weak population of ^{23}F excited states, it was not possible to extract the γ -gated neutron spectrum. Due to the low geometric efficiency of the NEXT array, the following analysis is based on the VANDLE TOF spectrum.

By normalizing the total number of neutrons feeding to the excited and ground state of ^{23}F to the total number of β decays, the neutron branching ratio of 28(3)% was obtained for ^{24}O . The excitation energy, branching ratio, and logft value for each neutron emitting state identified in ^{24}F are summarized in Table 6.2. The branching ratio for the individual level was obtained by normalizing the number of neutrons feeding to that particular level to the

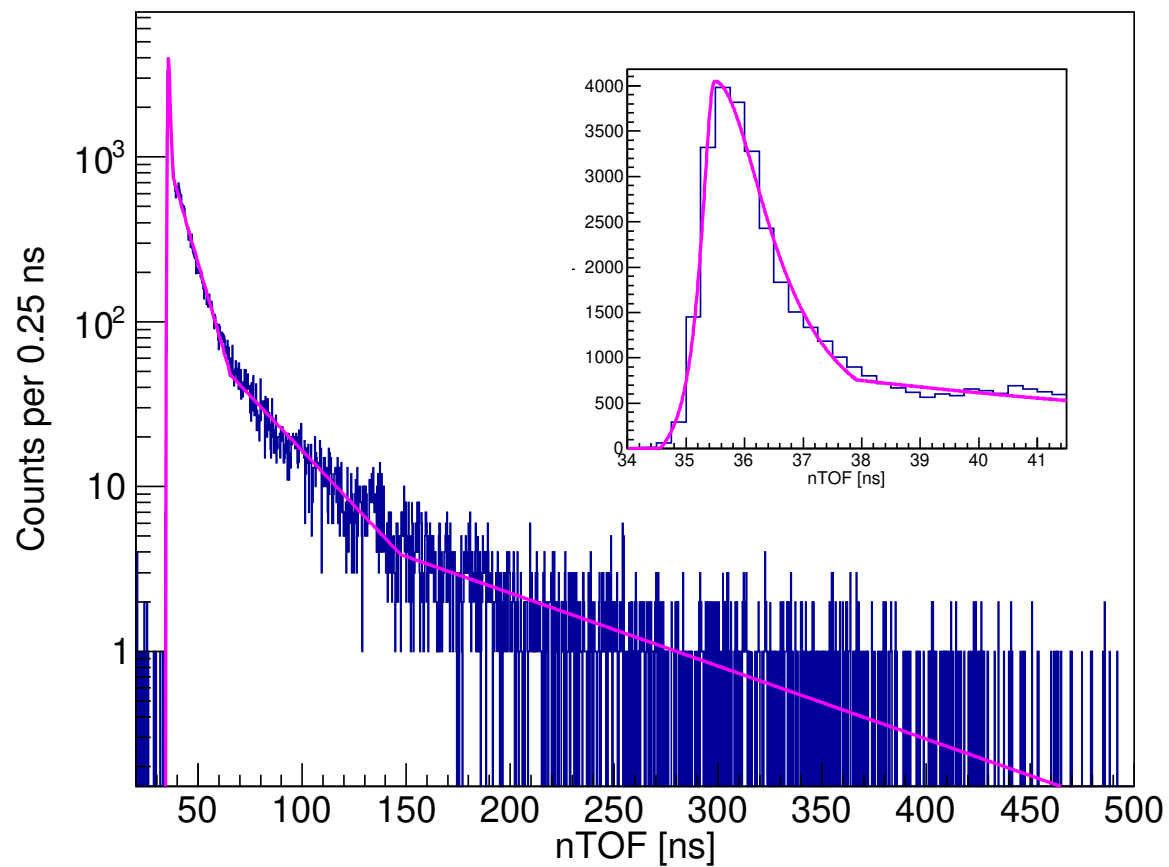
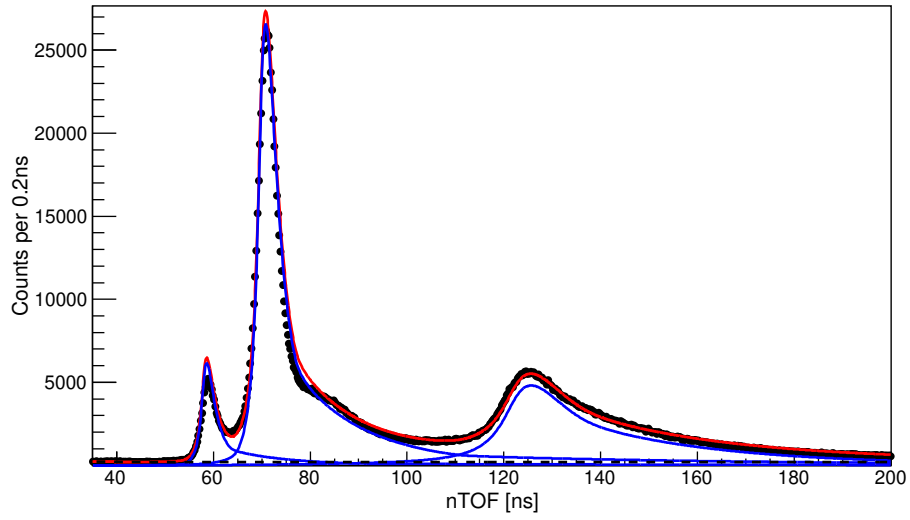
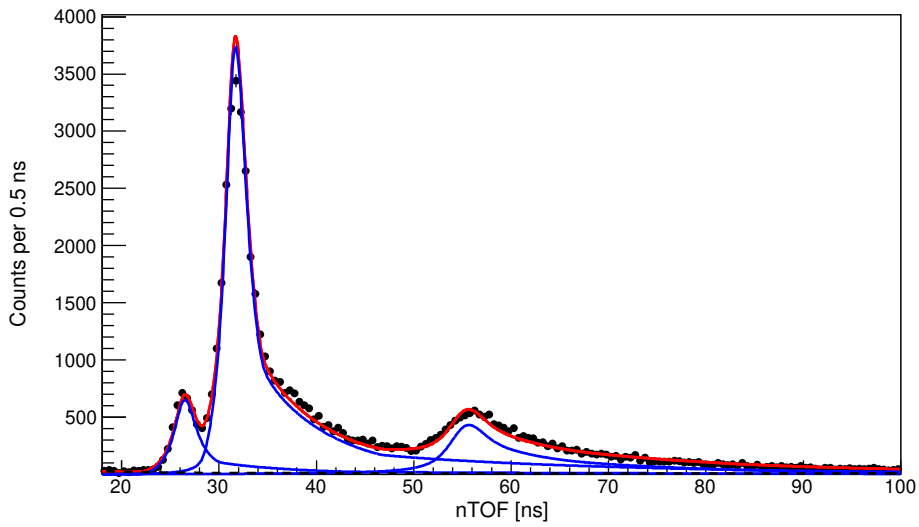


Figure 6.14: The simulated TOF spectrum for NEXT array for 1 MeV neutrons fitted with an asymmetric Lorentzian-shaped function plus three exponential decay tails. The inset shows the TOF spectrum zoomed around the TOF centroid.

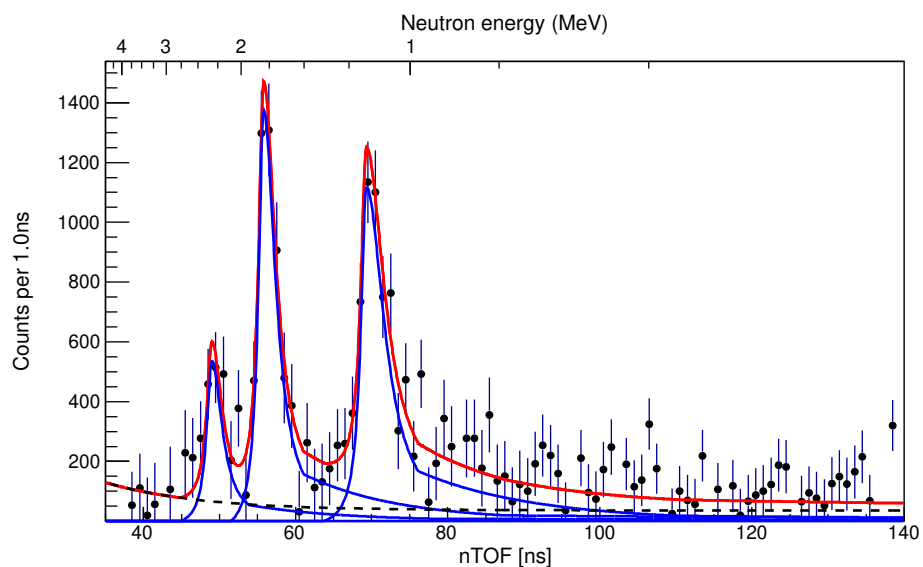


(a)

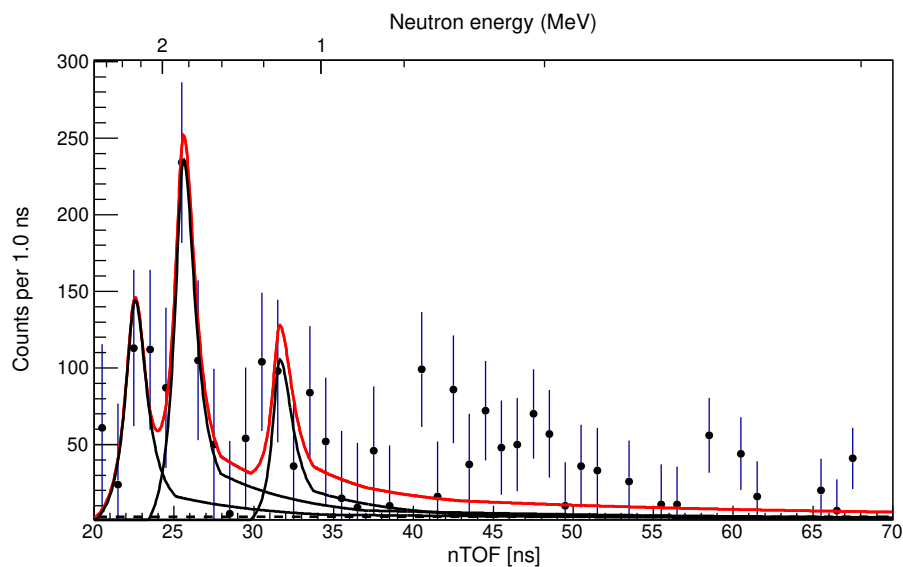


(b)

Figure 6.15: ^{17}N β -delayed neutron time-of-flight spectrum (black) fitted with detector response function. The total fitting function is represented in red, and the contribution from individual neutron peaks are shown in blue. a) for VANDLE and b) for NEXT.



(a)



(b)

Figure 6.16: Neutron singles TOF spectrum for a) VANDLE and b) NEXT within 500 ms of ion-beta correlation time window with the total fitting function plotted in red. Also, a contribution from the individual peak is shown in blue for VANDLE and black for NEXT. The dotted black line represents the background. The energy obtained from VANDLE spectrum deconvolution was used as a fixed parameter for NEXT spectrum deconvolution.

total neutron branching ratio. For three major neutron transitions, $\log ft$ values ranging from 3.9 - 4.1 were found. This favors the Gamow-Teller transitions with the spin and parity of 1^+ . The Gamow-Teller transition reduced matrix elements $B(GT)$ obtained for each neutron transition is shown in Figure 6.17.

6.5.5 Comparison with Shell Model Calculations

The experimental excitation energies and Gamow-Teller transition matrix elements ($B(GT)$) were compared to the predictions of theoretical calculations. The Shell Model calculations were performed using KSHELL [80] with standard USD-type interactions (USDA, USDB) [81, 82] and the interactions obtained using the In-Medium Similarity Renormalization Group (IMSRG) method [83, 84].

The USD Hamiltonian consists of 63 sd-shell two-body matrix elements, and three single-particle energies [81]. The initial version of USD Hamiltonian was obtained by performing least squares fitting of 380 states in 66 sd-shell nuclei, which successfully predicted the nuclear properties of $A = 16-40$ nuclei near the valley of stability. The prediction for the near drip-line nuclei was also reasonably good, but with the unavailability of experimental data for those nuclei at the time, the single-particle energies needed to be extrapolated. This Hamiltonian was modified to include updated single-particle energies and binding energies. New versions of the USD-type interactions are referred to as “USDA” and “USDB” [82]. The new interactions included 608 states in 77 sd-shell nuclei to perform least squares fitting. The only difference between USDA and USB is the fitting procedure; USDB provided a better fit to the data. On the other hand, IMSRG is a novel ab initio method that utilizes a continuous unitary transformation of many-body Hamiltonian to suppress off-diagonal matrix elements, leading to a band or block-diagonal form.

The ^{24}F energy levels were calculated using different interactions are shown in Figure 6.18. Both USDB and IMSRG interactions produced a good agreement with the measured levels. The Gamow-Teller transition reduced matrix elements ($B(GT)$) were also calculated using the same interactions. Figure 6.19 shows the $B(GT)$ obtained from calculations compared with the experimental values.

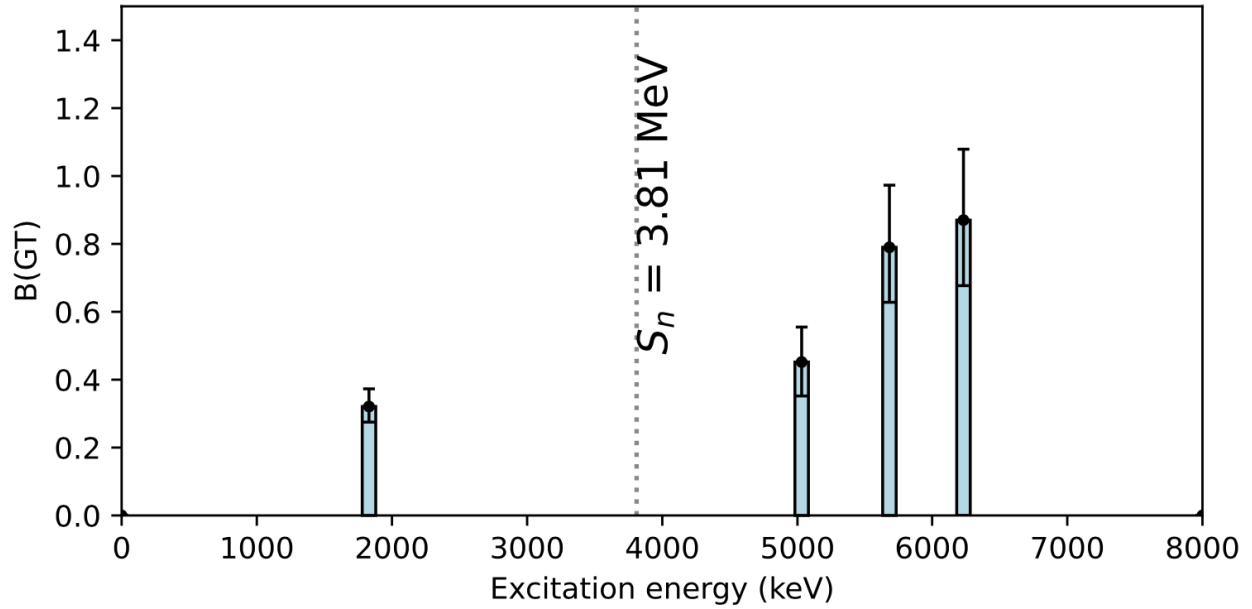


Figure 6.17: The experimental Gamow-Teller transition reduced matrix elements (B(GT)) for observed 1^+ states in ^{24}F .

Table 6.2: Branching ratios and logft values for the neutron emitting states in ^{24}F .

Ex. Energy (keV)	Branching Ratio (%)	logft
5031(22)	11.5(2.3)	4.1(0.1)
5684(37)	11.9(2.3)	3.9(0.1)
6223(51)	4.8(0.9)	4.0(0.1)

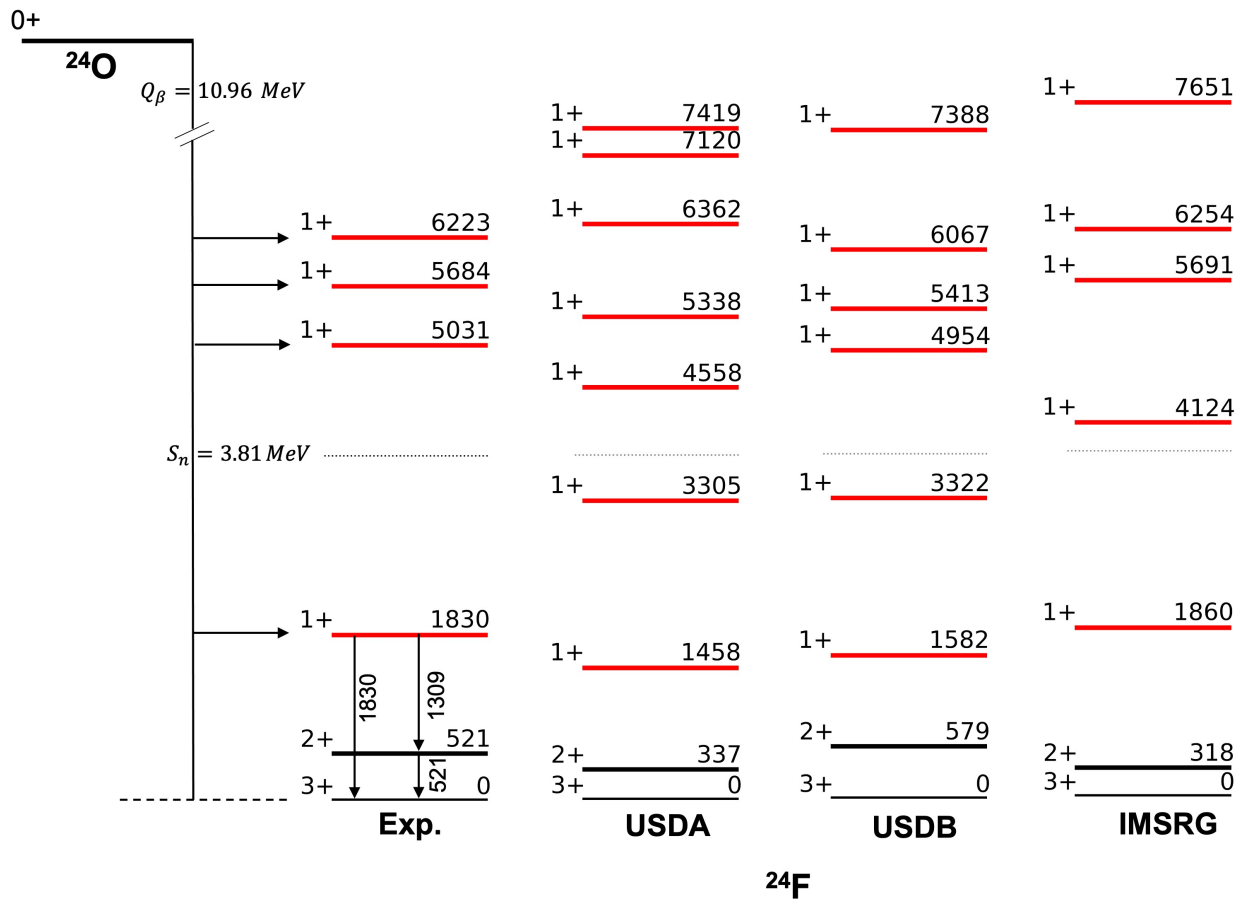
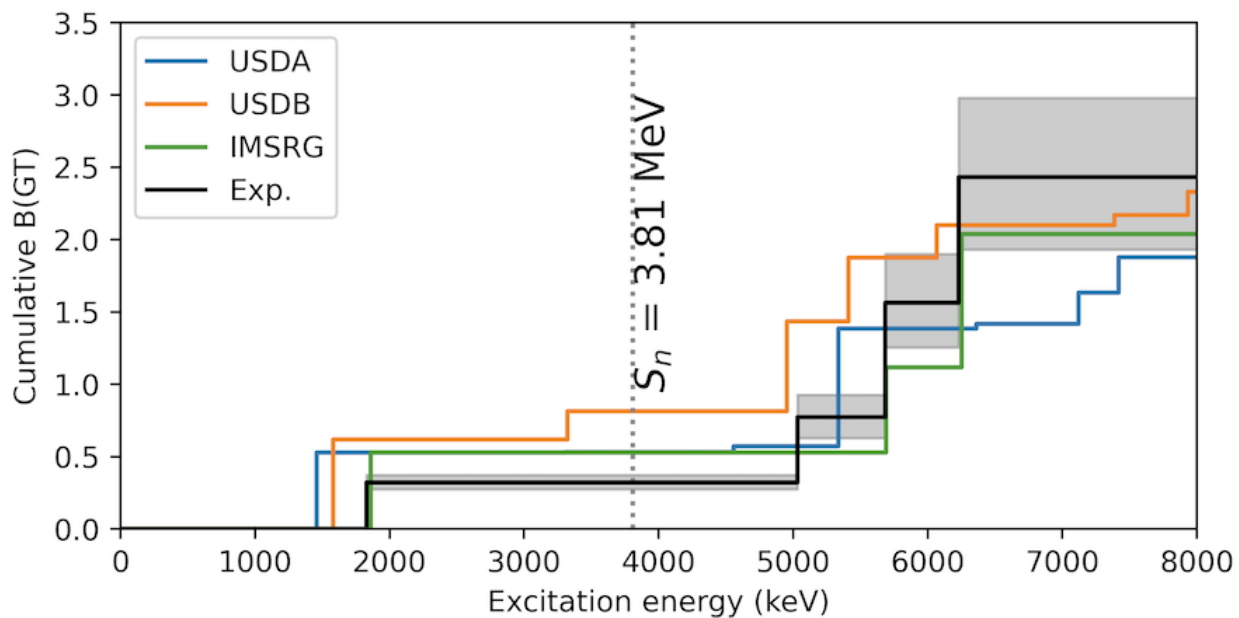
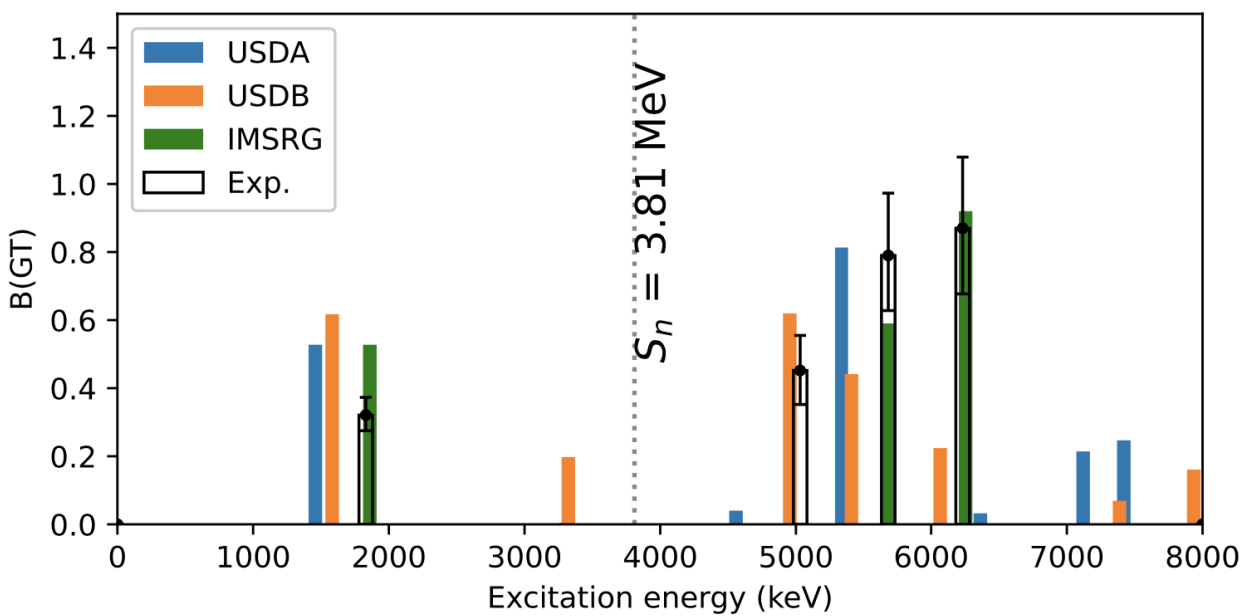


Figure 6.18: Comparison of the experimental ^{24}F energy levels with shell model calculations using standard USDA and USDB interactions and IMSRG. The states which are accessible to the Gamow-Teller transitions (1^+ states) are shown in red.



(a)



(b)

Figure 6.19: a) Comparison of the experimental B(GT) with shell model calculations using standard USDA and USDB interactions and IMSRG. b) Cumulative B(GT).

6.5.6 Discussion

Since ^{24}O ground state has spin and parity of 0^+ , the Gamow-Teller states in ^{24}F should have spin and parity of 1^+ to satisfy the Gamow-Teller selection rules as discussed in Section 1.1.1. The possible spin-orbit configurations for neutron and proton for Gamow-Teller transition in the decay of ^{24}O are summarized in Table 6.3.

The USDA and IMSRG underestimate the excitation energy of the first excited 2^+ state by ~ 200 keV while USDB produced a better agreement (579 keV) with the experimental value of 521 keV. This state decays to the ground state of ^{24}F , which has spin and parity of 3^+ . Both of these states (2^+ and 3^+) are part of $\pi d_{\frac{5}{2}} \otimes \nu s_{\frac{1}{2}}$ multiplet with almost pure ($\sim 70\%$) configuration.

The excitation energy of experimentally observed 1^+ state at 1830 keV is underestimated in both USDA and USDB calculations by ~ 300 keV, but IMSRG prediction is in good agreement (1860 keV). This state mainly ($\sim 50\%$) originates from $\pi s_{\frac{1}{2}} \otimes \nu s_{\frac{1}{2}}$ configuration. USDB overestimates the decay strength (B(GT)) to this state by $\sim 50\%$, but slightly better agreement is found in USDA and IMSRG. USDA and USDB predict the second 1^+ state at ~ 3300 keV, likely originating from $\pi d_{\frac{5}{2}} \otimes \nu d_{\frac{3}{2}}$ configuration but IMSRG estimates this state at 4124 keV. This state is close to the neutron separation energy (3810 keV), and the β decay strength feeding is very low. Its non-observation in the experiment may be attributed to the weak β decay feeding and low detection efficiency if this level decays directly to the ground state via γ emission. The detection threshold might be high if this state is just above the S_n as predicted by IMSRG and decays via neutron emission.

Three states above the neutron separation energy were observed in the experiment at energies of 5031(22), 5684(37), and 6223(57) keV, each of which has spin and parity of 1^+ as shown in Figure 6.18. USDA underestimates the state at 5031 keV by ~ 500 keV while a better agreement is found in USDB (4954 keV). USDA predicts weak decay strength to this state, but USDB has produced experimental value better. This state is not seen in IMSRG calculations. IMSRG has produced a good agreement with excitation energies and decay strengths for the states at 5684 keV and 6223 keV (5691 and 6254 keV, respectively). The energies of these states are underestimated by ~ 200 keV in USDB. It also underestimates the

decay strengths to these states. USDA underestimates the state at 5684 keV by ~ 350 keV, but decay strength agrees well with the experimental value. It better predicts the state at 6223 keV; still, the decay strength is very small compared to the measurement. Overall, USDB and IMSRG have produced a better agreement with the measurement in terms of both excitation energies and decay strengths. All three 1^+ states have somewhat mixed configurations of nuclear wave functions.

Table 6.3: The possible spin-orbit configurations for neutron and proton for Gamow-Teller transition in the decay of ^{24}O in sd-shell model space.

Spin-orbit configuration
$(\nu s_{\frac{1}{2}})^{-1} \otimes \pi s_{\frac{1}{2}}$
$(\nu d_{\frac{5}{2}})^{-1} \otimes \pi d_{\frac{3}{2}}$
$(\nu d_{\frac{5}{2}})^{-1} \otimes \pi d_{\frac{5}{2}}$
$(\nu d_{\frac{3}{2}})^{-1} \otimes \pi d_{\frac{5}{2}}$
$(\nu d_{\frac{3}{2}})^{-1} \otimes \pi d_{\frac{3}{2}}$

Chapter 7

Summary

As the capabilities of radioactive ion beam facilities are continually improving, the detector technology must also improve. NEXT is a novel neutron TOF detector for future studies of very neutron-rich nuclei. NEXT utilizes the concept of segmenting the detector along the neutron flight path direction, which reduces uncertainty in the flight path measurement and improves energy resolution without losing detection efficiency.

NEXT modules have been constructed using segments of n- γ discriminating plastic coupled to the position-sensitive photomultiplier tubes, allowing high-resolution timing and position measurements in β -delayed neutron spectroscopy. The n- γ discriminating capability of NEXT allows performing measurements in high γ ray background conditions. The position resolution provided by the segmentation in each NEXT module improves energy resolution in the neutron TOF measurements, which is vital to nuclear structure studies and astrophysics. NEXT is shown to improve neutron energy resolution when a correction from the three-dimensional scattering position inside the detector is applied. The TOF correction procedure was benchmarked using $^{27}\text{Al}(d,n)$ reactions and ^{17}N β -delayed neutron emission and applied to the ^{106}Nb decay, where it showed a dramatic change in the spectrum shape.

A high neutron detection efficiency of NEXT modules was demonstrated using neutrons produced from the $^{27}\text{Al}(d,n)$ reactions. Efficiency measurements of three NEXT modules, which differ in length and the scintillator material, were performed and analyzed. The performance of each of the modules is compatible with the prediction from GEANT4

simulations. A new trigger configuration has been developed, which leads to better measurements of low-energy neutrons.

NEXT was used alongside the VANDLE array at National Superconducting Cyclotron Laboratory(NSCL) to study light near drip-line nuclei at and below the island of inversion with the first-ever neutron spectroscopy performed for several isotopes from carbon to aluminum. β decay and subsequent neutron emission of ^{24}O were studied as a part of this dissertation. ^{24}O is a doubly magic drip line nucleus of the Oxygen isotopic chain. Studying decay properties of ^{24}O provides an excellent testing ground for benchmarking the nuclear model calculations near the neutron drip line.

β decay of ^{24}O was previously studied, but measurements focused only on the neutron-bound states in ^{24}F . Also, the half-life and neutron branching ratio were not well constrained. The present study measured the beta-delayed neutron spectrum for the first time. The updated half-life of 125(9) ms and a neutron branching ratio of 28(3)% were extracted from this measurement. Three neutron transitions were observed following the β decay of ^{24}O . Using these transitions, three new states above neutron separation energy in ^{24}F were constructed, and the decay strength to these states was obtained. The experimental results were compared with the shell model calculations using various interactions. The standard USDB interaction and interaction based on IMSRG provided a good agreement with the measurements.

Bibliography

- [1] C. S. Sumithrarachchi, D. J. Morrissey, A. D. Davies, D. A. Davies, M. Facina, E. Kwan, P. F. Mantica, M. Portillo, Y. Shimbara, J. Stoker, and R. R. Weerasiri. States in ^{22}O via β decay of ^{22}N . *Phys. Rev. C*, 81:014302, Jan 2010. [1](#), [76](#), [77](#)
- [2] C.R. Hoffman, T. Baumann, D. Bazin, J. Brown, G. Christian, D.H. Denby, P.A. DeYoung, J.E. Finck, N. Frank, J. Hinnefeld, S. Mosby, W.A. Peters, W.F. Rogers, A. Schiller, A. Spyrou, M.J. Scott, S.L. Tabor, M. Thoennessen, and P. Voss. Evidence for a doubly magic ^{24}O . *Physics Letters B*, 672(1):17–21, 2009. [1](#), [76](#), [77](#)
- [3] Yutaka Utsuno, Takaharu Otsuka, Takahiro Mizusaki, and Michio Honma. Extreme location of f drip line and disappearance of the $n = 20$ magic structure. *Phys. Rev. C*, 64:011301, Jun 2001. [1](#), [76](#)
- [4] M Thoennessen. Reaching the limits of nuclear stability. *Reports on Progress in Physics*, 67(7):1187, jun 2004. [1](#), [76](#)
- [5] Björn Jonson. Light dripline nuclei. *Physics Reports*, 389(1):1–59, 2004. [1](#), [76](#)
- [6] M Pfützner, E Badura, C Bingham, Bertram Blank, M Chartier, H Geissel, J Giovinazzo, LV Grigorenko, R Grzywacz, M Hellström, et al. First evidence for the two-proton decay of ^{45}Fe . *The European Physical Journal A-Hadrons and Nuclei*, 14(3):279–285, 2002. [1](#)
- [7] I.N. Borzov. Beta-decay rates. *Nuclear Physics A*, 777:645–675, 2006. Special Issue on Nuclear Astrophysics. [3](#)

- [8] R. B. Roberts, R. C. Meyer, and P. Wang. Further observations on the splitting of uranium and thorium. *Phys. Rev.*, 55:510–511, Mar 1939. [4](#)
- [9] Daniel Abriola, Balraj Singh, and Iris Dillmann. Summary report of consultants’ meeting on beta-delayed neutron emission evaluation. Technical report, International Atomic Energy Agency, 2011. [8](#), [13](#)
- [10] M Pfützner, M Karny, LV Grigorenko, and Karsten Riisager. Radioactive decays at limits of nuclear stability. *Reviews of modern physics*, 84(2):567, 2012. [8](#)
- [11] T Nakamura, H Sakurai, and H Watanabe. Exotic nuclei explored at in-flight separators. *Progress in Particle and Nuclear Physics*, 97:53–122, 2017. [8](#)
- [12] K-L Kratz and G Herrmann. Systematics of neutron emission probabilities from delayed neutron precursors. *Zeitschrift für Physik*, 263(5):435–442, 1973. [8](#)
- [13] Kohji Takahashi and Masami Yamada. Gross Theory of Nuclear β -Decay. *Progress of Theoretical Physics*, 41(6):1470–1503, 06 1969. [8](#)
- [14] Peter Möller, Bernd Pfeiffer, and Karl-Ludwig Kratz. New calculations of gross β -decay properties for astrophysical applications: Speeding-up the classical r process. *Physical Review C*, 67(5):055802, 2003. [8](#)
- [15] Rin Yokoyama, Robert Grzywacz, B Charlie Rasco, Nathan Brewer, Krzysztof P Rykaczewski, Iris Dillmann, Jose Louis Tain, Shunji Nishimura, DS Ahn, Alejandro Algara, et al. Strong one-neutron emission from two-neutron unbound states in β decays of the r-process nuclei ga 86, 87. *Physical Review C*, 100(3):031302, 2019. [9](#)
- [16] T Kawano, P Möller, and WB Wilson. Calculation of delayed-neutron energy spectra in a quasiparticle random-phase approximation–hauser-feshbach model. *Physical Review C*, 78(5):054601, 2008. [9](#), [11](#)
- [17] AJ Koning and JP Delaroche. Local and global nucleon optical models from 1 kev to 200 mev. *Nuclear Physics A*, 713(3-4):231–310, 2003. [9](#)

- [18] A Gilbert and AGW Cameron. A composite nuclear-level density formula with shell corrections. *Canadian Journal of Physics*, 43(8):1446–1496, 1965. [12](#)
- [19] J Kopecky and M. Uhl. Test of gamma-ray strength functions in nuclear reaction model calculations. *Physical Review C*, 41(5):1941, 1990. [12](#)
- [20] Benjamin P Abbott, Rich Abbott, TD Abbott, Fausto Acernese, Kendall Ackley, Carl Adams, Thomas Adams, Paolo Addesso, RX Adhikari, VB Adya, et al. Gw170817: observation of gravitational waves from a binary neutron star inspiral. *Physical Review Letters*, 119(16):161101, 2017. [12](#)
- [21] T Kajino, W Aoki, AB Balantekin, R Diehl, MA Famiano, and GJ Mathews. Current status of r-process nucleosynthesis. *Progress in Particle and Nuclear Physics*, 2019. [12](#)
- [22] Matthew R Mumpower, Rebecca Surman, GC McLaughlin, and A Aprahamian. The impact of individual nuclear properties on r-process nucleosynthesis. *Progress in Particle and Nuclear Physics*, 86:86–126, 2016. [12](#)
- [23] FRIB Decay Station White Paper. <https://fds.ornl.gov/wp-content/uploads/2020/09/FDS-WP.pdf>. [12](#), [14](#)
- [24] María Belén Gómez-Hornillos, J Rissanen, JL Taín, A Algora, KL Kratz, G Lhersonneau, B Pfeiffer, J Agramunt, D Cano-Ott, V Gorlychev, et al. β -delayed neutron emission studies. *Hyperfine interactions*, 223(1-3):185–194, 2014. [16](#)
- [25] R Grzywacz, KP Rykaczewski, CJ Gross, M Madurga, K Miernik, DT Miller, SV Paulauskas, SW Padgett, C Rasco, M Wolinska-Cichocka, et al. Hybrid-3hen—new detector for gammas and neutrons. *Acta Physica Polonica B*, 45(2):217–222, 2014. [16](#)
- [26] Alvaro Tolosa-Delgado, Jorge Agramunt, José Luis Taín, Alejandro Algora, César Domingo-Pardo, AI Morales, Berta Rubio, A Tarifeño-Saldivia, F Calviño, G Cortes, et al. Commissioning of the briken detector for the measurement of very exotic β -delayed neutron emitters. *Nuclear Instruments and Methods in Physics Research Section A: Accelerators, Spectrometers, Detectors and Associated Equipment*, 925:133–147, 2019. [16](#)

- [27] J Pereira, P Hosmer, G Lorusso, P Santi, A Couture, J Daly, M Del Santo, T Elliot, J Görres, C Herlitzius, et al. The neutron long counter nero for studies of β -delayed neutron emission in the r-process. *Nuclear Instruments and Methods in Physics Research Section A: Accelerators, Spectrometers, Detectors and Associated Equipment*, 618(1-3):275–283, 2010. [16](#)
- [28] WA Peters, S Ilyushkin, M Madurga, C Matei, SV Paulauskas, RK Grzywacz, DW Bardayan, CR Brune, J Allen, JM Allen, et al. Performance of the versatile array of neutron detectors at low energy (vandle). *Nuclear Instruments and Methods in Physics Research Section A: Accelerators, Spectrometers, Detectors and Associated Equipment*, 836:122–133, 2016. [16](#), [83](#)
- [29] George Perdikakis, M Sasano, Sam M Austin, D Bazin, C Caesar, S Cannon, JM Deaven, HJ Doster, CJ Guess, GW Hitt, et al. Lenda: A low energy neutron detector array for experiments with radioactive beams in inverse kinematics. *Nuclear Instruments and Methods in Physics Research Section A: Accelerators, Spectrometers, Detectors and Associated Equipment*, 686:117–124, 2012. [16](#)
- [30] S. Shalev and J. M. Cuttler. The energy distribution of delayed fission neutrons. *Nuclear Science and Engineering*, 51(1):52–66, 1973. [16](#)
- [31] ND Scielzo, Gang Li, MG Sternberg, G Savard, PF Bertone, Fritz Buchinger, Salen Caldwell, JA Clark, John Crawford, CM Deibel, et al. The β -decay paul trap: A radiofrequency-quadrupole ion trap for precision β -decay studies. *Nuclear Instruments and Methods in Physics Research Section A: Accelerators, Spectrometers, Detectors and Associated Equipment*, 681:94–100, 2012. [16](#)
- [32] GL Wilson, TS Nagel, ST Marley, ND Scielzo, A Aprahamian, JA Clark, A Czeszumaska, G Savard, K Siegl, and BS Wang. Reconstruction of β -delayed neutron energy spectra from recoil-ion spectroscopy of trapped ions. *Nuclear Instruments and Methods in Physics Research Section A: Accelerators, Spectrometers, Detectors and Associated Equipment*, 1017:165806, 2021. [16](#)

- [33] Ryan Matthew Yee, ND Scielzo, PF Bertone, F Buchinger, S Caldwell, JA Clark, CM Deibel, J Fallis, JP Greene, S Gulick, et al. β -delayed neutron spectroscopy using trapped radioactive ions. *Physical review letters*, 110(9):092501, 2013. 16
- [34] PE Garrett. Descant—the deuterated scintillator array for neutron tagging. In *ISAC and ARIEL: The TRIUMF Radioactive Beam Facilities and the Scientific Program*, pages 137–141. Springer, 2013. 16
- [35] M Febbraro, R Toomey, SD Pain, KA Chipps, B Becker, RJ Newby, Z Meisel, TN Massey, CR Brune, Q Liu, et al. The ornl deuterated spectroscopic array—odesa. *Nuclear Instruments and Methods in Physics Research Section A: Accelerators, Spectrometers, Detectors and Associated Equipment*, 946:162668, 2019. 16
- [36] Glenn F Knoll. *Radiation detection and measurement*. John Wiley & Sons, 2010. 20
- [37] Alexandra Gade, C. Konrad Gelbke, and Thomas Glasmacher. Nsl and the facility for rare isotope beams (frib) project. *Nuclear Physics News*, 24(1):28–30, 2014. 21, 76
- [38] J Heideman, D Pérez-Loureiro, R Grzywacz, CR Thornsberry, J Chan, LH Heilbronn, SK Neupane, K Schmitt, MM Rajabali, AR Engelhardt, et al. Conceptual design and first results for a neutron detector with interaction localization capabilities. *Nuclear Instruments and Methods in Physics Research Section A: Accelerators, Spectrometers, Detectors and Associated Equipment*, 946:162528, 2019. 22, 28, 64
- [39] Eljen technologies. <https://eljentechnology.com>. 23
- [40] 3M™. <https://www.3m.com/>. 23
- [41] Hamamatsu Photonics K. K. <https://www.hamamatsu.com/jp/en/index.html>. 23, 32, 83
- [42] Vertilon Corporation, Westford, MA. <https://vertilon.com/>. 23, 24, 27, 36
- [43] XIA LLC. https://www.xia.com/dgf_pixie-16.html. 23, 34

- [44] W.A. Peters, S. Ilyushkin, M. Madurga, C. Matei, S.V. Paulauskas, R.K. Grzywacz, D.W. Bardayan, C.R. Brune, J. Allen, J.M. Allen, Z. Bergstrom, J. Blackmon, N.T. Brewer, J.A. Cizewski, P. Copp, M.E. Howard, R. Ikeyama, R.L. Kozub, B. Manning, T.N. Massey, M. Matos, E. Merino, P.D. O'Malley, F. Raiola, C.S. Reingold, F. Sarazin, I. Spassova, S. Taylor, and D. Walter. Performance of the versatile array of neutron detectors at low energy (vandle). *Nuclear Instruments and Methods in Physics Research Section A: Accelerators, Spectrometers, Detectors and Associated Equipment*, 836:122–133, 2016. [24](#)
- [45] Cory R. Thornsberry. *Proton Transfer Reactions Studied Using the Versatile Array of Neutron Detectors at Low Energy (VANDLE)*. PhD thesis, University of Tennessee, 2018. [24](#)
- [46] Hal O Anger. Scintillation camera with multichannel collimators. 1964. [25](#), [57](#)
- [47] S. Siegel, R.W. Silverman, Yiping Shao, and S.R. Cherry. Simple charge division readouts for imaging scintillator arrays using a multi-channel pmt. *IEEE Transactions on Nuclear Science*, 43(3):1634–1641, 1996. [25](#)
- [48] T. N. Massey, S. Al-Quraishi, C. E. Brient, J. F. Guillemette, S. M. Grimes, D. Jacobs, J. E. O'Donnell, J. Oldendick, and R. Wheeler. A measurement of the ^{27}Al (d, n) spectrum for use in neutron detector calibration. *Nuclear Science and Engineering*, 129(2):175–179, 1998. [45](#), [46](#)
- [49] J. Heideman, D. Pérez-Loureiro, R. Grzywacz, C.R. Thornsberry, J. Chan, L.H. Heilbronn, S.K. Neupane, K. Schmitt, M.M. Rajabali, A.R. Engelhardt, and et al. Conceptual design and first results for a neutron detector with interaction localization capabilities. *Nuclear Instruments and Methods in Physics Research Section A: Accelerators, Spectrometers, Detectors and Associated Equipment*, 946:162528, Dec 2019. [47](#)
- [50] S. Agostinelli, J. Allison, K. Amako, J. Apostolakis, H. Araujo, P. Arce, M. Asai, D. Axen, S. Banerjee, G. Barrand, F. Behner, L. Bellagamba, J. Boudreau, L. Broglia,

A. Brunengo, H. Burkhardt, S. Chauvie, J. Chuma, R. Chytraccek, G. Cooperman, G. Cosmo, P. Degtyarenko, A. Dell’Acqua, G. Depaola, D. Dietrich, R. Enami, A. Feliciello, C. Ferguson, H. Fesefeldt, G. Folger, F. Foppiano, A. Forti, S. Garelli, S. Giani, R. Giannitrapani, D. Gibin, J.J. Gómez Cadenas, I. González, G. Gracia Abril, G. Greeniaus, W. Greiner, V. Grichine, A. Grossheim, S. Guatelli, P. Gumplinger, R. Hamatsu, K. Hashimoto, H. Hasui, A. Heikkinen, A. Howard, V. Ivanchenko, A. Johnson, F.W. Jones, J. Kallenbach, N. Kanaya, M. Kawabata, Y. Kawabata, M. Kawaguti, S. Kelner, P. Kent, A. Kimura, T. Kodama, R. Kokoulin, M. Kossov, H. Kurashige, E. Lamanna, T. Lampén, V. Lara, V. Lefebure, F. Lei, M. Liendl, W. Lockman, F. Longo, S. Magni, M. Maire, E. Medernach, K. Minamimoto, P. Mora de Freitas, Y. Morita, K. Murakami, M. Nagamatu, R. Nartallo, P. Nieminen, T. Nishimura, K. Ohtsubo, M. Okamura, S. O’Neale, Y. Oohata, K. Paech, J. Perl, A. Pfeiffer, M.G. Pia, F. Ranjard, A. Rybin, S. Sadilov, E. Di Salvo, G. Santin, T. Sasaki, N. Savvas, Y. Sawada, S. Scherer, S. Sei, V. Sirotenko, D. Smith, N. Starkov, H. Stoecker, J. Sulkimo, M. Takahata, S. Tanaka, E. Tcherniaev, E. Safai Tehrani, M. Tropeano, P. Truscott, H. Uno, L. Urban, P. Urban, M. Verderi, A. Walkden, W. Wander, H. Weber, J.P. Wellisch, T. Wenaus, D.C. Williams, D. Wright, T. Yamada, H. Yoshida, and D. Zschiesche. Geant4—a simulation toolkit. *Nuclear Instruments and Methods in Physics Research Section A: Accelerators, Spectrometers, Detectors and Associated Equipment*, 506(3):250–303, 2003. [47](#)

- [51] J. Allison, K. Amako, J. Apostolakis, P. Arce, M. Asai, T. Aso, E. Bagli, A. Bagulya, S. Banerjee, G. Barrant, B.R. Beck, A.G. Bogdanov, D. Brandt, J.M.C. Brown, H. Burkhardt, Ph. Canal, D. Cano-Ott, S. Chauvie, K. Cho, G.A.P. Cirrone, G. Cooperman, M.A. Cortés-Giraldo, G. Cosmo, G. Cuttone, G. Depaola, L. Desorgher, X. Dong, A. Dotti, V.D. Elvira, G. Folger, Z. Francis, A. Galoyan, L. Garnier, M. Gayer, K.L. Genser, V.M. Grichine, S. Guatelli, P. Guèye, P. Gumplinger, A.S. Howard, I. Hřivnáčová, S. Hwang, S. Incerti, A. Ivanchenko, V.N. Ivanchenko, F.W. Jones, S.Y. Jun, P. Kaitaniemi, N. Karakatsanis, M. Karamitros, M. Kelsey, A. Kimura, T. Koi, H. Kurashige, A. Lechner, S.B. Lee, F. Longo, M. Maire, D. Mancusi, A. Mantero,

- E. Mendoza, B. Morgan, K. Murakami, T. Nikitina, L. Pandola, P. Paprocki, J. Perl, I. Petrović, M.G. Pia, W. Pokorski, J.M. Quesada, M. Raine, M.A. Reis, A. Ribon, A. Ristić Fira, F. Romano, G. Russo, G. Santin, T. Sasaki, D. Sawkey, J.I. Shin, I.I. Strakovsky, A. Taborda, S. Tanaka, B. Tomé, T. Toshito, H.N. Tran, P.R. Truscott, L. Urban, V. Uzhinsky, J.M. Verbeke, M. Verderi, B.L. Wendt, H. Wenzel, D.H. Wright, D.M. Wright, T. Yamashita, J. Yarba, and H. Yoshida. Recent developments in geant4. *Nuclear Instruments and Methods in Physics Research Section A: Accelerators, Spectrometers, Detectors and Associated Equipment*, 835:186–225, 2016. [47](#)
- [52] H Ohm, W Rudolph, and K-L Kratz. Beta-delayed neutron emission following the decay of ^{17}n . *Nuclear Physics A*, 274(1-2):45–52, 1976. [60](#), [64](#), [95](#)
- [53] H Miyatake, H Ueno, Y Yamamoto, N Aoi, K Asahi, E Ideguchi, M Ishihara, H Izumi, T Kishida, T Kubo, et al. Spin-parity assignments in $^{15}\text{c}^*$ by a new method: β -delayed spectroscopy for a spin-polarized nucleus. *Physical Review C*, 67(1):014306, 2003. [60](#), [95](#)
- [54] R. Yokoyama, M. Singh, R. Grzywacz, A. Keeler, T.T. King, J. Agramunt, N.T. Brewer, S. Go, J. Heideman, J. Liu, S. Nishimura, P. Parkhurst, V.H. Phong, M.M. Rajabali, B.C. Rasco, K.P. Rykaczewski, D.W. Stracener, J.L. Tain, A. Tolosa-Delgado, K. Vaigneur, and M. Wolińska-Cichocka. Segmented yso scintillation detectors as a new β -implant detection tool for decay spectroscopy in fragmentation facilities. *Nuclear Instruments and Methods in Physics Research Section A: Accelerators, Spectrometers, Detectors and Associated Equipment*, 937:93–97, 2019. [60](#), [83](#)
- [55] J. Brenneisen, D. Grathwohl, M. Lickert, R. Ott, H. Ropke, J. Schmalzlin, P. Siedle, and B. H. Wildenthal. The structure of ^{28}si above 10 mev excitation energy i: Gamma-decay modes and radiative widths of levels. *Z.Phys.*, A352:149, 1995. [71](#)
- [56] H. Satyanarayana, M. Ahmad, C. E. Brient, P. M. Egun, S. L. Graham, S. M. Grimes, and S. K. Saraf. Identification of new excited levels in ^{28}Si through the $^{27}\text{Al}(\text{d},\text{n})^{28}\text{si}$ reaction. *Phys. Rev. C*, 32:394–399, Aug 1985. [71](#)

- [57] W. Bohne, H. Fuchs, K. Grabisch, M. Hagen, H. Homeyer, U. Janetzki, H. Lettau, K.H. Maier, H. Morgenstern, P. Pietrzyk, G. Röscher, and J.A. Scheer. One-proton and two-proton stripping between ^{26}Mg , ^{27}Al and ^{28}Si . *Nuclear Physics A*, 131(2):273–304, 1969. [71](#)
- [58] C. Miehé, A. Huck, G. Klotz, and G. Walter. $t = 1$ positive parity states in ^{28}Si and ^{28}P . *Phys. Rev. C*, 15:30–39, Jan 1977. [71](#)
- [59] TN Massey, S Al-Quraishi, CE Brient, JF Guillemette, SM Grimes, D Jacobs, JE O’Donnell, J Oldendick, and R Wheeler. A measurement of the ^{27}Al (d, n) spectrum for use in neutron detector calibration. *Nuclear science and engineering*, 129(2):175–179, 1998. [64](#)
- [60] S. Neupane, J. Heideman, R. Grzywacz, J. Hooker, K.L. Jones, N. Kitamura, C.R. Thornsberry, L.H. Heilbronn, M.M. Rajabali, Y. Albery-Jones, J. Derkin, T. Massey, and D. Soltesz. Neutron detection efficiency of the neutron detector with xn tracking (next). *Nuclear Instruments and Methods in Physics Research Section A: Accelerators, Spectrometers, Detectors and Associated Equipment*, page 165881, 2021. [64](#)
- [61] Marek Karny, Krzysztof P Rykaczewski, A Fijałkowska, Bertis C Rasco, Marzena Wolińska-Cichočka, RK Grzywacz, KC Goetz, D Miller, and EF Zganjar. Modular total absorption spectrometer. *Nuclear Instruments and Methods in Physics Research Section A: Accelerators, Spectrometers, Detectors and Associated Equipment*, 836:83–90, 2016. [65](#)
- [62] Maria Goeppert Mayer. On closed shells in nuclei. ii. *Physical Review*, 75(12):1969, 1949. [77](#)
- [63] Otto Haxel, J Hans D Jensen, and Hans E Suess. On the” magic numbers” in nuclear structure. *Physical Review*, 75(11):1766, 1949. [77](#)
- [64] R Kanungo, C Nociforo, A Prochazka, T Aumann, D Boutin, D Cortina-Gil, B Davids, M Diakaki, F Farinon, H Geissel, et al. One-neutron removal measurement reveals ^{28}O as a new doubly magic nucleus. *Physical review letters*, 102(15):152501, 2009. [77](#)

- [65] Y Kondo, T Nakamura, R Tanaka, R Minakata, S Ogoshi, NA Orr, NL Achouri, T Aumann, H Baba, F Delaunay, et al. Nucleus o 26: A barely unbound system beyond the drip line. *Physical Review Letters*, 116(10):102503, 2016. [77](#)
- [66] Akira Ozawa, T Kobayashi, T Suzuki, K Yoshida, and I Tanihata. New magic number, $n=16$, near the neutron drip line. *Physical review letters*, 84(24):5493, 2000. [77](#)
- [67] K Tshoo, Y Satou, H Bhang, S Choi, T Nakamura, Y Kondo, S Deguchi, Y Kawada, N Kobayashi, Y Nakayama, et al. $N=16$ spherical shell closure in o 24. *Physical review letters*, 109(2):022501, 2012. [77](#)
- [68] Takaharu Otsuka, Toshio Suzuki, Jason D Holt, Achim Schwenk, and Yoshinori Akaishi. Three-body forces and the limit of oxygen isotopes. *Physical review letters*, 105(3):032501, 2010. [77](#), [79](#)
- [69] Gaute Hagen, M Hjorth-Jensen, GR Jansen, R Machleidt, and T Papenbrock. Continuum effects and three-nucleon forces in neutron-rich oxygen isotopes. *Physical Review Letters*, 108(24):242501, 2012. [79](#)
- [70] AC Mueller, D Guillemaud-Mueller, JC Jacmart, E Kashy, F Pougheon, A Richard, A Staudt, HV Klapdor-Kleingrothaus, M Lewitowicz, R Anne, et al. Measurement and qrpa calculation of the β -delayed neutron emission of 21, 22n and 23, 24o. *Nuclear Physics A*, 513(1):1–10, 1990. [79](#), [88](#)
- [71] A. T. Reed, O. Tarasov, R. D. Page, D. Guillemaud-Mueller, Yu. E. Penionzhkevich, R. G. Allatt, J. C. Angélique, R. Anne, C. Borcea, V. Burjan, W. N. Catford, Z. Dlouhý, C. Donzaud, S. Grévy, M. Lewitowicz, S. M. Lukyanov, F. M. Marqués, G. Martinez, A. C. Mueller, P. J. Nolan, J. Novák, N. A. Orr, F. Pougheon, P. H. Regan, M. G. Saint-Laurent, T. Siiskonen, E. Sokol, O. Sorlin, J. Suhonen, W. Trinder, and S. M. Vincent. Radioactivity of neutron-rich oxygen, fluorine, and neon isotopes. *Phys. Rev. C*, 60:024311, Jul 1999. [79](#), [88](#)
- [72] Yu E Penionzhkevich. Research on neutron-rich nuclei in the region of the nuclear shells $n=20$ and $n=28$. *Physics of Atomic Nuclei*, 64(6):1121–1126, 2001. [79](#), [88](#)

- [73] L Cáceres, A Lepailleur, O Sorlin, M Stanoiu, D Sohler, Zs Dombradi, SK Bogner, BA Brown, H Hergert, JD Holt, et al. Nuclear structure studies of f 24. *Physical Review C*, 92(1):014327, 2015. [79](#), [88](#)
- [74] A Stolz, T Baumann, TN Ginter, DJ Morrissey, M Portillo, BM Sherrill, M Steiner, and JW Stetson. Production of rare isotope beams with the nscl fragment separator. *Nuclear Instruments and Methods in Physics Research Section B: Beam Interactions with Materials and Atoms*, 241(1-4):858–861, 2005. [79](#), [82](#)
- [75] K-H Schmidt, E Hanelt, H Geissel, G Münzenberg, and JP Dufour. The momentum-loss achromat—a new method for the isotopical separation of relativistic heavy ions. *Nuclear Instruments and Methods in Physics Research Section A: Accelerators, Spectrometers, Detectors and Associated Equipment*, 260(2-3):287–303, 1987. [81](#)
- [76] Jerzy Cetnar. General solution of bateman equations for nuclear transmutations. *Annals of Nuclear Energy*, 33(7):640–645, 2006. [88](#)
- [77] AT Reed, O Tarasov, RD Page, D Guillemaud-Mueller, Yu E Penionzhkevich, RG Allatt, JC Angélique, R Anne, C Borcea, V Burjan, et al. Radioactivity of neutron-rich oxygen, fluorine, and neon isotopes. *Physical Review C*, 60(2):024311, 1999. [88](#)
- [78] J. P. Dufour, R. Del Moral, A. Fleury, F. Hubert, D. Jean, M. S. Pravikoff, H. Delagrange, H. Geissel, and K. H. Schmidt. Beta decay of ^{17}c , ^{19}n , ^{22}o , ^{24}f , ^{26}ne , ^{32}al , ^{34}al , $^{35-36}\text{si}$, $^{36-38}\text{p}$, ^{40}s . *Z.Phys.*, A324:487, 1986. [93](#)
- [79] CS Sumithrarachchi, DJ Morrissey, BA Brown, AD Davies, DA Davies, M Fancina, E Kwan, PF Mantica, M Portillo, Y Shimbara, et al. Structure of f 23 via β decay of o 23. *Physical Review C*, 75(2):024305, 2007. [93](#)
- [80] Noritaka Shimizu. Nuclear shell-model code for massive parallel computation,” kshell”. *arXiv preprint arXiv:1310.5431*, 2013. [99](#)
- [81] BH Wildenthal. Empirical strengths of spin operators in nuclei. *Progress in particle and nuclear physics*, 11:5–51, 1984. [99](#)

- [82] B Alex Brown and WA Richter. New “usd” hamiltonians for the sd shell. *Physical Review C*, 74(3):034315, 2006. [99](#)
- [83] Koshiroh Tsukiyama, SK Bogner, and A Schwenk. In-medium similarity renormalization group for nuclei. *Physical review letters*, 106(22):222502, 2011. [99](#)
- [84] H Hergert, SK Bogner, TD Morris, A Schwenk, and K Tsukiyama. The in-medium similarity renormalization group: A novel ab initio method for nuclei. *Physics reports*, 621:165–222, 2016. [99](#)

Vita

Shree Neupane was born in Baglung, Nepal. He earned his school education in his hometown and moved to Kathmandu, the capital city of Nepal, for higher education. After completing B.Sc. and M.Sc. degrees in Physics from Tribhuvan University, Nepal, he came to the United States for further studies. He first joined the master's program at Central Michigan University and started research in experimental nuclear physics. He continued his research in low-energy experimental nuclear physics by joining the Ph.D. program at the University of Tennessee, Knoxville. After graduation, he wants to pursue a career in nuclear physics as a researcher. Besides his professional interests, he likes outdoor activities like hiking, camping, mountain biking, and skiing.